JSCSEN 91(5)441-557(2026)

ISSN 1820-7421(Online)

Journal of the Serbian Chemical Society

Electronic version

VOLUME 91

No 5

BELGRADE 2026

Available on line at

www.shd.org.rs/JSCS/

The full search of JSCS is available through

DOAJ DIRECTORY OF OPEN ACCESS JOURNALS

www.doaj.org

The **Journal of the Serbian Chemical Society** (formerly Glasnik Hemijskog društva Beograd), one volume (12 issues) per year, publishes articles from the fields of chemistry. The **Journal** is financially supported by the **Ministry of Science, Technological Development and Innovation of the Republic of Serbia.**
Articles published in the **Journal** are indexed in **Clarivate Analytics products: Science Citation Index-Expanded™** – accessed *via* **Web of Science®** and **Journal Citation Reports®**.
Impact Factor announced for the year 2024: **0.700; 5-year Impact Factor**: **0.900**.
Articles appearing in the **Journal** are also abstracted by: **Scopus, Chemical Abstracts Plus (CAplus℠), Directory of Open Access Journals, Referativnii Zhurnal (VINITI), RSC Analytical Abstracts, EuroPub, Pro Quest** and **Asian Digital Library.**

Publisher:	**Serbian Chemical Society**, Karnegijeva 4/III, P. O. Box 36, 1120 Belgrade 35, Serbia tel./fax: +381–11–3370–467, E-mails: **Society** – shd@shd.org.rs; **Journal** – jscs@shd.org.rs Home Pages: **Society** – http://www.shd.org.rs/, **Journal** – http://www.shd.org.rs/JSCS/
Internet Service:	Contents, Abstracts and full papers (from Vol. 64, No. 1, 1999) are available in the electronic form at the Web Site of the **Journal** (http://www.shd.org.rs/JSCS/).
Former Editors:	**Nikola A. Pušin** (1930–1947), **Aleksandar M. Leko** (1948–1954), **Panta S. Tutundžić** (1955**–**1961), **Miloš K. Mladenović** (1962–1964), **Đorđe M. Dimitrijević** (1965–1969), **Aleksandar R. Despić** (1969–1975), **Slobodan V. Ribnikar** (1975–1985), **Dragutin M. Dražić** (1986–2006), **Branislav Ž. Nikolić** (2006-2026).
Editor-in-Chief:	DUŠAN **SLADIĆ**, Faculty of Chemistry, University of Belgrade
Deputy Editors:	MARIO **ZLATOVIĆ**, Faculty of Chemistry, University of Belgrade, VLADIMIR **PANIĆ**, Institute of Chemistry, Technology and Metallurgy, University of Belgrade
Sub editors:	
,	
Organic Chemistry	DEJAN **OPSENICA**, Institute of Chemistry, Technology and Metallurgy, University of Belgrade JÁNOS **CSANÁDI**, Faculty of Science, University of Novi Sad
Biochemistry and Biotechnology	OLGICA **NEDIĆ**, INEP – Institute for the Application of Nuclear Energy, University of Belgrade
Inorganic Chemistry	BILJANA **GLIŠIĆ**, Faculty of Science, University of Kragujevac
Theoretical Chemistry	MATIJA **ZLATAR**, Institute of Chemistry, Technology and Metallurgy, University of Belgrade MILOŠ **MILIČIĆ**, Faculty of Chemistry, University of Belgrade
Physical Chemistry	LJILJANA **DAMJANOVIĆ-VASILIĆ**, Faculty of Physical Chemistry, University of Belgrade
Electrochemistry	SNEŽANA **GOJKOVIĆ**, Faculty of Technology and Metallurgy, University of Belgrade
Analytical Chemistry	RADA **BAOŠIĆ**, Faculty of Chemistry, University of Belgrade
Polymers	BRANKO **DUNJIĆ**, Faculty of Technology and Metallurgy, University of Belgrade
Thermodynamics	MIRJANA **KIJEVČANIN**, Faculty of Technology and Metallurgy, University of Belgrade
Chemical Engineering	TATJANA **KALUĐEROVIĆ RADOIČIĆ**, Faculty of Technology and Metallurgy, University of Belgrade
Materials	RADA **PETROVIĆ**, Faculty of Technology and Metallurgy, University of Belgrade
Metallic Materials and Metallurgy	ANA **KOSTOV**, Mining and Metallurgy Institute Bor, University of Belgrade
Environmental and Geochemistry	VESNA **ANTIĆ**, Faculty of Agriculture, University of Belgrade
History of and Education in Chemistry	DRAGICA **TRIVIĆ**, Faculty of Chemistry, University of Belgrade
English Language Editors:	VLATKA **VAJS**, Serbian Chemical Society MIROSLAV **PAVLOVIĆ**, Institute of Chemistry, Technology and Metallurgy, University of Belgrade
Journal Manager & Web Master:	MARIO **ZLATOVIĆ**, Faculty of Chemistry, University of Belgrade
Office:	VERA **ĆUŠIĆ**, Serbian Chemical Society

Editorial Board
From abroad: **R. Adžić**, Brookhaven National Laboratory (USA); **A. Casini**, University of Groningen (The Netherlands); **G. Cobb**, Baylor University (USA); **D. Douglas**, University of British Columbia (Canada); **G. Inzelt**, Etvos Lorand University (Hungary); **J. Kenny**, University of Perugia (Italy); **Ya. I. Korenman**, Voronezh Academy of Technology (Russian Federation); **M. D. Lechner**, University of Osnabrueck (Germany); **S. Macura**, Mayo Clinic (USA); **M. Spiteller**, INFU, Technical University Dortmund (Germany); **M. Stratakis**, University of Crete (Grecce); **M. Swart**, University de Girona (Cataluna, Spain); **G. Vunjak-Novaković**, Columbia University (USA); **P. Worsfold**, University of Plymouth (UK); **J. Zagal**, Universidad de Santiago de Chile (Chile).
From Serbia: **B. Abramović**, **V. Antić**, **R. Baošić**, **V. Beškoski**, **J. Csanadi**, **Lj. Damjanović-Vasilić**, **A. Dekanski**, **V. Dondur**, **B. Dunjić**, **M. Đuran, B. Glišić, S. Gojković**, **I. Gutman**, **B. Jovančićević**, **I. Juranić**, **T. Kaluđerović Radoičić**, **L. Katsikas**, **M. Kijevčanin**, **A. Kostov**, **V. Leovac**, **S. Milonjić**, **V.B. Mišković-Stanković**, **O. Nedić**, **D. Opsenica**, **V. Panić**, **M. Pavlović**, **M. Petkovska**, **R. Petrović**, **I. Popović**, **B. Radak**, **S. Ražić**, **D. Sladić**, **S. Sovilj**, **S. Šerbanović**, **B. Šolaja**, **Ž. Tešić**, **D. Trivić**, **V. Vajs, M. Zlatović**.

Subscription: The annual subscription rate is **150.00 €** including postage (surface mail) and handling. For Society members from abroad rate is **50.00 €**. For the proforma invoice with the instruction for bank payment contact the Society Office (E-mail: shd@shd.org.rs) or see JSCS Web Site: http://www.shd.org.rs/JSCS/, option Subscription.
Godišnja pretplata: Za članove SHD: **2.500,00 RSD**, za penzionere i studente: **1000,00 RSD**, a za ostale: **3.500,00 RSD**:za organizacije i ustanove: **16.000,00 RSD**. Uplate se vrše na tekući račun Društva: **205-13815-62**, poziv na broj **320**, sa naznakom "pretplata za JSCS".

Nota: Radovi čiji su svi autori članovi SHD prioritetno se publikuju.
Odlukom Odbora za hemiju Republičkog fonda za nauku Srbije, br. 66788/1 od 22.11.1990. godine, koja je kasnije potvrđena odlukom Saveta Fonda, časopis je uvršten u kategoriju međunarodnih časopisa (**M-23**). Takođe, aktom Ministarstva za nauku i tehnologiju Republike Srbije, 413-00-247/2000-01 od 15.06.2000. godine, ovaj časopis je proglašen za publikaciju od posebnog interesa za nauku. **Impact Factor** časopisa objavljen za 2024. godinu je **0,700**, a petogodišnji **Impact Factor 0,900**.

Journal of the Serbian Chemical Society
JSCS-info@shd.org.rs • www.shd.org.rs/JSCS

J. Serb. Chem. Soc. Vol. 91, No. 5 (2026)

CONTENTS*

Published by the Serbian Chemical Society
Karnegijeva 4/III, P.O. Box 36, 11120 Belgrade, Serbia
Printed by the Faculty of Technology and Metallurgy
Karnegijeva 4, P.O. Box 35-03, 11120 Belgrade, Serbia

* For colored figures in this issue please see electronic version at the Journal Home Page: http://www.shd.org.rs/JSCS/

Journal of the Serbian Chemical Society
JSCS@tmf.bg.ac.rs • www.shd.org.rs/JSCS
J. Serb. Chem. Soc. 91 (5) 441–455 (2026)
JSCS–5502
Original scientific paper
Published 12 June, 2026

Syntheses and computational analyses of selected macrolide derivatives derived from clarithromycin A

BILJANA B. ARSIC[1,2]*, GARETH A. MORRIS[3], ABDOLREZA HASSANZADEH[2,4], OLGA P. JOVANOVIC[1], JILL BARBER[2] and DJORDJE GLISIN[1]

[1]*University of Nis, Faculty of Sciences and Mathematics, Department of Chemistry, Visegradska 33, Nis, Serbia,* [2]*Division of Pharmacy and Optometry, School of Health Sciences, University of Manchester, Manchester, United Kingdom,* [3]*Department of Chemistry, University of Manchester, Manchester M13 9PL, United Kingdom and* [4]*Pharmaceutics Research Center, Institute of Pharmaceutical Sciences, Kerman University of Medical Sciences, Kerman, Iran*

(Received 4 November, revised 17 November 2025, accepted 6 April 2026)

Abstract: This study presents the synthesis and experimental and computational analysis of novel macrolide derivatives obtained from clarithromycin A, with the aim of exploring their potential to address the growing problem of antimicrobial resistance. The compounds synthesized include 2′-*O*-acetyl-clarithromycin A, its phosphoramidite derivative, and the corresponding phosphonyl derivative. Special attention was paid to the optimization of phosphitylation conditions due to the inherent instability of phosphoramidite compounds. The purity of the phosphoramidite derivative was successfully confirmed using diffusion-ordered NMR spectroscopy (DOSY). Comprehensive conformational analyses were carried out using molecular modeling techniques, followed by molecular docking and MM-GBSA calculations with a target protein from *Escherichia coli* to evaluate the relative binding affinities of clarithromycin A and its derivatives. The results indicate that the phosphoramidite and phosphonyl derivatives exhibit comparable binding affinities relative to the parent antibiotic. In addition, complex mass spectrometric fragmentation patterns of the phosphorus-containing derivatives were analyzed and rationalized using the MS Fragmenter computational tool.

Keywords: macrolide antibiotics; DOSY; synthesis; phosphoramidites; molecular docking.

INTRODUCTION

Rising antimicrobial resistance is a huge threat to human health.[1] A recent example is the hospital-acquired and ventilator-associated life-threatening pneumonia caused by *Acinetobacter*.[2] There are numerous initiatives to overcome the

* Corresponding author. E-mail: biljana.arsic@pmf.edu.rs
https://doi.org/10.2298/JSC251104018A

resistance problem, and one of them is a new antibiotic class (representatives SPR719 and its prodrug SPR720, gyrase B inhibitors) with a novel mechanism of action.[3] The prodrug SPR720 (fobrepodacin) is a phosphate derivative (Fig. 1), which encourages the synthesis of other phosphate derivatives. We are here interested in the synthesis of their precursors – phosphoramidites.

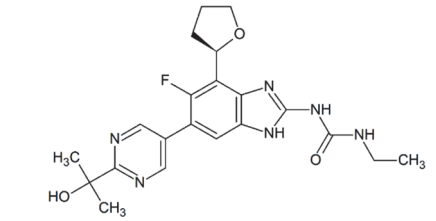

SPR719

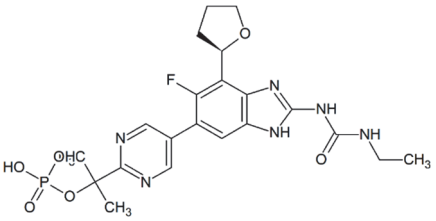

SPR720

Fig. 1. Structures of SPR719 and its prodrug, SPR720.

Phosphoramidite compounds are made in one of two ways, using the reagents 2-cyanoethyl diisopropylchlorophosphoramidite or 2-cyanoethyl *N*,*N*,*N*′,*N*′-tetraisopropylphosphorodiamidite. Successful phosphitylation of modified nucleosides at the 3´ position with 2-cyanoethyl *N*,*N*,*N*,*N*-tetraisopropylphosphorodiamidite in the presence of *N*,*N*-diisopropylamine tetrazolide in acetonitrile gave synthetic blocks in significant yields (52–86 %).[4] In the case of 2-cyanoethyl diisopropylchlorophosphoramidite, a mild base must be used, and the reaction time varied between 1–5 h.[5] Therefore, triethylamine has also been used as a base giving high yield of the synthesized compound (95 %).[6] DMAP has also been used to catalyse phosphorylations.[7] Cyanoethyl protection can be easily removed by piperidine in anhydrous acetonitrile, followed by addition of potassium carbonate solution in methanol[8,9] or by concentrated ammonia.[10]

The aim of the current work was to synthesize acetyl and phosphoramidite derivatives of clarithromycin A (usually known as clarithromycin), Fig. 2.

DOSY NMR was used in the case of the phosphoramidite derivative of acetyl clarithromycin A to show the purity of the synthesized compound.[11] Conformational analysis for the macrolide antibiotics (Fig. 3) gives insight into their possible biological conformations. Molecular docking was performed for clarithromycin A and compounds **1**–**3** with the target protein from *Escherichia coli*, and the relative

affinity of the investigated compounds was further explored using molecular mechanics/generalized Born surface area (MM/GBSA).

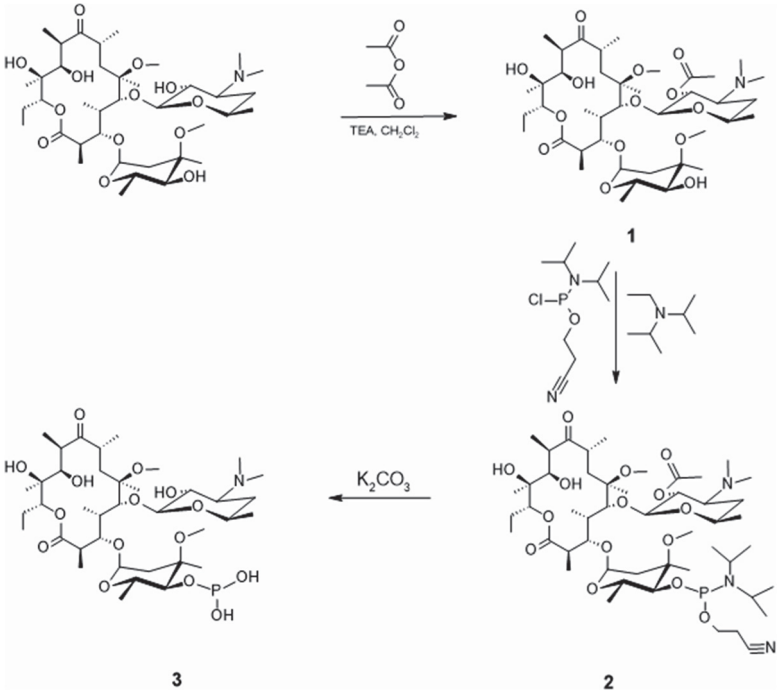

Fig. 2. Scheme for the synthesis of compounds **1**–**3**.

The complicated mass fragmentation patterns observed for 2′-*O*-acetyl-4″-*O*--(2-cyanoethyldiisopropylphosphoramidite)-clarithromycin A (**2**) and 4″-*O*-phosphonyl-clarithromycin A (**3**) with ES^+ were analysed using the computational tool MS Fragmenter 2023.1.1 (ACD/Labs, Canada) and are explained here in detail.

EXPERIMENTAL

Instrumentation

NMR spectrometers. NMR spectra were recorded using a Bruker Avance-300 spectrometer (7.05 T, Bruker, Billerica, MA, USA) equipped with a 5 mm single-axis *Z*-gradient four--nucleus probe, operating at 300 MHz for ^{1}H, 75 MHz for ^{13}C and 121 MHz for ^{31}P. The spectrometer was operated using the XWIN NMR system software. Chemical shifts (δ) are reported in ppm, with peak positions relative to Me_4Si (0 ppm) as internal reference for ^{1}H and ^{13}C.

A Varian Unity 500 NMR spectrometer (Varian Inc., Palo Alto, CA, USA) was operated with an 11.74 T Oxford Instruments magnet. In this field, the ^{1}H resonated at 500 MHz. A 5 mm pulse field gradient (PFG) probe was used. The temperature was controlled using the Varian VT unit with a precision of ±0.1 °C.

Mass spectrometer. Electrospray ionisation-mass spectra (ESI-MS) were acquired on a Micromass Platform mass spectrometer (Waters Corporation, Milford, MA, USA), and data were analysed using the program PLATFORM with a Masslynx data system. The sample (10

μL) was injected using a Hewlett Packard auto-sampler, and the machine was operated at a cone value of 30 eV, at 80 °C.

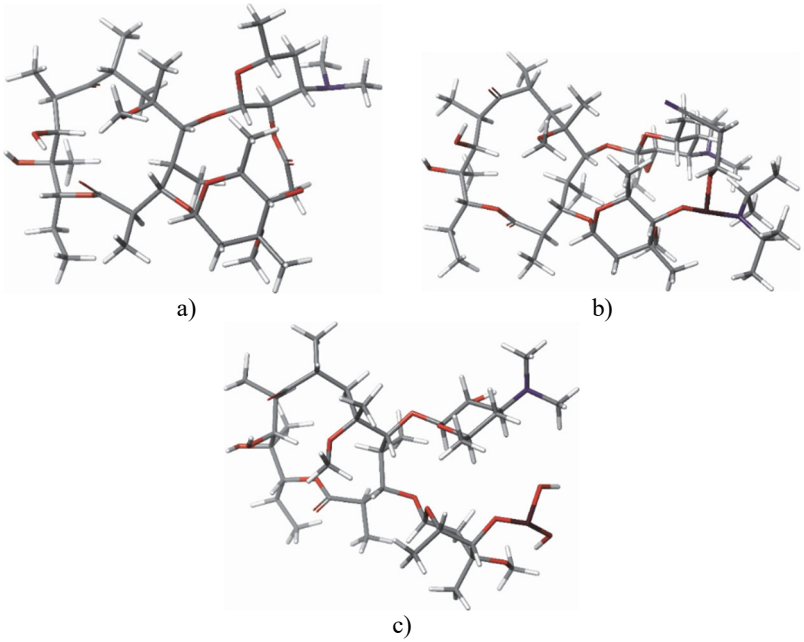

Fig. 3. Structure of: a) 2′-*O*-acetyl-clarithromycin A (**1**); b) 2′-*O*-acetyl-4″-*O*-(2-cyanoethyl-diisopropylphosphoramidite)-clarithromycin A (**2**); c) 4″-*O*-phosphoryl-clarithromycin A.

Melting point apparatus. All melting points were determined using a Bibby SMP-10 (Stuart Scientific, Staffordshire, UK) melting point apparatus and were reported uncorrected. The samples were placed in a capillary tube and inserted in the melting point apparatus and were heated at a rate of 1 °C min^{-1} until the compound melted.

Two-dimensional NMR spectroscopy

HMQC and HMBC. Heteronuclear multiple bond connectivity (HMBC) and heteronuclear multiple quantum coherence (HMQC) spectra were acquired on the Varian Unity 500 spectrometer. An HMBC spectrum gives a two-dimensional spectrum, with ^{13}C chemical shifts on one axis and ^{1}H chemical shifts on the other, correlating spins coupled through multiple bonds; HMQC correlates ^{13}C and ^{1}H through one-bond couplings.

DOSY. High resolution diffusion-ordered spectroscopy (DOSY) data were acquired using the ONESHOT DOSY pulse sequence. Twelve spectra were acquired, with gradient pulse durations of 2.9 ms and nominal gradient amplitudes ranging from 6 to 63 G cm^{-1} in equal steps of gradient squared. The free induction decay deconvolution for line shape enhancement (FIDDLE) algorithm[12] was used to correct line shapes using TSP as a reference standard. DOSY spectra were constructed after baseline correction by taking the first echo spectrum and distributing the intensities of the individual signals in the second dimension according to their respective diffusion coefficients.[13,14]

Synthetic procedures

2′-O-*Acetyl-clarithromycin A (**1**).* The compound 2′-*O*-acetyl-clarithromycin A (**1**) was synthesized according to previously published procedure.[15] A solution of clarithromycin A (0.0972 g, 0.13 mmol) and triethylamine (0.16 mmol) in dichloromethane was cooled in an ice--water bath. Acetic anhydride (0.27 mmol) was added to the solution, the bath was removed, and the reaction was stirred for 5.5 h at room temperature. The reaction was monitored using TLC, with mobile phase dichloromethane:ethyl acetate:ethanol = 5:5:2, and the plate was sprayed with the mixture *p*-anisaldehyde:ethanol:conc. sulfuric acid = 1:9:1. A solution of 0.5 M NaH_2PO_4 was added to the reaction mixture and the aqueous layer was separated. The aqueous phase was extracted three times with chloroform. The combined organic extracts were dried ($MgSO_4$) and concentrated under reduced pressure to give crude product which was recrystallized from acetonitrile, affording 0.0704 g (yield 68.6 %).

2′-O-*Acetyl-4″*-O-*(2-cyanoethyldiisopropylphosphoramidite)-clarithromycin A (**2**)*. Method A: 2′-*O*-acetyl-clarithromycin A (**1**, 0.1074 g, 0.14 mmol) was dissolved in dry dichloromethane (dried over thermally treated Al_2O_3) in an atmosphere of dry nitrogen. Then 60.7 μL (0.28 mmol) of 2-cyanoethyl *N*,*N*-diisopropylchlorophosphoramidite (ρ = 1.061 g mL^{-1}) was added, followed by 94.8 μL of *N*-ethyldiisopropylamine (ρ = 0.742 g mL^{-1}, 0.56 mmol). Then 0.0024 g (0.02 mmol) 4-dimethylaminopyridine was added and the reaction mixture was stirred. The reaction was monitored using TLC every 15 min during 2 h, with mobile phase dichloromethane:ethyl acetate:ethanol = 5:5:2, and the plate was sprayed with the mixture *p*-anisaldehyde:ethanol:conc. sulfuric acid = 1:9:1. The reaction was left with stirring overnight at room temperature. Then a few drops of absolute ethanol were added, followed by aqueous saturated $NaHCO_3$, and the extraction was performed with dichloromethane. The organic layer was dried over anhydrous sodium sulfate. A crude product was obtained after vacuum evaporation and kept at –21 °C. MS (ES^+) (*m/z*): $[M+K]^+$ 1028. Mass spectrum (ES^+) is available in the Supplementary material to this paper (Fig. S-2). NMR spectra (^1H, HMBC, HMQC) recorded at 500 MHz for the crude product are not shown.

Method B: 2′-*O*-acetyl-clarithromycin A (**1**, 0.1000 g, 0.13 mmol) was dissolved in dry dichloromethane in an atmosphere of dry nitrogen. Then, using an automated pipette, 141.4 μL 2-cyanoethyl *N*,*N*-diisopropylchlorophosphoramidite (ρ = 1.061 g mL^{-1}, 0.65 mmol) was added, and 176.6 μL of *N*-ethyldiisopropylamine (ρ = 0.742 g mL^{-1}, 1.04 mmol). The reaction mixture was monitored using TLC every 15 min during 2 h, with mobile phase dichloromethane:ethyl acetate:ethanol = 5:5:2, and the plate was sprayed with the mixture *p*-anisaldehyde:ethanol:conc. sulfuric acid = 1:9:1. The reaction was left overnight stirring. MS (ES^+) (*m/z*): M^+ 989. Mass spectrum (ES^+) is available in the Supplementary material (Fig. S-3).

4″-O-*Phosphonyl-clarithromycin A (**3**).* 2′-*O*-Acetyl-4″-*O*-(2-cyanoethyldiisopropyl-phosphoramidite)-clarithromycin A (**2**, 0.5165 g, 0.52 mmol) was dissolved in 15 mL acetone, 10 mL methanol and 5 mL water. The mixture was left at room temperature overnight, then a saturated solution of potassium carbonate was added. Afterwards, the reaction mixture was extracted with methylene chloride three times and then dried over anhydrous sodium sulphate. Filtration was performed, and evaporation with a vacuum evaporator, giving 0.1465 g 4″-*O*-phosphonyl-clarithromycin A (**3**, yield 34.7 %). MS (ES^+) (*m/z*): $[M-63]^+$ 748. Mass spectrum (ES^+) is available in the Supplementary material (Fig. S-4).

Conformational analysis

Unconstrained conformational search. SMILES string from PubChem was used for the generation of 3D structure of clarithromycin A. A 3D structure of 2′-*O*-acetyl derivative of

clarithromycin A was constructed using 2D Sketcher (Beta) option. Their unconstrained conformational analyses were performed using MacroModel under the Schrodinger Suite 2025-4 and with Maestro 14.6 as the interface. Chloroform was used as the solvent. The minimizations were first performed with charges from the force field (AMBER*),[16] the cut-off was extended, the minimization method was truncated Newton conjugate gradient (TNCG), and the maximum number of iterations was set to 10,000, with the gradient convergence, and its threshold of 0.05. AMBER* force field was used previously for this type of macrocycle as the results of the conformational analysis showed good agreement with NMR data.[17] Conformational search torsional sampling was Monte Carlo multiple minimum (MCMM) with automatic setup during the calculation, and torsion sampling options were set to intermediate. The maximum number of steps was 10,000, with 100 steps per rotatable bond. The number of structures to be saved for each search was 100, energy window for saving structures was 21 kJ/mol, and the maximum atom deviation cut-off was 0.5 Å. In the case of 2′-*O*-acetyl-4″-*O*-(2-cyanoethyldiisopropyl-phosphoramidite)-clarithromycin A (**2**), minimization and unconstrained conformational search were performed in Macromodel using MMFFs force field and chloroform as solvent, with the previously found parameters for the minimization and unconstrained conformational analysis of clarithromycin A and 2′-*O*-acetyl derivative of clarithromycin A. AMBER* force field does not contain the parameters for phosphorus containing compounds like from this study, so MMFFs was chosen as a force field as it provides good agreement with the experimental data on this type of compounds.[18] MMFFs force field was used in the minimization and the conformational analysis of 4″-*O*-phosphoryl-clarithromycin A as well.

Constrained conformational search. Constrained conformational search was performed on clarithromycin A and macrolides **1**–**3** starting from the global minima of the unconstrained search of the investigated compounds and using the same parameters as for unconstrained conformational search with the distance constraints (H4–H11, H5–H18 and H15–H16 was constrained to 2.5±0.3 Å).

Molecular docking

The molecular docking studies with selected compounds (clarithromycin A (6-*O*-methyl erythromycin A), compounds **1**–**3**) were performed using protein chain from *Escherichia coli* as a target interacting with co-crystalized erythromycin A (entry 4V7U[19] from Protein Data Bank) in folded-out conformation. They were achieved at the binding site of erythromycin A in *E. coli*. Protein chain was prepared for docking using the Protein Preparation and Refinement tool of Schrodinger Suite 2025-4. The previously optimized structures of clarithromycin A and compounds **1**–**3** in MacroModel through constrained conformational search were ligands in the molecular docking studies. Molecular docking was performed with Glide under Schrodinger Suite 2025-4.

MM-GBSA studies

MM-GBSA studies were conducted on docking complexes of ligands (clarithromycin A, compounds **1**–**3**) and the target-protein chain from *E. coli* using Prime under Schrodinger Suite 2025-4. Solvation model was VSGB and used force field was OPLS 4.

Rules-based fragment prediction for mass spectrometry

MS Fragmenter[20] was used for the prediction of mass spectral fragmentation of 2′-*O*-acetyl-4″-*O*-(2-cyanoethyldiisopropylphosphoramidite)-clarithromycin A (**2**) and 4″-*O*-phosphonyl-clarithromycin A (**3**). The compounds **2** and **3** were drawn, and then ionization polarity and fragmentation options were selected.

RESULTS AND DISCUSSION

*Synthesis of the phosphoramidite derivative of 2′-*O*-acetyl-clarithromycin A*

There are many published syntheses[21] of acetyl derivatives of macrolide antibiotics (such as 2′-*O*-acetyl-(10*E*)-10,11-ene-11-deoxy-clarithromycin), but there are no available data on the synthesis of the phosphoramidite derivatives. Phosphoramidites are unstable, and preferably stored under an inert atmosphere at −20 °C to minimize oxidation and hydrolysis.[22] Although stored at –21 °C prior to NMR analysis, the phosphoramidite derivative of 2′-*O*-acetyl-clarithromycin A showed several signals in the ^{31}P-NMR spectrum. A simple experiment with water, 2-cyanoethyl *N*,*N*-diisopropylchlorophosphoramidite and *N*-ethyldiisopropylamine showed that the reagent is not so easily degradable (^{31}P δ 15.4 ppm) and that there are numerous products with various chemical shifts (Fig. S-5 in the Supplementary material). The most intense can be observed at δ 3.4 ppm (^{31}P). 2′--*O*-Acetyl clarithromycin A did not show any reaction towards phosphoramidite derivative in 1 day when there was no catalyst in the system. After 1 day when 2-cyanoethyl *N*,*N*-diisopropylchlorophosphoramidite was in 5-fold excess, the desired product appeared (^{31}P δ 7 ppm) (Fig. S-6 in the Supplementary material). The same result was achieved with: 1) DMAP (4-dimethylaminopyridine) as a catalyst (Fig. S-7 in the Supplementary material), 2) on heating on 40 °C under reflux (Fig. S-8 in the Supplementary material), 3) in ratio of 2-cyanoethyl *N*,*N*-diisopropylchlorophosphoramidite and the substrate of 0.95:1, and the ratio of base to the reagent of 2:1 and 4) iodine as a catalyst. *N*-ethyldiisopropylamine causes some slight changes in 2-cyanoethyl *N*,*N*-diisopropylchlorophosphoramidite, particularly if the reaction requires longer time, so other bases are preferred. The synthesis of 4″-*O*-phosphonyl-clarithromycin A (**3**) was easily achieved.

*DOSY NMR analysis of the purity of the synthesized compound:2′-O-acetyl-4″--O-(2-cyanoethyldiisopropylphosphoramidite)-clarithromycin A (**2**)*

Diffusion-ordered NMR spectroscopy (DOSY) is a method for distinguishing between the NMR signals of (macro)molecules of different molecular weights present in solution at millimolar concentrations.[23] The number of components identifiable in solution is limited only by resolution.[24,25]

The purity of the synthesized compound, 2′-*O*-acetyl-4′′-*O*-(2-cyanoethyl-diisopropylphosphoramidite)-clarithromycin A using DMAP as a catalyst was checked using DOSY NMR at 500 MHz. The recorded spectrum revealed several compounds with different diffusion coefficients (Fig. 4), however, most of the signals with different diffusion coefficients belong to solvent and reagents used. A line of signal at diffusion coefficient ($3–4\times10^{-10}$ m^2 s^{-1}) shows chemical shifts characteristic of macrolides,[26] suggesting the presence of a single compound with, crucially, no degradation products, such as cladinose.

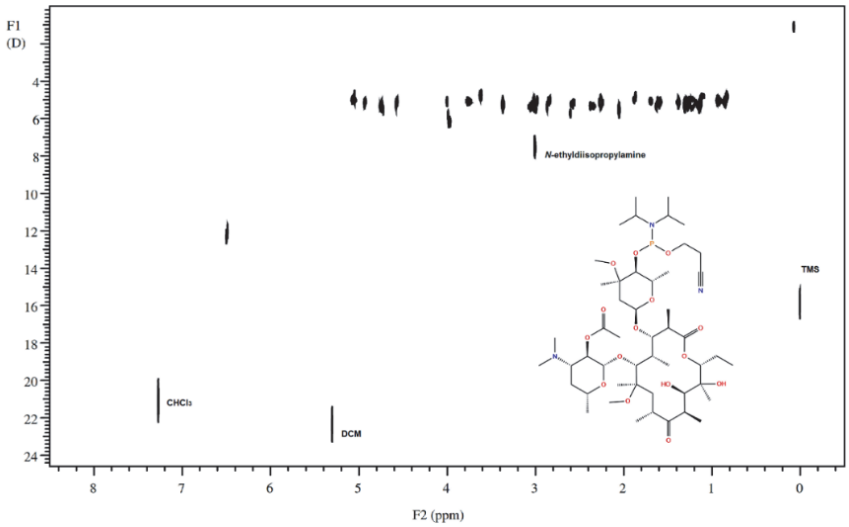

Fig. 4. DOSY NMR spectrum at 500 MHz of 2′-*O*-acetyl-4″-*O*-(2-cyanoethyldiisopropyl-phosphoramidite)-clarithromycin A (**2**).

Conformational analysis

Unconstrained conformational analysis of clarithromycin A, 2′-*O*-acetyl-clarithromycin A (**1**) and 2′-*O*-acetyl-4″-*O*-(2-cyanoethyldiisopropylphosphoramidite)-clarithromycin A (**2**) gave as global minima folded-out[17,27] structures (H4––H11 (2.90 Å), H5–H18 (2.36 Å) and H15–H16 (2.94 Å) in the case of clarithromycin A; H4–H11 (2.88 Å), H5–H18 (2.36 Å) and H15–H16 (2.95 Å) in the case of 2′-*O*-acetyl-clarithromycin A (**1**); H4–H11 (3.03 Å), H5–H18 (2.44 Å), H15––H16 (2.91 Å) in the case of 2′-*O*-acetyl-4″-*O*-(2-cyanoethyldiisopropylphosphoramidite)-clarithromycin A (**2**)). A longer distance H15–H16 than 2.8 Å in the case of clarithromycin A, 2′-*O*-acetyl-clarithromycin A (**1**) and 2′-*O*-acetyl-4″-*O*--(2-cyanoethyldiisopropylphosphoramidite)-clarithromycin A (**2**) is not so significant, owing to the possibility of free rotation of methyl groups, which obviously does not require a high amount of energy. Conformational analysis of 4″-*O*-phosphoryl-clarithromycin A did not give a folded-out structure of the global minimum (H4–H11 (5.18 Å), H5–H18 (2.94 Å) and H15–H16 (5.79 Å)). The analysis of the conformational landscapes, low-energy conformers, and relative populations of clarithromycin A and macrolide antibiotics (**1**–**3**) reflects the known conformational diversity of macrolides (Table I).

Our previously published work on erythromycin A and clarithromycin A (6-*O*-methyl erythromycin A) shows that their active conformations, when bound weakly to bacterial (*E. coli*) ribosomes, are folded-out conformations.[17] Obtained clarithromycin A conformations with the lowest energy-global minima in water

both using Macromodel and SYBYL[17] showed folded-out structure. Unconstrained conformational search on clarithromycin A and compounds **1** and **2** in chloroform showed folded-out conformation with negligible longer H4–H11 distance from 2.8 Å. However, compound **3** showed completely different conformation. Since biologically active conformation of clarithromycin A is folded-out, all four compounds (clarithromycin A and compounds **1**–**3**) were put for constrained conformational search, and obtained global minima were used in further computational studies.

TABLE I. Global minima energies and their number of times, and the population of folded-out in the first ten lowest energy conformations as results of the unconstrained conformational search, as well as global minima energies and their number of times as results of constrained conformational search

Compound	Unconstrained conformational search			Constrained conformational search	
	Global minimum		Population of folded-out in the first ten lowest energy conformations	Global minimum	
	Energy kJ/mol	Number of times		Energy kJ/mol	Number of times
Clarithromycin A	85.78	13	4/10	130.57	19
2′-*O*-Acetyl-clarithromycin A (**1**)	26.17	23	6/10	76.26	10
2′-*O*-Acetyl-4″-*O*-(2-cyanoethyldiisopropylphosphoramidite)-clarithromycin A (**2**)	464.99	2	3/10	521.97	15
4″-*O*-Phosphonyl-clarithromycin A (**3**)	493.64	8	0/10	516.28	29

Molecular docking

Macrolide antibiotics inhibit bacterial protein synthesis by reversibly binding to the 50S subunit of the bacterial ribosome. This binding blocks the ribosomal exit tunnel near the peptidyl transferase center, thereby preventing elongation of the growing peptide chain.[28]

Due to the reason that there is no available crystal structure of clarithromycin A with the ribosomal bacterial proteins, the crystal structure of erythromycin A with *E. coli* ribosome was used for the molecular docking study (PDB ID: 4V7U).[19] Clarithromycin A (6-*O*-methyl erythromycin A) is a semi-synthetic macrolide derived from erythromycin A.

Erythromycin A shows folded out conformation in the bound state in the crystal structure with ribosome of *E. coli:* H4–H11 (2.42 Å), H5–H18 (2.65 Å) and H15–H16 (3.12 Å). It established interactions with amino-acids residues Ala 89,

Lys 90, Gly 91 and Arg 92. These data were used for the molecular studies with clarithromycin A and compounds **1**–**3**.

Molecular docking studies on clarithromycin A and compounds **1**–**3** show quite different Glide scores (Table II). Compounds **2** and **3** showed better inhibition compared to clarithromycin A.

TABLE II. Glide scores from molecular docking and Δ*G*_bind energies from MM-GBSA studies for the investigated compounds

Compound	Glide score kJ/mol	Δ*G*_bind energy kJ/mol
Clarithromycin A	–0.13	–83.30
2′-*O*-Acetyl-clarithromycin A (**1**)	0.33	–34.52
2′-*O*-Acetyl-4″-*O*-(2-cyanoethyldiisopropylphosphoramidite)-clarithromycin A (**2**)	–2.13	–82.01
4″-*O*-Phosphonyl-clarithromycin A (**3**)	–0.96	–74.81

MM-GBSA studies

MM-GBSA estimates the binding free energy of a ligand–protein complex in a more physically realistic way than simple docking scores. It includes terms for molecular mechanics energies and solvent effects *via* an implicit solvation model. Because of this, MM-GBSA is often more accurate at ranking ligands by binding affinity, especially for lead optimization or for smaller sets of compounds selected after docking.[29,30]A common strategy is to use docking to generate possible binding poses quickly, then apply MM-GBSA to rescore these poses with a more realistic energy model. This helps refine rankings and improve discrimination between strong and weak binders.[31]

Obtained docking complexes of protein chain from *E. coli* and investigated compounds (clarithromycin A and **1**–**3**) were used in MM-GBSA studies. Clarithromycin A and compound **2** were shown to possess similar binding affinities, and less activity was shown by compound **3**, and particularly compound **1** (Table II).

Rules-based fragment prediction for mass spectrometry

Electrospray ionization of 2′-*O*-acetyl-4″-*O*-(2-cyanoethyldiisopropylphosphoramidite)-clarithromycin A (**2**) was performed under two different sets of conditions. In the first case (electrospray), one additional peak was observed which has *m*/*z* equal to 200.2 (Fig. 5a), and which was predicted with MS Fragmenter. In the second case (default conditions), MS Fragmenter successfully predicted the existence of peaks with following *m*/*z* values that were found in experimental ES^+ mass spectra of **2**: 102, 219, 614, 790, 877, 920, 921, 930, 947, 962 (Fig. 5b).

The fragments at *m*/*z* equal to 776, 771, 750, 748, 734 and 198 in the ES^+ mass spectrum of 4″-*O*-phosphonyl-clarithromycin A (**3**) were predicted using MS Fragmenter (Fig. 6).

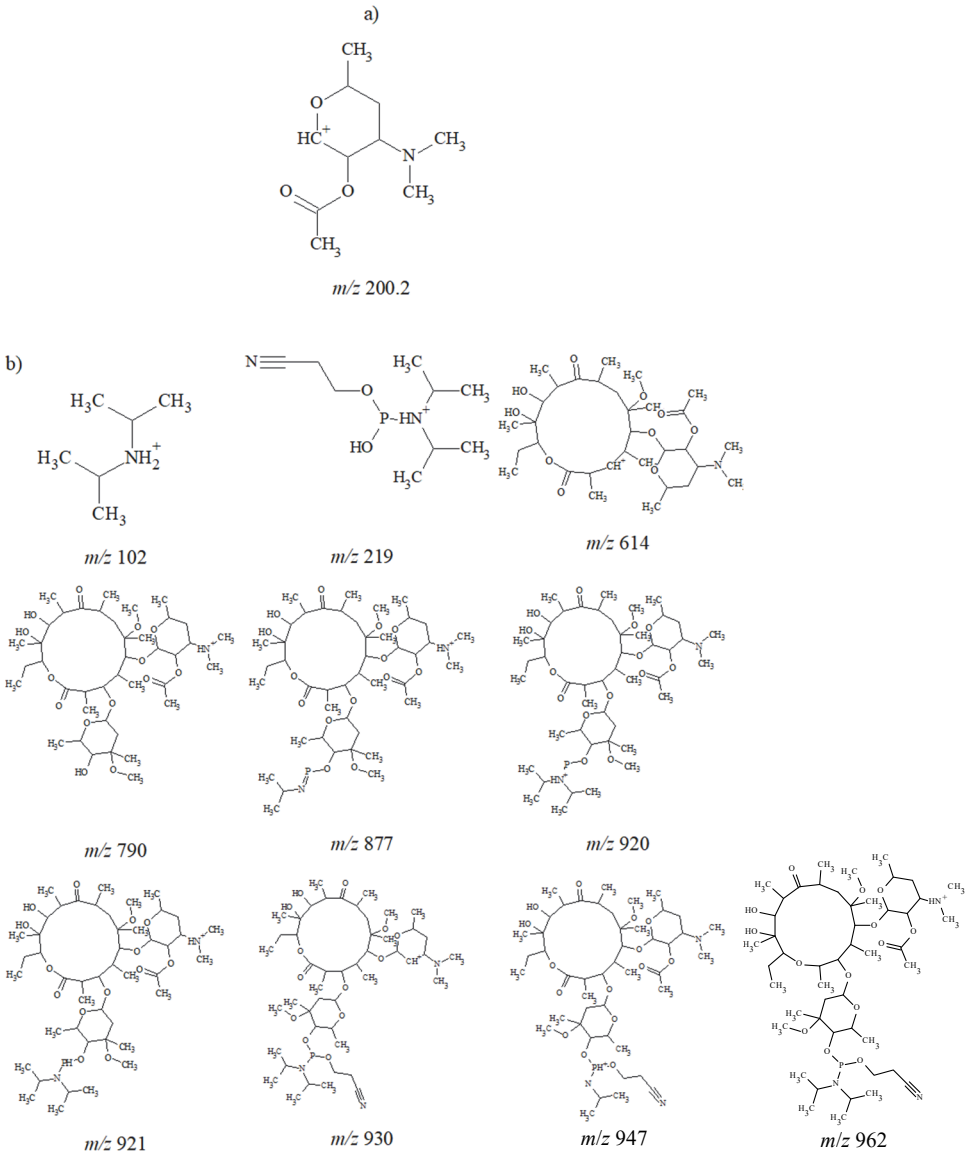

Fig. 5. Fragments of compound **2** predicted using MS Fragmenter: a) a fragment only seen under milder conditions of electrospray ionization; b) fragments seen in mass spectra under default conditions.

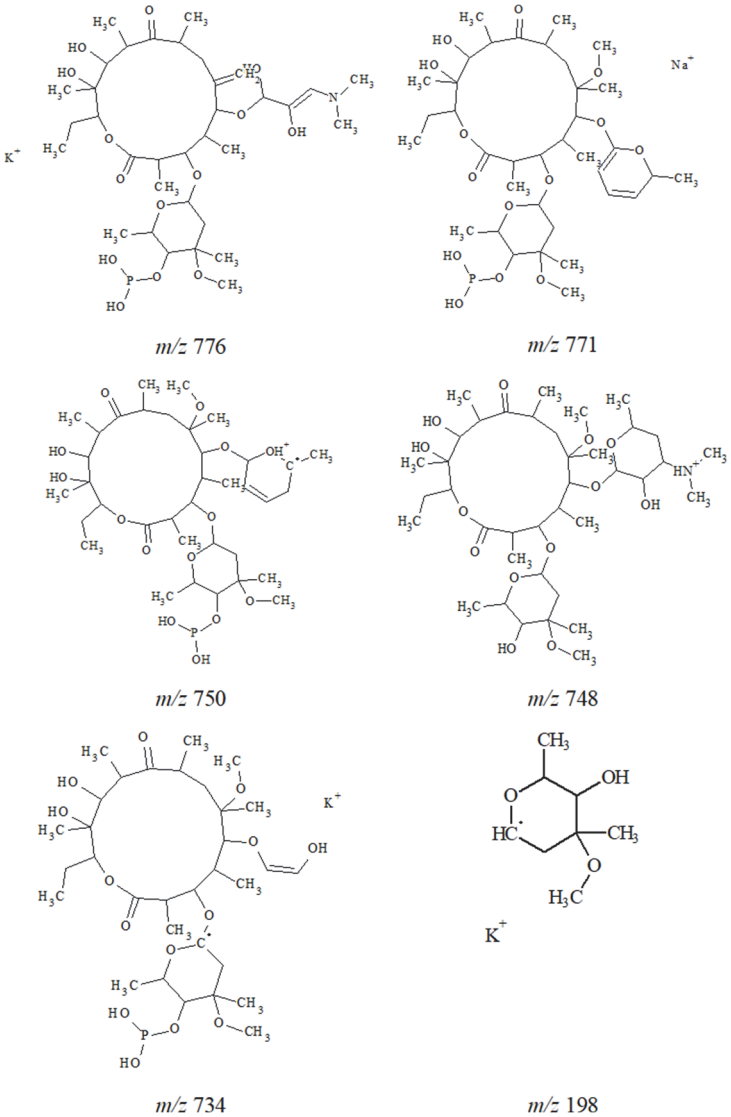

Fig. 6. Fragments in the ES$^+$ mass spectrum of 4″-*O*-phosphonyl-clarithromycin A (**3**) predicted using MS Fragmenter.

CONCLUSION

In this work, clarithromycin A was successfully modified through the introduction of acetyl, phosphoramidite and phosphonyl functional groups, yielding structurally well-characterized macrolide derivatives. The synthesis of the phosphoramidite derivative is particularly significant, given the scarcity of literature data and the challenges associated with its chemical instability. The application of

DOSY NMR spectroscopy proved to be a powerful method for confirming the purity of this complex macrolide derivative. Computational conformational analyses revealed that clarithromycin A and its acetyl and phosphoramidite derivatives predominantly adopt folded-out conformations consistent with the biologically active form known to bind bacterial ribosomes, whereas the phosphonyl derivative displayed a markedly different conformational preference. Molecular docking and MM-GBSA studies further demonstrate that derivatives containing phosphorus-based substituents retain binding affinity toward the ribosomal target when compared to clarithromycin A. Overall, the results highlight chemical modification of macrolide antibiotics as a promising strategy for the development of new compounds with potentially improved pharmacological properties. This study provides a solid foundation for further biological evaluation and supports the future design of novel macrolide-based prodrugs and derivatives aimed at combating antimicrobial resistance.

SUPPLEMENTARY MATERIAL

Additional data and information are available electronically at the pages of journal website: https://www.shd-pub.org.rs/index.php/JSCS/article/view/13617, or from the corresponding author on request.

Acknowledgements. Biljana Arsic gratefully acknowledges financial support from the British Scholarship Trust and The University of Manchester, United Kingdom, to perform various experiments at the University of Manchester, United Kingdom. Special thanks are offered to the mass spectrometry unit at the Department of Chemistry, University of Manchester, for mass analysis of the compounds. Special gratitude goes to Prof. dr Elena V. Bichenkova from the University of Manchester, United Kingdom, for useful discussions on ^{31}P-NMR.

This work is also financially supported by the Ministry of Science, Technological Development and Innovation of the Republic of Serbia (contract numbers: 451-03-47/2023-01/ /200124, 451-03-66/2024-03/200124, 451-03-136/2025-03/200124 and 451-03-33/2026-03/ /200124).Thanks also go to the COST action CA21111-One Health drugs against parasitic vector-borne diseases in Europe and beyond (OneHealthdrugs).

ИЗВОД

СИНТЕЗЕ И КОМПЈУТЕРСКЕ АНАЛИЗЕ ОДАБРАНИХ МАКРОЛИДНИХ ДЕРИВАТА ДОБИЈЕНИХ ИЗ КЛАРИТРОМИЦИНА А

БИЉАНА Б. АРСИЋ[1,2], GARETH A. MORRIS[3], ABDOLREZA HASSANZADEH[2,4], ОЛГА П. ЈОВАНОВИЋ[1], JILL BARBER[2] и БОРЂЕ ГЛИШИН[1]

[1]Универзитет у Нишу, Природно–математички факултет, Департман за хемију, Вишеградска 33, Ниш, [2]Division of Pharmacy and Optometry, School of Health Sciences, University of Manchester, Manchester, United Kingdom, [3]Department of Chemistry, University of Manchester, Manchester M13 9PL, United Kingdom и [4]Pharmaceutics Research Center, Institute of Pharmaceutical Sciences, Kerman University of Medical Sciences, Kerman, Iran

У раду су приказане синтезе и експерименталне и компјутерске анализе нових макролидних деривата добијених из кларитромицина А, са циљем испитивања њиховог потенцијала у превазилажењу проблема антимикробне резистенције. Синтетисани су 2′-

-*O*-ацетил-кларитромицин А, његов фосфорамидитни дериват и одговарајући фосфонилни дериват. Посебна пажња посвећена је оптимизацији услова фосфорилације, с обзиром на нестабилност фосфорамидита. Чистоћа фосфорамидитног деривата потврђена је применом DOSY NMR спектроскопије. Изведене су детаљне конформационе анализе коришћењем молекулског моделирања, као и молекулско доковање и MM-GBSA прорачуни са циљним протеином из Escherichia coli, како би се проценио афинитет везивања синтетисаних једињења. Резултати показују да фосфорамидитни и фосфонилни деривати имају упоредив афинитет везивања у односу на кларитромицин А. Додатно, фрагментација у масеној спектрометрији анализирана је и рационализована применом MS Fragmenter софтвера.

(Примљено 4. новембра, ревидирано 17. новембра 2025, прихваћено 6. априла 2026)

REFERENCES

1. Antimicrobial resistance, https://www.who.int/news-room/fact-sheets/detail/antimicrobial-resistance, accessed on the 19th February 2026
2. I. Kyriakidis, E. Vasileiou, Z. D. Pana, A. Tragiannidis, *Pathogens* **10** (2021) 373 (https://doi.org/10.3390/pathogens10030373)
3. A. K. Talley, A. Thurston, G. Moore, V. K. Gupta, M. Satterfield, E. Manyak, S. Stokes, A. Dane, D. Melnick, *Antimicrob. Agents Chemother.* **65** (2021) (https://doi.org/10.1128/aac.01208-21)
4. T. P. Prakash, A. M. Kawasaki, A. S. Fraser, G. Vasquez, M. Manoharan, *J. Org. Chem.* **67** (2002) 357 (https://doi.org/10.1021/jo0103975)
5. C. Xie, M. A. Staszak, J. T. Quatroche, C. D. Sturgill, V. V. Khau, M. J. Martinelli, *Org. Process Res. Dev.* **9** (2005) 730 (https://doi.org/10.1021/op050077d)
6. C. Wagner, H.-A. Wagenknecht, *Chem. Eur. J.* **11** (2005) 1871 (https://doi.org/10.1002/chem.200401013)
7. G. Hofle, W. Steglich, H. Vorbriiggen, *Angew. Chem. Int. Ed. Engl.* **17** (1978) 569 (https://doi.org/10.1002/anie.197805691)
8. A. P. Guzaev, M. Manoharan, *J. Org. Chem.* **66** (2001) 1798 (https://doi.org/10.1021/jo001591e)
9. W. H. Kuijpers, J. Huskens, L. H. Koole, C. A. van Boeckel, *Nucleic Acids Res.* **18** (1990) 5197 (https://doi.org/10.1093/nar/18.17.5197)
10. N. D. Sinha, J. Biernat, H. Köster, *Tetrahedron Lett.* **24**(52) (1983) 5843 (https://doi.org/10.1016/S0040-4039(00)94216-3)
11. V. Gilard, S. Trefi, S. Balayssac, M.-A. Delsuc, T. Gostan, M. Malet-Martino, R. Martino, Y. Prigent, F. Taulelle, in *NMR Spectroscopy in Pharmaceutical Analysis*, U. Holzgrabe, I. Wawer, B. Diehl, Eds., Elsevier Science, New York, 2008, pp. 269–289 (https://doi.org/10.1016/B978-0-444-53173-5.00011-1)
12. H. Barjat, G. A. Morris, S. Smart, A. G. Swanson, S. C. R. William, *J. Mag. Res. Ser. A* **116** (1995) 206 (https://doi.org/10.1006/jmra.1995.0009)
13. H. Barjat, G. A. Morris, S. Smart, A. G. Swanson, S. C. R. William, *J. Mag. Res. Ser. B* **108** (1995) 170 (https://doi.org/10.1006/jmrb.1995.1118)
14. G. A. Morris, *Diffusion-Ordered Spectroscopy (DOSY)*. *Encyclopedia of Nuclear Magnetic Resonance: Advances in NMR*, John Wiley and Sons, New York, 2009 (https://doi.org/10.1002/9780470034590.emrstm0119.pub2)
15. W. R. Baker, J. D. Clark, R. L. Stephens, K. H. Kim, *J. Org. Chem.* **53** (1988) 2340 (https://doi.org/10.1021/jo00245a038)

16. W. D. Cornell, P. Cieplak, C. I. Bayly, I. R. Gould, K. M. Merz, Jr., D. M. Ferguson, D. C. Spellmeyer, T. Fox, J. W. Caldwell, P. A. Kollman, *J. Am. Chem. Soc.* **117** (1995) 5179 (https://doi.org/10.1021/ja00124a002)
17. B. Arsic, A. Awan, R. J. Brennan, J. A. Aguilar, R. Ledder, A. J. McBain, A. C. Regan, J. Barber, *MedChemComm* **5** (2014) 1347 (https://doi.org/10.1039/c4md00220b)
18. K. S. Watts, P. Dalal, A. J. Tebben, D. L. Cheney, J. C. Shelley, *J. Chem. Inf. Model.* **54** (2014) 2680 (https://doi.org/10.1021/ci5001696)
19. J. A. Dunkle, L. Xiong, A.S. Mankin, J. H. D. Cate, *Proc. Natl. Acad. Sci. U.S.A.* **107** (2010) 17152 (https://doi.org/10.1073/pnas.1007988107)
20. *MS Fragmenter*, version 2023.1.1, Advanced Chemistry Development, Inc. (ACD/Labs), Toronto, ON, Canada, www.acdlabs.com
21. Y. Qin, M. Sun, N. Zhang, Y. Yang, P. Ma, *Bioorg. Chem.* **127** (2022) 106020 (https://doi.org/10.1016/j.bioorg.2022.106020)
22. A. F. Sandahl, T. J. D. Nguyen, R. A. Hansen, M. B. Johansen, T. Skrydstrup, K. V. Gothelf, *Nat. Commun.* **12** (2021) 2760 (https://doi.org/10.1038/s41467-021-22945-z)
23. A. Ambrus, D. Yang, *Anal. Biochem.* **367** (2007) 56 (https://doi.org/10.1016/j.ab.2007.04.025)
24. E. J. Cabrita, S. Berger, *Magn. Reson. Chem.* **40** (2002) S122 (https://doi.org/10.1002/mrc.1082)
25. E. J. Cabrita, S. Berger, P. Brauer, J. Karger, *J. Magn. Reson.* **157** (2002) 124 (https://doi.org/10.1006/jmre.2002.2574)
26. M. N. Mordi, M. D. Pelta, V. Boote, G. A. Morris, J. Barber, *J. Med. Chem.* **43** (2000) 467 (https://doi.org/10.1021/jm9904811)
27. J. R. Everett, J. W. Tyler, *J. Chem. Soc. Perkin Trans. 2* **11** (1987) 1659 (https://doi.org/10.1039/P29870001659)
28. J. Poehlsgaard, S. Douthwaite, *Nat. Rev. Microbiol*. **3** (2005) 870 (https://doi.org/10.1038/nrmicro1265)
29. E. Wang, H. Sun, J. Wang, Z. Wang, H. Liu, J. Z. H. Zhang, T. Hou, *Chem. Rev.* **119** (2019) 9478 (https://doi.org/10.1021/acs.chemrev.9b00055)
30. G. Poli, C. Granchi, F. Rizzolio, T. Tuccinardi, *Molecules* **25** (2020) 1971 (https://doi.org/10.3390/molecules25081971)
31. G. Rastelli, L. Pinzi, *Front. Chem.* **7** (2019) 498 (https://doi.org/10.3389/fchem.2019.00498).

Journal of the Serbian Chemical Society
JSCS@tmf.bg.ac.rs • www.shd.org.rs/JSCS
J. Serb. Chem. Soc. 91 (5) S143–S150 (2026) *Supplementary material*

SUPPLEMENTARY MATERIAL TO

Syntheses and computational analyses of selected macrolide derivatives derived from clarithromycin A

BILJANA B. ARSIC[1,2]*, GARETH A. MORRIS[3], ABDOLREZA HASSANZADEH[2,4], OLGA P. JOVANOVIC[1], JILL BARBER[2] and DJORDJE GLISIN[1]

[1]University of Nis, Faculty of Sciences and Mathematics, Department of Chemistry, Visegradska 33, Nis, Serbia, [2]Division of Pharmacy and Optometry, School of Health Sciences, University of Manchester, Manchester, United Kingdom, [3]Department of Chemistry, University of Manchester, Manchester M13 9PL, United Kingdom and [4]Pharmaceutics Research Center, Institute of Pharmaceutical Sciences, Kerman University of Medical Sciences, Kerman, Iran

J. Serb. Chem. Soc. *91* (5) (2026) 441–455

*2´-O-acetyl-clarithromycin A (**1**).* m.p. 249-251 ºC; 1H NMR (CDCl3) δ 4.75 (dd, CHOAc), 3.37 (s, 3H, C-3´´OCH3), 3.01 (s, 3H, C-6 OCH3), 2.26 (s, 6H, N(CH3)2), 2.05 (s, 3H, OCOCH3), 1.14 (s, 3H, C-12 CH3); 13C NMR (CDCl3) δ 175.7 (C-1), 170 (OCOCH3), 71.8 (C- 2´); MS (ES+) (m/z): [M+H]+ 790. The melting point was in accordance with the previously published value.[1] NMR spectra (1H and 13C) of the compound are available in the Supplementary Material (Figure S-1).

* Corresponding author. E-mail: biljana.arsic@pmf.edu.rs

a)

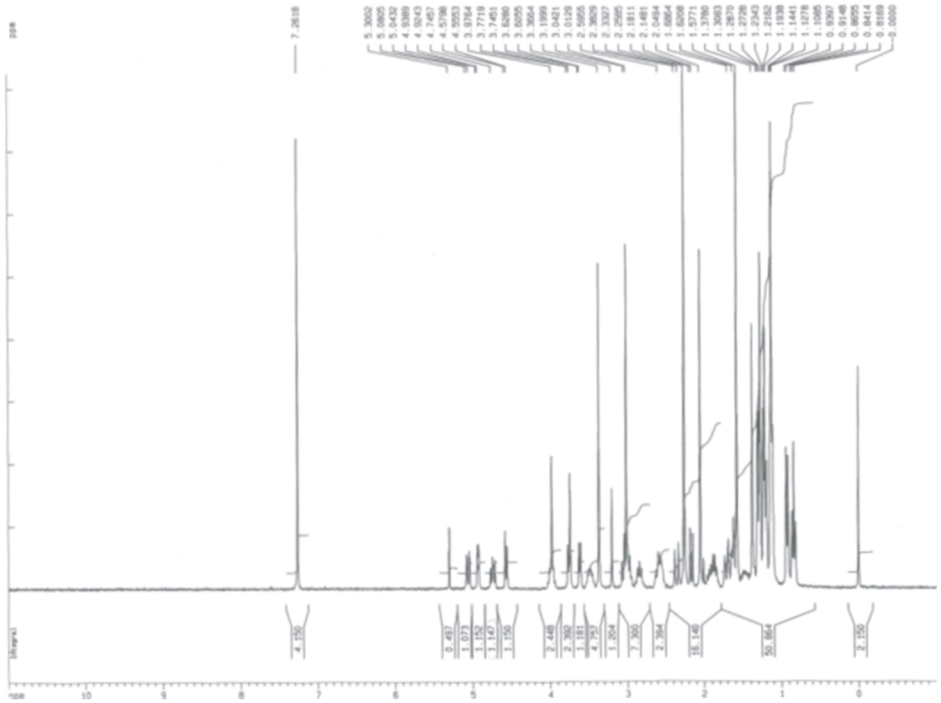

Fig. S-1. a) The ^{1}H NMR spectrum of 2′-*O*-acetyl-clarithromycin A (**1**).

b)

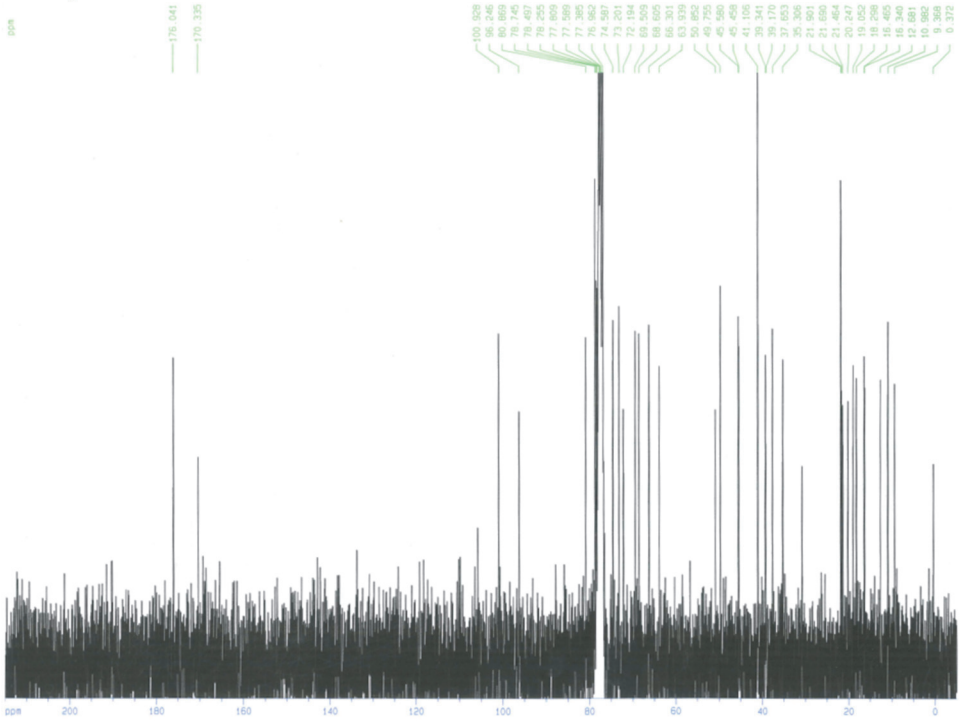

Fig. S-1. b) ^{13}C NMR spectrum of 2′-*O*-acetyl-clarithromycin A (**1**).

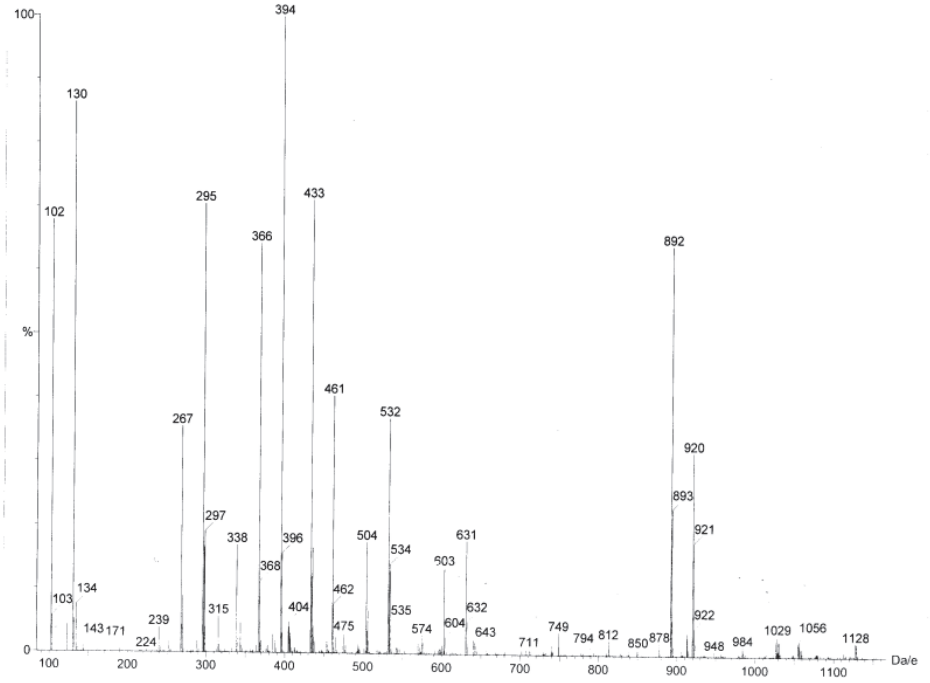

Fig. S-2. Mass spectrum (ES+) of 2′-*O*-acetyl-4"-*O*-(2-cyanoethyldiisopropylphosphoramidite)-clarithromycin A (**2**).

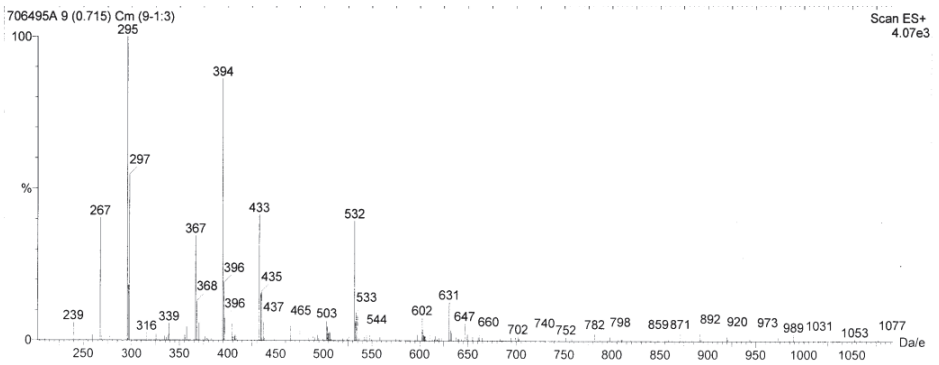

Fig. S-3. Mass spectrum (ES+) of 2′-*O*-acetyl-4′′-*O*-(2-cyanoethyldiisopropylphosphoramidite)-clarithromycin A (**2**).

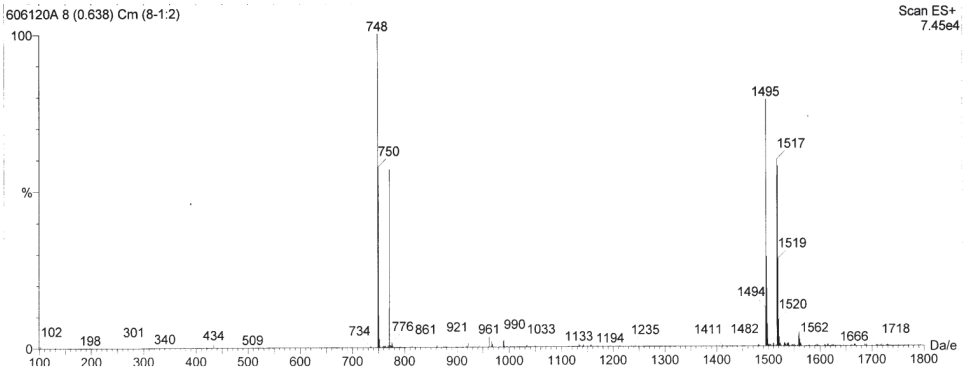

Fig. S-4. Mass spectrum (ES+) of 4´´-*O*-phosphonyl-clarithromycin A (**3**).

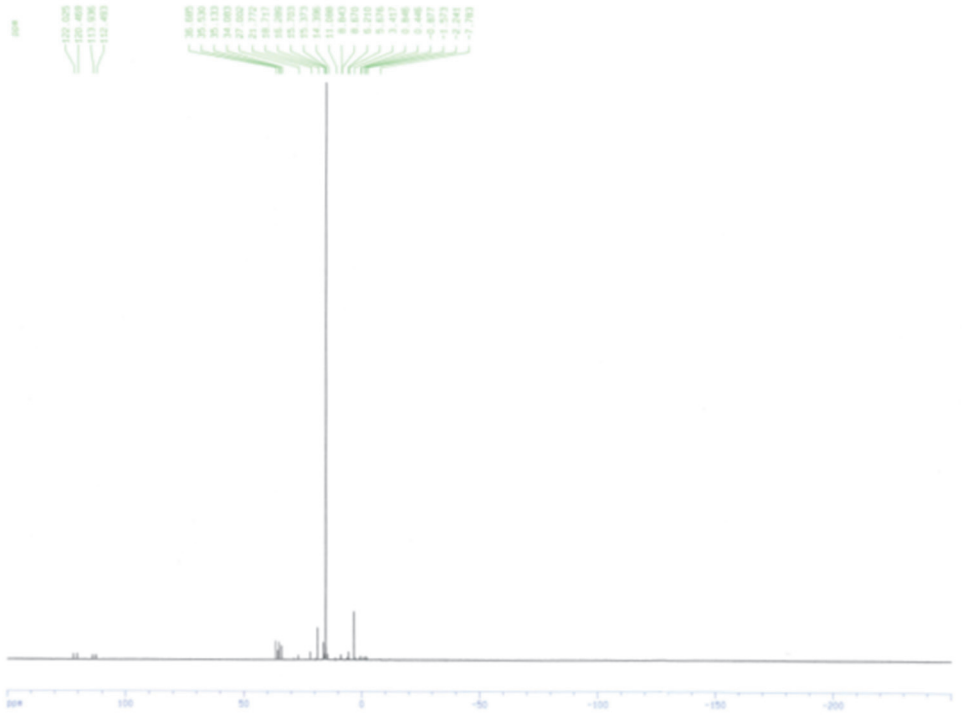

Fig. S-5. ^{31}P NMR spectrum of the mixture 2-cyanoethyl *N,N*-diisopropylchlorophosphoramidite, *N*-ethyldiisopropylamine and water.

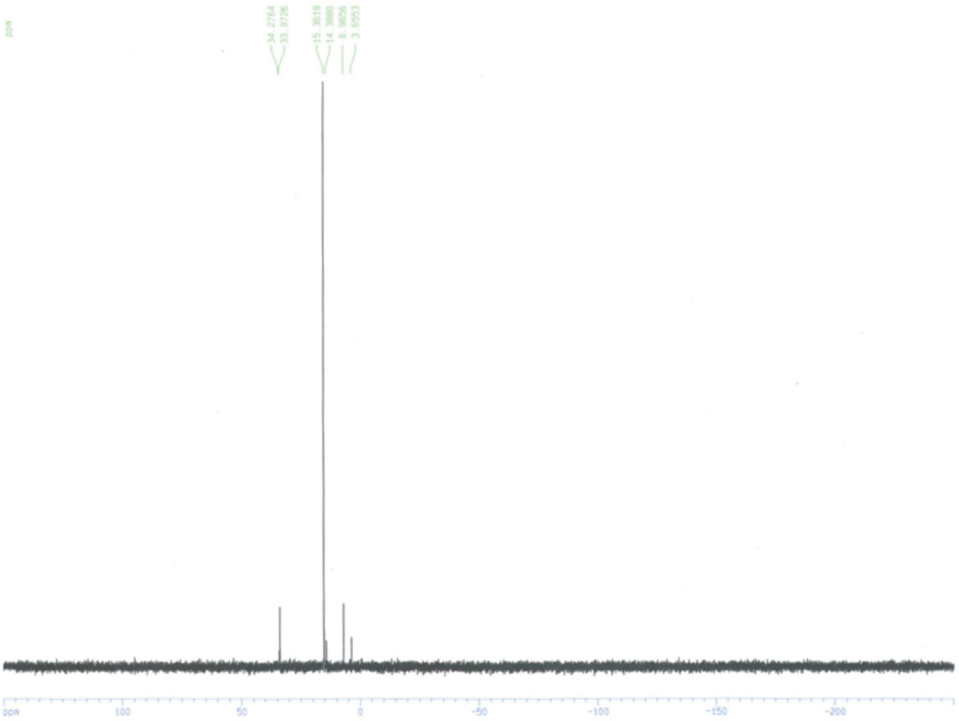

Fig. S-6. ^{31}P NMR spectrum of the reaction mixture after 1 day when 2-cyanoethyl *N,N*-diisopropylchlorophosphoramidite was in 5 fold excess.

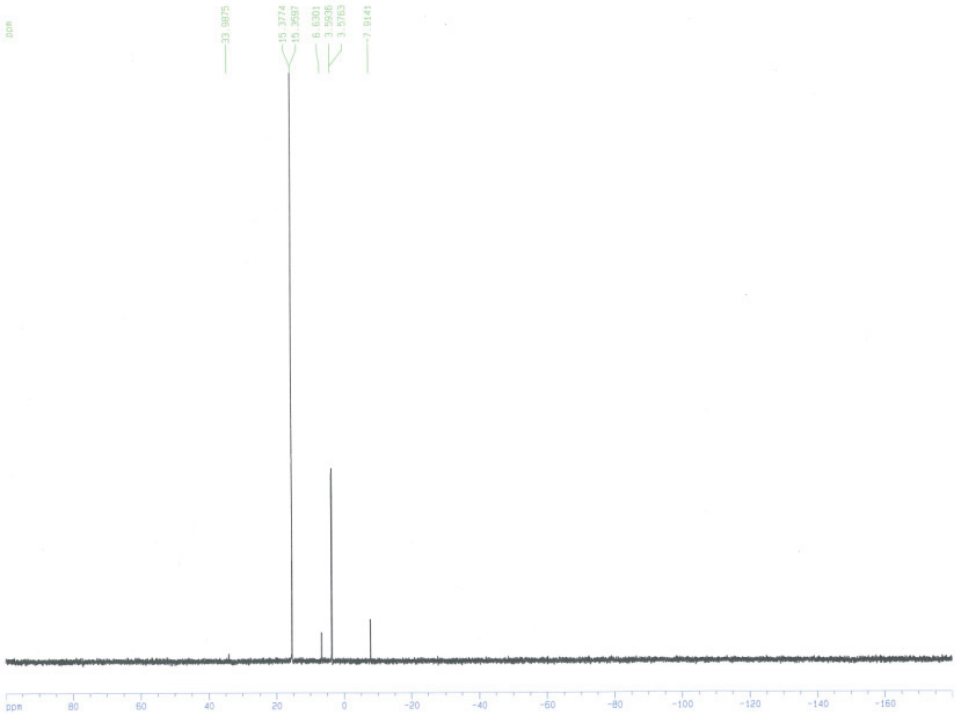

Fig. S-7. ^{31}P NMR spectrum of a reaction mixture with DMAP (4-dimethylaminopyridine) as a catalyst.

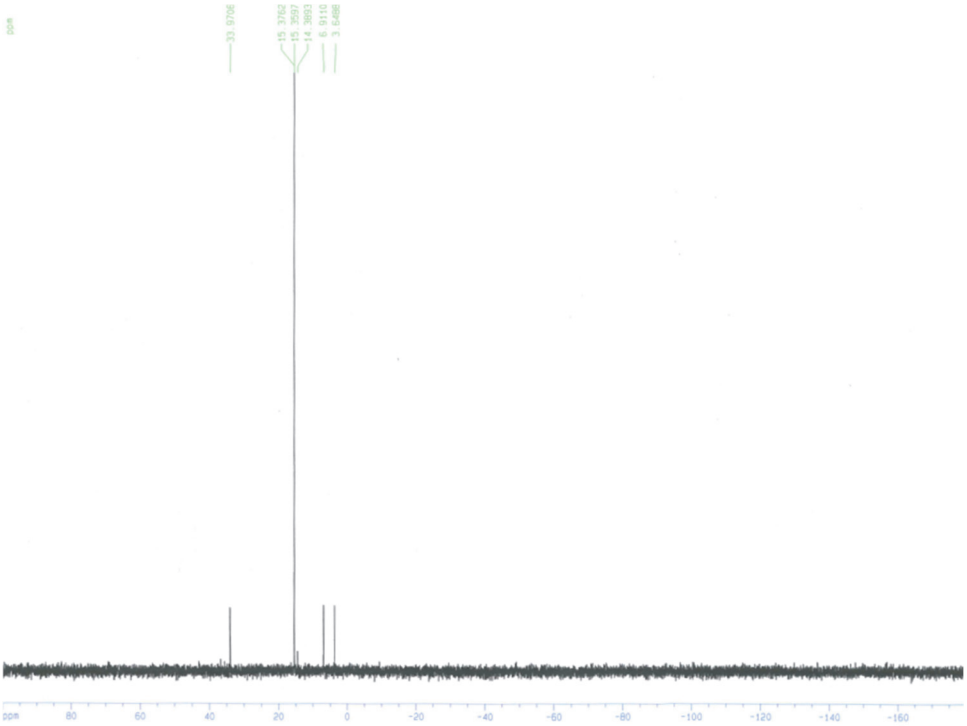

Fig. S-8. ^{31}P NMR spectrum of the reaction mixture on heating at 40 ºC under reflux.

REFERENCES

1. W. R. Baker, J. D. Clark, R. L. Stephens, K. H. Kim, *J. Org. Chem.* **53** (1988) 2340 (https://doi.org/10.1021/jo00245a038).

Journal of the Serbian Chemical Society
JSCS-info@shd.org.rs • www.shd.org.rs/JSCS
J. Serb. Chem. Soc. 91 (5) 457–477 (2026)
JSCS–5503
Original scientific paper
Published 12 June, 2026

In silico modeling of selected phloroglucinol derivatives from *Rhodomyrtus tomentosa*: Mechanistic insights into their potential against cervical cancer

HUNG DUC NGUYEN*

Thai Nguyen University of Education, 24000 Thai Nguyen, Vietnam

(Received 13 December 2025, revised 26 February, accepted 23 March 2026)

Abstract: Cervical cancer remains a major cause of morbidity and mortality worldwide, driven primarily by persistent infection with high-risk HPV types. Natural phloroglucinol derivatives from *Rhodomyrtus tomentosa* have demonstrated anti-cervical cancer potential; however, their apoptosis-related mechanisms remain insufficiently characterized. In this work, selected phloroglucinol derivatives were evaluated as potential inhibitors of the anti-apoptotic Bcl-2 protein (PDB: 6GL8) through an integrated in silico pipeline that combines molecular docking, 100 ns molecular dynamics simulations, MM/GBSA binding free-energy estimation, ADMET profiling, and DFT-based electronic analysis. Docking prioritized CPD1 as the most favorable ligand (–37.36 kJ/mol), outperforming Belzutifan (–25.73 kJ/mol) and engaging the conserved binding pocket. MD trajectories supported stable complex formation across 100 ns. MM/GBSA further indicated stronger binding for CPD1 (ΔTOTAL = –138.78±15.4 kJ/mol) relative to Belzutifan (–63.72±14.31 kJ/mol), primarily due to more favorable gas-phase interactions, while maintaining a comparable solvation term. ADMET predictions suggested similar solubility but higher intestinal absorption for CPD1, alongside a hERG II alert that warrants cardiotoxicity-oriented optimization. DFT descriptors were consistent with the enhanced electrophilic character of CPD1. Collectively, CPD1 is computationally prioritized as a candidate scaffold for follow-up experimental validation and structure-guided refinement.

Keywords: anti-apoptosis; Bcl-2; cervical cancer; molecular modelling; phloroglucinol derivatives; *Rhodomyrtus tomentosa*.

INTRODUCTION

Cervical cancer is indeed the fourth most common cancer in women globally, causing significant mortality, especially in low-and-middle-income countries, with over 660,000 cases and 350,000 deaths reported in 2022.[1] A persistent infection with certain types of high-risk human papillomavirus (HPV) is the primary cause

* Corresponding author. E-mail: hungnd@tnue.edu.vn
https://doi.org/10.2298/JSC251213016N

of virtually all cervical cancers, though most HPV infections clear up on their own; it's the long-lasting ones, especially HPV 16 and 18, that can lead to abnormal cell changes and eventually cancer if undetected.[2] Current cervical cancer treatments focus on surgery, radiation, chemotherapy, targeted therapy and immunotherapy, often combined based on cancer stage and type, with radiochemotherapy standard for advanced localized disease and chemo plus targeted drugs/immunotherapy for metastatic cases, plus clinical trials exploring new agents like sodomiden.[3] Nonetheless, current treatment methods still face challenges, including a high risk of recurrence, unintended damage to surrounding tissues, and the emergence of drug resistance.[4] Therefore, there is an urgent need to research better options like natural compounds, nanoparticles, and targeted immunotherapies, which aim for higher efficacy with fewer side effects to improve patient outcomes.

In recent years, the application of traditional Chinese medicine (TCM) in cervical cancer treatment has focused on its use as a complementary therapy to standard treatments. Research indicates that TCM helps to improve immune function, reduce the side effects of conventional treatments, and enhance patients' quality of life and survival rates.[5,6] Among these, phloroglucinol, a natural polyphenolic compound found in plants and marine brown algae, is being investigated in laboratory and preclinical studies for its potential anti-cancer effects, including its effects against cervical cancer cells.[7] The anti-cancer mechanism of phloroglucinol is multifaceted, primarily involving the induction of apoptosis and the inhibition of key cancer-related signaling pathways.[8,9] Bcl-2 protein is indeed the original, founding member of the Bcl-2 protein family, a critical anti-apoptotic protein that prevents programmed cell death (apoptosis) by regulating the mitochondria. Its discovery in lymphomas established the concept of defective apoptosis in cancer. It works by inhibiting pro-apoptotic members, preventing the release of cytochrome c, and thereby maintaining cell survival, playing a key role in development but also contributing to cancer when overexpressed.[10,11] Inhibiting anti-apoptotic members of the Bcl-2 family can reinstate normal apoptotic signaling, helping to counteract the resistance that cervical cancer cells often develop against conventional chemotherapy and radiotherapy.

Advancements in computational chemistry and bioinformatics are revolutionizing drug discovery, materials science, and personalized medicine by enabling faster and more accurate molecular modeling, virtual screening, genomic analysis, and the design of novel therapeutics. These fields allow the prediction of molecular properties, identification of disease markers, and optimization of drug formulations, thereby moving research from complex data to clinically relevant solutions.[12] The plant *Rhodomyrtus tomentosa* is widely utilized in traditional Vietnamese culture, where it is known as "sim". Roots and other parts are rich in bioactive compounds, traditionally used across Asia to treat diarrhea, stomach issues, burns, inflam-

mation and even as a hemostatic agent. Scientific studies have explored its antioxidant, anti-inflammatory and antibacterial properties, particularly highlighting compounds like rhodomyrtone for potential drug development.[13] A previous study on this species led to the isolation of several phloroglucinol derivatives with anti-cervical cancer activity against HeLa cell.[14] Despite these advances, the mechanisms of action of their bioactivity, particularly within apoptosis-regulatory pathways, remain underexplored. Therefore, an integrated computational approach was employed to assess both the interaction profiles and the mechanistic feasibility of the selected phloroglucinol derivatives. This study incorporated molecular docking, molecular dynamics simulations, MM/GBSA analyses, ADMET evaluation and DFT-derived electronic parameters. Together, these results support the computational prioritization of candidates for further laboratory testing and structure-guided refinement in a cervical cancer-relevant context.

EXPERIMENTAL

Structural preparation of selected ligands

These selected phloroglucinol derivatives, including tomentodione S (CPD1), rhodomyrtosone I (CPD2), rhodomyrtone (CPD3) and rhodomyrtosone B (CPD4), have molecular formulas of $C_{28}H_{30}O_6$, $C_{28}H_{30}O_6$, $C_{26}H_{34}O_6$ and $C_{26}H_{34}O_6$, with molecular weights of 462.2042, 462.2042, 442.2355 and 442.2355 Da, respectively. Belzutifan, possessing a molecular formula of $C_{17}H_{12}F_3NO_4S$ and a molecular weight of 383.0439 Da, was chosen as a reference compound (Fig. 1).

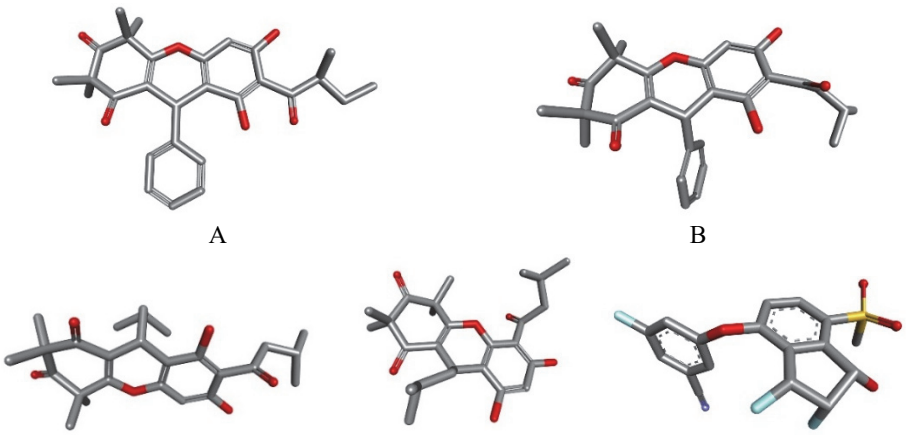

Fig. 1. Structure of the selected ligands: A) CPD1, B) CPD2, C) CPD3, D) CPD4 and E) Belzutifan.

Molecular docking study

Three-dimensional structures of the selected ligands were generated in BIOVIA Discovery Studio Visualizer and exported in PDB format. Before docking, polar hydrogens were incorporated, Gasteiger partial charges were assigned, and all rotatable bonds were left unconstrained

to allow complete conformational freedom. The experimental structure of Bcl-2 (PDB ID: 6GL8) was obtained from the RCSB Protein Data Bank.[15] Docking calculations were carried out using AutoDock Tools,[16] employing a grid box with 60 points along each Cartesian axis and a grid spacing of 0.375 Å. The grid was positioned over the active site of the 6GL8 structure, centered at x = 9.866 Å, y = 0.590 Å and z = 16.717 Å. Conformational exploration was conducted using the Lamarckian genetic algorithm, facilitating the identification of low-energy orientations and favorable interaction patterns. Ten independent GA–LS runs (ga_run = 10) were executed per ligand, with a population size of 150, a maximum of 2,500,000 energy evaluations, and 27,000 generations; Solis–Wets local search was enabled (300 iterations). Clustering of solutions used an RMS tolerance of 2.0 Å. AutoDock searches used stochastic initialization; the random seed handling followed the docking parameter files (seed = pid time). For each compound, the top-scoring pose was further inspected in Discovery Studio Client 2024 and compared to the docked configuration of Belzutifan on the same Bcl-2 template to evaluate correspondence in binding orientation and interaction characteristics.[17]

Molecular dynamics simulation

Molecular dynamics simulations were carried out on the top docking conformation of the ligand bound to the Bcl-2 protein (PDB ID: 6GL8) using GROMACS 2024.4 with the CHARMM36 force field applied under physiological conditions.[18] Before initiating the simulations, the protein structure was corrected in Swiss-PdbViewer, where missing atoms and unresolved residues were rebuilt to ensure structural completeness.[19] Ligand parameters compatible with the selected force field were produced *via* SwissParam.[20] The prepared complex was then positioned in a triclinic water box filled with SPC molecules, and the system's ionic strength was adjusted to 0.15 M NaCl to approximate physiological conditions. An initial energy minimization of 50,000 steps was performed to eliminate steric clashes and stabilize the system. Subsequent equilibration followed a two-stage routine: a 200 ps NVT phase to stabilize temperature, and a 200 ps NPT phase to equilibrate pressure, both maintained at 300 K and 1 bar. Temperature control was applied with the V-rescale thermostat (τ_T = 0.1 ps), using two coupling groups with reference temperatures of 300 K. Pressure coupling during NPT employed the Berendsen barostat (isotropic coupling; τ_p = 2.0 ps, reference pressure = 1.0 bar, compressibility = 4.5×10^{-5} bar^{-1}), while the production phase used the Parrinello–Rahman barostat (isotropic; τ_p = 2.0 ps, reference pressure = 1.0 bar, compressibility = 4.5×10^{-5} bar^{-1}). Production runs were executed as a single 100 ns simulation with a 2 fs time step; trajectory snapshots were recorded at 10 ns intervals for downstream analysis. Initial velocities were generated in the NVT stage from a Maxwell–Boltzmann distribution at 300 K with time-dependent seeding (gen_seed = −1). Electrostatics were treated with PME under the Verlet cutoff scheme (rlist = 1.2 nm; rcoulomb = 1.2 nm), and covalent bonds involving hydrogens were constrained with LINCS (h--bonds). Trajectory processing was performed using Grace to extract structural descriptors, root mean square deviation (*RMSD*), root mean square fluctuation (*RMSF*), radius of gyration (*Rg*), number of hydrogen bonds, and solvent-accessible surface area (*SASA*). Structural alignment in UCSF Chimera 1.13.3 was applied to compare representative conformations sampled along the trajectory and to assess overall complex stability. To investigate interaction durability, the ligand positions at the start (0 ns) and end (100 ns) of the simulation were superimposed within the binding pocket, allowing for the assessment of the persistence of hydrogen bonding, hydrophobic contacts, and van der Waals interactions throughout the 100 ns simulation.[21]

Binding free energy calculation using MMGBSA

A binding free energy calculation for the CPD1–6GL8 and Belzutifan–6GL8 complexes was carried out using the gmx_MMPBSA protocol with the CHARMM36 force field.[22] The MMGBSA evaluation was performed as trajectory post-processing based on the same force-field description used in the molecular dynamics simulations, ensuring parameter consistency across the workflow. The electrostatic component of solvation was estimated through a generalized Born implicit-solvent model, while the nonpolar term was obtained from *SASA* measurements. Energy decomposition was based on snapshots extracted from the molecular dynamics trajectories between 20 and 100 ns, resulting in an 80 ns analysis interval. A total of 125 frames, selected at uniform 80 ps intervals, were used to ensure representative sampling of complex behaviour. This ensemble-averaged approach enabled a direct comparison of the binding energetics of the two ligands, providing insight into differences in affinity and the dynamic stability of each complex over the examined simulation.

ADMET prediction

Evaluation of absorption, distribution, metabolism, excretion and toxicity (ADMET) parameters represents a core element of preclinical screening, as it facilitates early identification of pharmacokinetic constraints and potential safety liabilities. Such an appraisal can mitigate attrition during advanced development stages and enhance the prioritization of candidates exhibiting more favourable therapeutic promise. In this study, the pkCSM framework was applied to estimate the ADMET profiles of CPD1 and Belzutifan computationally. The pkCSM approach derives predictions from graph-based molecular signatures, thereby enabling a systematic assessment of key biopharmaceutical and toxicological properties of the investigated compounds.[23]

Quantum DFT analysis

Structural minimization of CPD1 and belzutifan was conducted using the ORCA quantum chemistry suite (ver. 6.1.0). Initial geometries were prepared using Avogadro, while molecular orbital visualisation and related electronic analyses were completed with IboView (v20211019).[24-26] Density functional theory computations employed the B3LYP exchange–correlation functional together with the 6-31G(d,p) basis set to yield internally consistent electronic wavefunctions. Based on the converged, fully optimized geometries, quantum-chemical descriptors were derived, comprising the highest occupied molecular orbital (HOMO) and lowest unoccupied molecular orbital (LUMO) energies, the HOMO–LUMO separation (ΔE), chemical potential (μ), electronegativity (χ), global hardness (η), softness (σ) and electrophilicity index (ω). Interpretation of these quantities followed the Koopmans' theorem approximation to characterise electronic structure and to support inference regarding the intrinsic reactivity of the studied molecules.[27,28]

RESULTS AND DISCUSSION

Molecular docking analysis

Molecular docking constitutes a computational strategy for modelling the association between a low-molecular-weight ligand and a macromolecular target, such as a protein, to estimate the preferred binding orientation and the corresponding interaction strength. This approach supports a mechanistic interpretation of molecular recognition and is widely applied in structure-based drug discovery to relate binding propensity to biological response. Docking protocols typically integrate conformational and positional sampling algorithms to explore candidate binding

modes, followed by scoring functions that approximate the energetic favourability of each configuration. The highest-ranked solutions represent putative stable complexes with comparatively low estimated free energy and enhanced structural complementarity.[29] Before docking the selected ligands into the Bcl-2 structure (PDB ID: 6GL8), the reliability of the docking workflow was examined through a re-docking exercise using the ligand co-resolved in the crystallographic complex (Fig. 2). The optimal re-docked pose reproduced the experimentally reported binding orientation within the predefined binding region with an *RMSD* of 0.7540 Å, indicating that the grid definition and search settings were appropriate for describing the 6GL8 pocket. In standard docking practice, successful recovery of the co-crystallized pose with a *RMSD* below 2 Å is generally interpreted as evidence of acceptable protocol performance and pose predictability.[30] Following this validation step, all ligand poses were scored and ranked according to predicted binding energy, where more negative values reflect a stronger estimated binding preference.

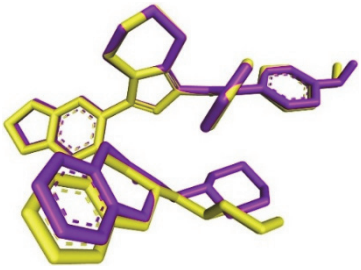

Fig. 2. The superimposition of the docked and native ligands within 6GL8 protein for validation of the molecular docking protocol (yellow = native, violet = docked).

As reported in Table I, docking scores and residue-level contacts were examined for four candidate ligands (CPD1–CPD4) within a pocket repeatedly defined by Phe104, Tyr108, Asp111, Phe112, Gln118, Leu137, Ala149 and Phe153. Belzutifan was included as the reference compound under the same scoring scheme. Across the evaluated complexes, the contact pattern indicated an aromatic–aliphatic cavity dominated by Phe/Tyr side chains, complemented by polar residues (Asp111, Gln118 and Glu136) that may contribute to directional stabilization through hydrogen bonding. Predicted binding energies ranged from –37.36 to –25.73 kJ/mol, supporting a clear affinity ranking of CPD1 > CPD2 > CPD3 > CPD4 > Belzutifan. The interaction inventory comprised hydrogen bonding, van der Waals contacts, and hydrophobic interactions, as annotated for each ligand––target complex. Collectively, these non-covalent forces are expected to promote complex integrity through: *i*) directional hydrogen-bond constraints that stabilize specific geometries *via* alignment with electronegative centers, *ii*) hydrophobic clustering that limits solvent accessibility and favors compact packing within the binding cavity and *iii*) short-range van der Waals complementarity that contributes incremental stabilization while fine-tuning association energetics and kinetic persistence.[31,32]

TABLE I. The interactions between the docked ligands and the protein 6GL8

Docked ligand	Binding energy, kJ/mol	Hydrogen bond interaction	Van der Waals interaction	Hydrophobic interaction
CPD1	–37.36	–	Phe104, Tyr108, Asp111, Glu114, Gln118, Leu137, Ala149, Phe153	Phe112, Met115, Leu119, Val133
CPD2	–33.14	Glu136	Phe104, Tyr108, Glu114, Gln118, Leu137, Ala149	Asp111, Phe112, Met115, Leu119, Val133
CPD3	–32.38	Gln118, Glu136	Phe104, Phe112, Leu119, Arg129, Thr132, Ala149, Phe153	Met115, Val133, Leu137
CPD4	–30.42	–	Phe104, Tyr108, Asp111, Gln118, Leu119, Val133, Leu137, Glu152, Val156	Phe112, Met115, Ala149, Phe153
Belzutifan	–25.73	–	Tyr108, Val133, Glu136, Leu137, Ala149, Glu152, Phe153	Phe104, Asp111, Phe112, Met115, Gln118, Leu119

CPD1 produced the most favorable docking energy (–37.36 kJ/mol) and engaged the complete canonical residue set (Phe104, Tyr108, Asp111, Phe112, Gln118, Leu137, Ala149, Phe153). No hydrogen bond was annotated; instead, stabilization was characterized by extensive van der Waals complementarity (Phe104, Tyr108, Asp111, Glu114, Gln118, Leu137, Ala149, Phe153) together with hydrophobic contacts involving Phe112, Met115, Leu119 and Val133, consistent with tight packing inside the pocket (Fig. 3A).

CPD2 displayed the second-highest affinity (–33.14 kJ/mol) while retaining most core contacts (Phe104, Tyr108, Asp111, Phe112, Gln118, Leu137, Ala149). A hydrogen bond to Glu136 was recorded, accompanied by van der Waals interactions with Phe104, Tyr108, Glu114, Gln118, Leu137 and Ala149 and additional hydrophobic contributions from Asp111, Phe112, Met115, Leu119 and Val133. The absence of Phe153 among the listed active-site contacts suggests a slightly reduced engagement of the distal aromatic boundary relative to CPD1.

CPD3 yielded an intermediate docking score (–32.38 kJ/mol) and contacted Phe104, Phe112, Gln118, Leu137, Ala149 and Phe153. Two hydrogen bonds were assigned (Gln118 and Glu136), and the van der Waals network extended toward Leu119, Arg129 and Thr132 in addition to Phe104, Phe112, Ala149 and Phe153, indicating a pose with measurable polar anchoring yet a shifted contact distribution. Hydrophobic interactions were primarily associated with Met115, Val133 and Leu137.

CPD4 exhibited a lower predicted affinity (–30.42 kJ/mol) despite preservation of the canonical active-site residues (Phe104, Tyr108, Asp111, Phe112, Gln118, Leu137, Ala149, Phe153). No hydrogen bond was annotated. Van der

Waals contacts included the core residues and additional interactions with Leu119, Val133, Glu152 and Val156. At the same time, hydrophobic contributions involved Phe112, Met115, Ala149 and Phe153, suggesting that nonpolar and dispersive terms dominated binding stabilization without explicit polar locking.

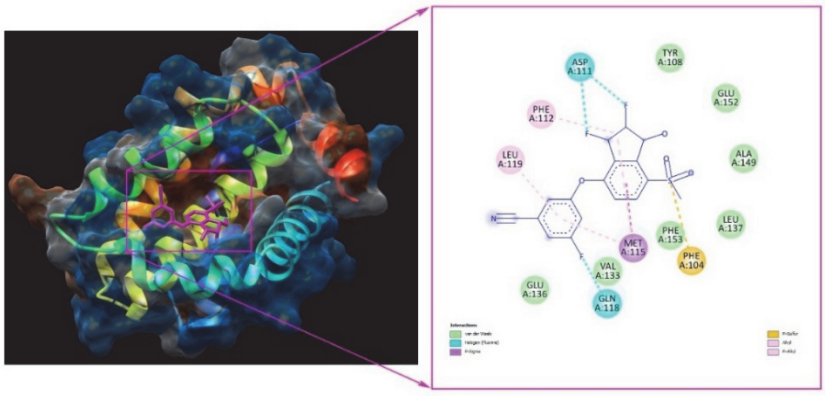

A

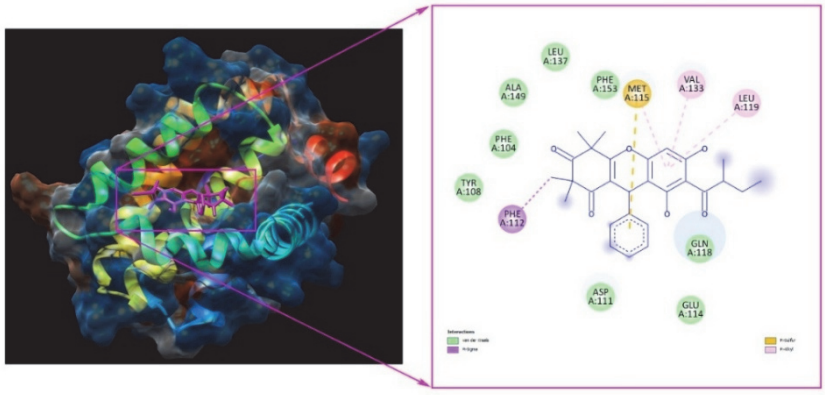

B

Fig. 3. Molecular docking model and 2D interaction diagram of CPD1 (A) and Belzutifan (B) with 6GL8 protein.

Belzutifan showed the weakest docking energy (–25.73 kJ/mol) while maintaining contact with the conserved pocket residues (Phe104, Tyr108, Asp111, Phe112, Gln118, Leu137, Ala149, Phe153). The interaction map lacked hydrogen bonding and was defined by van der Waals contacts (Tyr108, Val133, Glu136, Leu137, Ala149, Glu152, Phe153) plus hydrophobic interactions (Phe104, Asp111, Phe112, Met115, Gln118, Leu119) (Fig. 3B).

Overall, CPD1 emerged as the highest-priority ligand in the docking series, exhibiting the most favorable binding energy (–37.36 kJ/mol) and extensive engagement of the conserved binding pocket (Phe104, Tyr108, Asp111, Phe112, Gln118, Leu137, Ala149 and Phe153). The predicted pose was stabilized predominantly by dense van der Waals complementarity with the core residues and additional hydrophobic packing involving Phe112, Met115, Leu119 and Val133, indicating tight accommodation within the aromatic–aliphatic cavity. On this basis, CPD1 was selected as the highest-priority candidate for subsequent molecular dynamics simulations to evaluate the time-dependent persistence of its pose and the stability of its principal contact network under protein flexibility and solvent effects.

Molecular dynamics simulation

Drug-likeness screening, molecular docking, and molecular dynamics simulations form a complementary in silico pipeline for structure-based drug discovery. Drug-like filters narrow chemical space, docking rapidly proposes and ranks binding poses, and molecular dynamics provides time-resolved trajectories that capture conformational fluctuations and intermolecular interactions by integrating classical equations of motion on a potential-energy surface. In this context, molecular dynamics extends docking by testing pose stability in a dynamic, solvated environment, evaluating persistence of key contact and hydrogen-bond networks and supporting more reliable energetic characterization for hit validation and lead optimization.[33] Therefore, the evaluation systematically investigated *RMSD*, *RMSF*, *Rg*, *Hbonds* and *SASA* metrics to determine the stability, flexibility and solvent exposure of the CPD1-6GL8 and Belzutifan-6GL8 complexes throughout the simulation. Because one 100 ns production trajectory was analyzed for each complex, these MD metrics should be interpreted as qualitative descriptors of trajectory behavior rather than statistically averaged results from replicate simulations. Consequently, the total energy and potential energy values for the CPD1-6GL8 complex were found to be –227.913 and –282.916 kJ/mol, respectively. For the Belzutifan––6GL8 complex, the total energy and potential energy values were measured at –227.574 and –282.502 kJ/mol, respectively. The simulation system maintained equilibrium at a temperature of 300 K.

The *RMSD* describes the extent of structural displacement relative to a reference after optimal superposition and is routinely used to monitor equilibration and global stability during molecular dynamics simulations.[34] In the present trajectories, both complexes exhibited an early accommodation phase followed by confinement within a narrow *RMSD* band, without sustained divergence across the 0–100 ns interval. The CPD1–6GL8 profile fluctuated predominantly around the 0.18–0.24 nm region, with intermittent excursions approaching 0.25 nm, whereas the Belzutifan–6GL8 profile occupied a similar interval but displayed more frequent high--*RMSD* episodes (reaching 0.25–0.26 nm), particularly in the late-stage segment

(Fig. 4A). The close overlap of both traces and the absence of progressive drift support preservation of the overall protein conformation under both ligand-bound conditions. To quantify late-stage equilibration, plateau *RMSD* values were defined as the time-averaged *RMSD* over the final 30 ns of the trajectories (70–100 ns). The plateau *RMSD* was 0.204±0.014 nm for CPD1–6GL8 and 0.217±0.013 nm for Belzutifan–6GL8, where the standard deviation reflects fluctuations within this plateau window of a single trajectory.

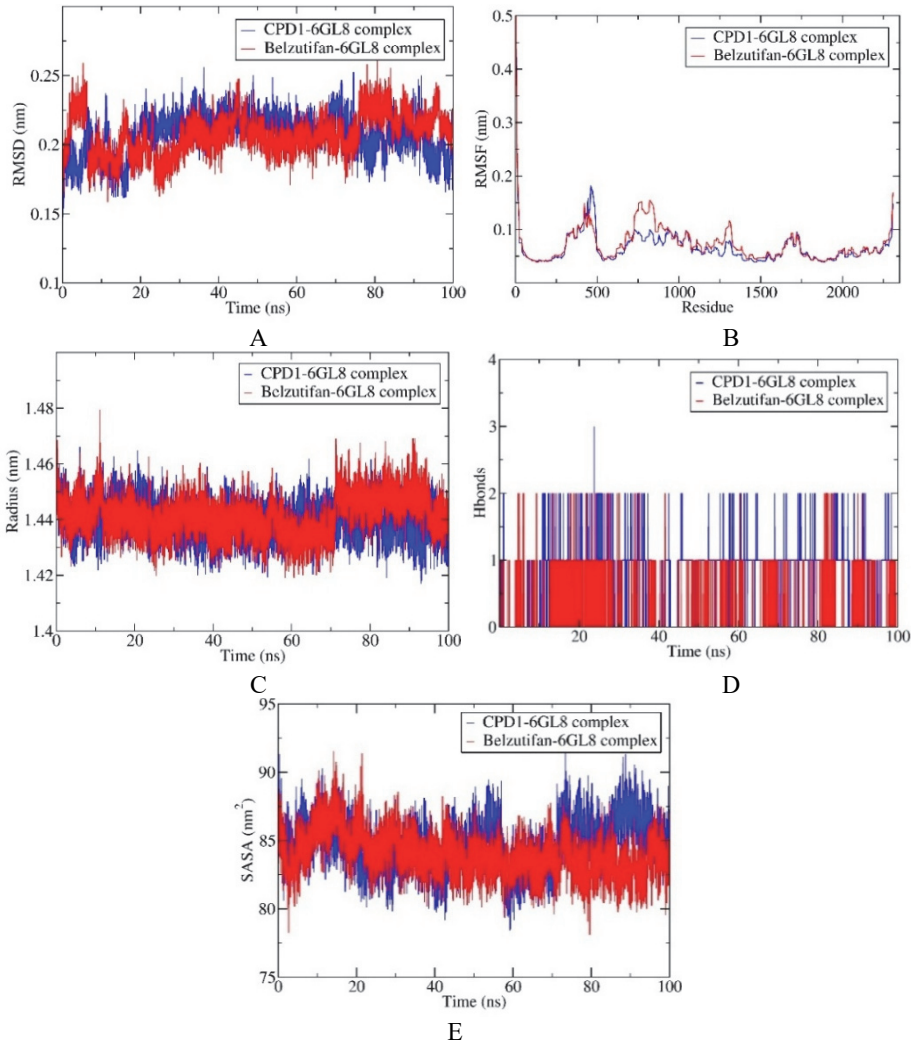

Fig. 4. Results of MD simulation for the bindings of CPD1 (blue) and Belzutifan (red) with 6GL8 protein. A) *RMSD*, B) *RMSF*, C) *Rg*, D) *Hbonds* and E) *SASA*.

The *RMSF* quantifies residue-level mobility around the time-averaged position, thereby identifying locally flexible segments and relatively rigid cores. Within the Gly7–Gly203 interval, the *RMSF* profiles of both the CPD1–6GL8 and Belzutifan–6GL8 complexes are low in amplitude and nearly superimposable, indicating a structurally stable N-terminal region beyond the highly mobile initial residues. After the sharp fluctuation at the beginning of the sequence, *RMSF* values rapidly decrease and remain consistently low throughout this interval, generally around 0.04–0.06 nm, and rarely exceed 0.07–0.08 nm (Fig. 4B). No pronounced flexibility peaks or ligand-dependent deviations are observed in this region, suggesting that ligand binding has minimal impact on local dynamics within Gly7–Gly203, which behaves as a relatively rigid structural core in both simulations.

Rg reflects the mass-weighted spatial distribution of atoms around the center of mass and serves as a measure of global compactness. Both systems demonstrated an early relaxation from the 1.46 nm region toward 1.44 nm, followed by sustained oscillations within a constrained interval. The CPD1–6GL8 trajectory remained approximately within 1.42–1.46 nm, while Belzutifan–6GL8 generally occupied 1.42–1.47 nm and included a rare transient expansion close to 1.48 nm (Fig. 4C). A mild upward shift for Belzutifan–6GL8 during 70–95 ns was evident relative to CPD1–6GL8, consistent with slightly reduced compactness in the reference-bound state during that period.

Intermolecular hydrogen bonds provide directional constraints that can enhance binding specificity and contribute to dynamic stability, although hydrophobic and dispersive interactions frequently supply substantial stabilization in ligand–protein complexes.[35] The CPD1–6GL8 complex exhibited hydrogen-bond counts spanning 0–3, with the trajectory most commonly occupying 0–2 bonds and a short-lived event reaching three near the early-mid portion of the simulation (Fig. 4D). Belzutifan–6GL8 fluctuated mainly between 0 and 2 hydrogen bonds, with extended intervals dominated by a single bond and intermittent two-bond events. The comparative pattern indicates that CPD1 maintained a slightly broader polar-contact repertoire, while a more consistently sparse hydrogen-bond regime characterized Belzutifan.

The *SASA* reports the degree of solvent exposure and can reflect changes in global packing and surface rearrangements during molecular dynamics. Both systems displayed bounded *SASA* fluctuations across the entire trajectory (80–92 nm^2), without a monotonic drift suggestive of unfolding (Fig. 4E). A modest separation emerged after 70 ns, where CPD1–6GL8 tended toward higher *SASA* values and larger excursions, while Belzutifan–6GL8 showed a comparatively lower envelope over the same interval, indicating subtle differences in solvent exposure despite broadly stable global architecture.

Collectively, *RMSD* and *Rg* traces support sustained structural integrity for both ligand-bound states across 100 ns, with CPD1–6GL8 exhibiting slightly tighter

late-stage confinement in global measures and a marginally richer hydrogen--bonding pattern. The *RMSF* distribution indicates that ligand-dependent effects were localized rather than systemic, consistent with stable binding accompanied by limited loop reorganization. When considered alongside the stronger docking score previously obtained for CPD1, the MD readouts provide convergent support for prioritization of CPD1 as the more favorable 6GL8 binder under the simulated conditions.

Free binding energy (MMGBSA) analysis

Molecular mechanics/generalized Born surface area (MM/GBSA) is a commonly applied approach in computational biochemistry and drug design for approximating the binding free energy of a ligand–macromolecule complex. The method integrates molecular mechanics energy terms with an implicit-solvent treatment, where the generalized Born model represents electrostatic solvation and a solvent-accessible surface area term accounts for nonpolar contributions. By post-processing molecular dynamics trajectories rather than relying on fully explicit solvent-free energy protocols, MMGBSA provides a comparatively efficient route to ranking binding affinities while retaining physically interpretable energy components.

Binding free energies for the CPD1–6GL8 and Belzutifan–6GL8 complexes were assessed using the MM/GBSA approach. In this analysis, the reported binding term represents an enthalpy-dominated estimate because configurational entropy was not included; nevertheless, such treatment remains appropriate for comparative ranking between closely related protein–ligand systems. The mean values and corresponding standard deviations describe the interplay between gas-phase stabilization, arising from van der Waals and electrostatic interactions, and the opposing (or compensating) influence of solvation, captured by polar and nonpolar solvent contributions, thereby enabling mechanistic interpretation through energy-component decomposition. Both systems display a favourable association, as indicated by negative total binding energies. Configurational entropy change ($-T\Delta S$) was intentionally not included in the present MM/GBSA post-processing; therefore, the reported ΔTOTAL values should be interpreted as enthalpy change-dominated (ΔH-like) estimates rather than full binding free energy changes (ΔG). As detailed in Table II, CPD1–6GL8 shows a markedly more favorable mean ΔTOTAL of –138.78±15.4 kJ/mol relative to Belzutifan–6GL8 (–63.72±14.31 kJ/mol), corresponding to an advantage of 75.06 kJ/mol for CPD1. This separation is primarily attributed to stronger gas-phase interactions for CPD1, with ΔGGAS reaching –258.49±38.79 kJ/mol, compared with –183.47±41.59 kJ/mol for Belzutifan. Within the gas-phase term, electrostatics contribute substantially to the difference: ΔEEL is more stabilizing for CPD1 (–101.92±39.83 kJ/mol) than for Belzutifan

(–52.01±35.77 kJ/mol). Van der Waals interactions remain favourable for both ligands and further support CPD1 binding (ΔVDWAΔALS = –156.57±14.85 kJ/mol *versus* –131.46±16.44 kJ/mol). In contrast, the overall solvation contribution is identical in mean magnitude for both complexes (ΔGSOLV = 119.75±27.91 kJ/mol for CPD1 and 119.75±34.18 kJ/mol for Belzutifan). This equality reflects rounding at the reported precision, because ΔGSOLV is obtained as ΔEGB + ΔESURF and the component means differ slightly between systems but yield the same rounded sum. Consistently, the polar solvation term is comparable (ΔEGB = 141.88±28.53 kJ/mol for CPD1; 138.91±35.10 kJ/mol for Belzutifan), whereas the nonpolar component is slightly more favorable for CPD1 (ΔESURF = –22.13±1.84 kJ/mol) than for Belzutifan (–19.16±2.3 kJ/mol). Variability in the total binding estimate remains similar between systems, with standard deviations of 15.40 and 14.31 kJ/mol for CPD1 and Belzutifan, respectively, indicating a consistent energetic preference for CPD1, primarily driven by stronger gas-phase stabilization, particularly electrostatic complementarity.

TABLE II. Changes in free energy of binding obtained using MM/GBSA calculations

Energy component	Average, kJ/mol		Standard deviation	
	CPD1–6GL8	Belzutifan–6GL8	CPD1–6GL8	Belzutifan–6GL8
ΔVDWAΔALS	–156.57	–131.46	14.85	16.44
ΔEEL	–101.92	–52.01	39.83	35.77
ΔEGB	141.88	138.91	28.53	35.10
ΔESURF	–22.13	–19.16	1.84	2.30
ΔGGAS	–258.49	–183.47	38.79	41.59
ΔGSOLV	119.75	119.75	27.91	34.18
ΔTOTAL	–138.78	–63.72	15.40	14.31

ADMET prediction analysis

In silico ADMET profiling was conducted to characterize the predicted pharmacokinetic behavior and safety-relevant alerts of CPD1 in comparison with the reference compound Belzutifan, with descriptors organized into absorption, distribution, metabolism, excretion and toxicity domains. This side-by-side evaluation provides an integrated basis for identifying potential liabilities and prioritizing candidates within an *in silico* modeling framework focused on selected phloroglucinol derivatives from *R. tomentosa* and their prospective utility against cervical cancer.[36] The predicted ADMET parameters for CPD1 and Belzutifan are summarized in Table III.

Regarding absorption, both molecules exhibit closely matched predicted aqueous solubility, with water solubility (mol/L) log values of –4.749 for CPD1 and –4.733 for Belzutifan, indicating comparably limited dissolution under the applied model. Membrane permeability, however, differentiates the profiles: Belzutifan presents higher Caco-2 permeability (log (*Papp*/10^{-6} cm s^{-1}) = 1.282) than CPD1

(1.109), whereas CPD1 shows stronger predicted human intestinal absorption (98.254 %) relative to Belzutifan (92.996 %). Skin permeability estimates remain similar, with log *Kp* values of –2.736 for CPD1 and –2.784 for Belzutifan. Transporter-related annotations further distinguish the compounds, as CPD1 is predicted to be a P-glycoprotein substrate, whereas Belzutifan is not. Both compounds are flagged as P-glycoprotein I inhibitors; however, only CPD1 is expected to inhibit P-glycoprotein II.

TABLE III. Predicted ADMET properties of CPD1 and Belzutifan

ADMET property	CPD1	Belzutifan
Log (Water solubility in mol/L)	–4.749	–4.733
Caco2 permeability log (*Papp*/10^{-6} cm s^{-1})	1.109	1.282
Intestinal absorption (Human), %	98.254	92.996
Skin permeability (log *Kp*)	–2.736	–2.784
P-glycoprotein substrate	Yes	No
P-glycoprotein I inhibitor	Yes	Yes
P-glycoprotein II inhibitor	Yes	No
Log (*VDss* in L/kg)	–0.152	0.684
Fraction unbound (human), *Fu*	0.035	0.014
BBB permeability (log *BB*)	0.192	–1.105
CNS permeability (log *PS*)	–2.605	–3.167
CYP2D6 substrate	No	No
CYP3A4 substrate	Yes	Yes
CYP1A2 inhibitor	No	Yes
CYP2C19 inhibitor	Yes	Yes
CYP2C9 inhibitor	Yes	Yes
CYP2D6 inhibitor	No	No
CYP3A4 inhibitor	No	No
Log (Total clearance in mL/(min kg))	0.212	0.291
Renal OCT2 substrate	No	No
AMES toxicity	No	No
Log (Max. tolerated dose (human) in mg/(kg day))	–0.049	0.291
hERG I inhibitor	No	No
hERG II inhibitor	Yes	No
Oral rat acute toxicity (*LD50*), mol/kg	2.543	2.775
Log (Oral rat chronic toxicity (*LOAEL*), mg/(kg_bw day))	1.618	0.892
Hepatotoxicity	No	Yes
Skin sensation	No	No
Log (Tetrahymena pyriformis toxicity in μg/L)	0.292	0.419
Log (Minnow toxicity in mM)	–0.89	1.344

Distribution descriptors indicate divergent systemic disposition tendencies. A lower predicted steady-state volume of distribution is observed for CPD1 (log *VDss*/L kg^{-1}) = –0.152) compared with Belzutifan (0.684), consistent with a more constrained distributional extent for CPD1 within this output. The predicted

unbound fraction in human plasma is higher for CPD1 (*Fu* = 0.035) than for Belzutifan (0.014), suggesting greater free-drug availability for CPD1 according to the model. Central exposure indices also differ: BBB permeability is positive for CPD1 (log *BB* = 0.192) but strongly negative for Belzutifan (–1.105), and CNS permeability follows the same directionality, with CPD1 showing less negative log *PS* (–2.605) than Belzutifan (–3.167), indicating comparatively higher predicted central penetration for CPD1. Because BBB penetration is not a therapeutic requirement for cervical cancer, the positive BBB permeability prediction for CPD1 is discussed primarily as a distribution/safety consideration rather than a clinical advantage.

Metabolism-related predictions highlight shared and distinct CYP interaction patterns. Neither compound is categorized as a CYP2D6 substrate, while both are predicted CYP3A4 substrates. Inhibitory flags overlap for CYP2C19 and CYP2C9, which are positive for both CPD1 and Belzutifan. A key divergence is seen for CYP1A2 inhibition, which is negative for CPD1 but positive for Belzutifan. No inhibition is predicted for CYP2D6 or CYP3A4 in either compound under the same settings.

Excretion estimates indicate a modestly higher predicted total clearance for Belzutifan (0.291) compared to CPD1 (0.212). Renal OCT2 substrate status is negative for both ligands, indicating no OCT2-associated renal transport designation in the present output.

Toxicity endpoints reveal both shared reassurance signals and notable compound-specific alerts. AMES toxicity and hERG I inhibition are negative for both CPD1 and Belzutifan. In contrast, hERG II inhibition is predicted for CPD1 but not for Belzutifan, indicating a differential cardiac liability flag in this dataset. The predicted hERG II inhibition flag for CPD1 is an in silico alert (pkCSM-based) and should not be interpreted as confirmed cardiotoxicity; experimental electrophysiology assays would be required to validate this risk. Hepatotoxicity is expected to be negative for CPD1 and positive for Belzutifan, representing a prominent separation in safety-relevant alerts. Quantitative indices further differentiate tolerability and toxicity: the log of maximum tolerated dose (human) is –0.049 for CPD1 and 0.291 for Belzutifan; oral rat acute toxicity (*LD50*) is 2.543 mol/kg for CPD1 and 2.775 mol/kg for Belzutifan; log of oral rat chronic toxicity (*LOAEL*) is higher for CPD1 (1.618) than for Belzutifan (0.892). Skin sensitization is negative for both. Ecotoxicity-associated descriptors indicate higher log of predicted *Tetrahymena pyriformis* toxicity for Belzutifan (0.419) than CPD1 (0.292), while log of minnow toxicity differs markedly, with CPD1 at –0.89 and Belzutifan at 1.344.

Overall, the ADMET output indicates broadly similar solubility and dermal permeability for CPD1 and Belzutifan, while suggesting higher intestinal absorption for CPD1, despite its lower Caco-2 permeability. Distributional behavior differs substantially, with CPD1 exhibiting lower *VDss* yet higher predicted unbound

fraction and less restricted BBB/CNS permeability compared with Belzutifan. Metabolic interaction potential overlaps through CYP3A4 substrate status and CYP2C19/CYP2C9 inhibition, whereas a CYP1A2 inhibition flag is restricted to Belzutifan. Safety-related predictions indicate an absence of hepatotoxicity for CPD1, alongside a hepatotoxicity alert for Belzutifan. A hERG II inhibition flag emerges for CPD1, but not for Belzutifan. These distinctions provide a mechanistic basis for prioritization and risk awareness in subsequent computational and experimental validation of phloroglucinol-derived candidates targeting cervical cancer--relevant pathways.

Quantum chemistry computation using the DFT method

DFT is indeed crucial for natural compounds and drug design, as it helps predict molecular structures, properties, binding affinities to targets, reaction pathways and simulate interactions. This speeds up the discovery of new medicines from nature by understanding how molecules work and fit together, optimizing lead compounds and reducing experimental costs.[37] DFT calculations were thus performed, following the classical modeling workflow, to characterize the electronic structure and infer reactivity-associated features of CPD1 relative to the reference compound, Belzutifan. The computed set included *EHOMO* (eV), *ELUMO* (eV), ΔE (eV), μ (eV), χ (eV), η (eV), σ (eV^{-1}) and ω (eV), collectively describing frontier-orbital energetics, resistance to charge redistribution and electrophilic behavior, Table IV. Within this context, *EHOMO* relates to electron-donating propensity, whereas *ELUMO* reflects electron-accepting capacity; the ΔE between these orbitals serves as an indicator of electronic stability *versus* chemical responsiveness.[38]

TABLE IV. DFT calculations for CPD1 and Belzutifan; *EHOMO*: energy of highest occupied molecular orbitals; *ELUMO*: energy of lowest unoccupied molecular orbitals; ΔE: energy gap; μ: chemical potential; χ: electronegativity; η: hardness; σ: softness; ω: electrophilicity index

Molecule	*EHOMO* / eV	*ELUMO* / eV	ΔE / eV	μ / eV	χ / eV	η / eV	σ / eV^{-1}	ω / eV
CPD1	–7.7313	–4.7815	2.9498	–6.2564	6.2564	1.4749	0.6780	13.2696
Belzutifan	–9.9400	1.3289	11.2689	–4.3056	4.3056	5.6345	0.1775	1.6450

For CPD1, *EHOMO* is –7.7313 eV, higher than the value obtained for Belzutifan (–9.9400 eV), supporting a comparatively greater tendency toward electron donation under the applied computational conditions (Table IV). A pronounced divergence is observed for *ELUMO*, where CPD1 retains a negative value (–4.7815 eV) while Belzutifan exhibits a positive *ELUMO* of 1.3289 eV, consistent with a substantially lower-lying acceptor orbital for CPD1. In accordance with these frontier-orbital positions, CPD1 presents a markedly smaller ΔE of 2.9498 eV relative to Belzutifan (11.2689 eV). This pattern aligns with enhanced electronic polarizability and higher potential chemical responsiveness for CPD1, whereas the

wider gap in Belzutifan is consistent with greater stabilization of frontier orbitals. Global descriptors further reinforce these differences. Electronegativity χ is higher for CPD1 (6.2564 eV) than for Belzutifan (4.3056 eV), accompanied by a more negative chemical potential μ for CPD1 (–6.2564 eV) compared with Belzutifan (–4.3056 eV), reflecting the expected inverse correspondence between μ and χ within this descriptor set. Hardness η is substantially lower for CPD1 (1.4749 eV) than for Belzutifan (5.6345 eV). The reciprocal softness σ is consequently higher for CPD1 (0.6780 eV^{-1}) than for Belzutifan (0.1775 eV^{-1}), indicating reduced resistance to electron-density deformation for CPD1 (Fig. 5). Finally, the electrophilicity index ω is markedly elevated for CPD1 (13.2696 eV) relative to Belzutifan (1.6450 eV), indicating a stronger electrophilic character for CPD1 in the present DFT dataset.

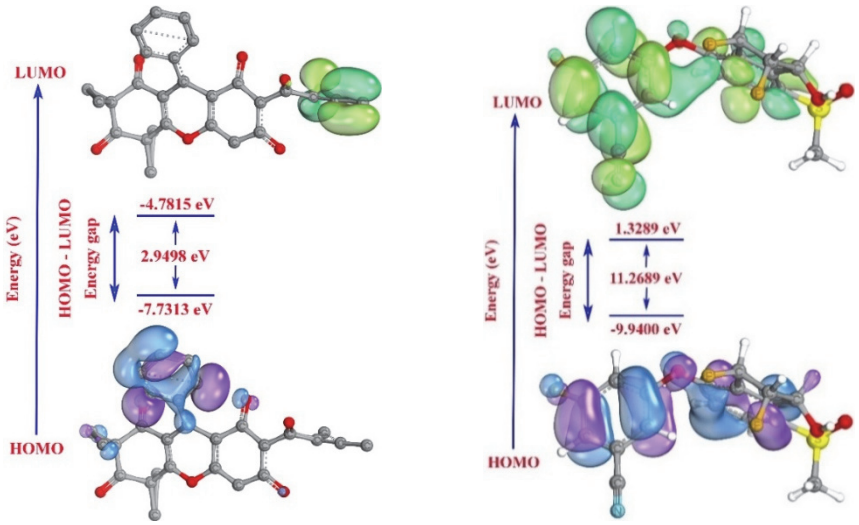

Fig. 5. HOMO and LUMO surface diagrams of: CPD1 (A) and Belzutifan (B).

Frontier-orbital and global reactivity indices primarily reflect intrinsic electronic responsiveness and should not be interpreted as stand-alone predictors of anticancer activity. Here, the smaller ΔE and higher ω of CPD1 are viewed as facilitating polarization and charge redistribution upon complexation, which aligns with the more favorable gas-phase contribution, especially ΔEEL, observed in the MM/GBSA decomposition. This electronic context complements the docking/MD observation that CPD1 is stabilized largely by dispersive and hydrophobic packing within the 6GL8 cavity, while experimental validation remains necessary to link electronic descriptors to biological response. A formal correlation analysis between DFT descriptors and binding energies was not performed in the present dataset; accordingly,

any linkage between electronic indices and binding behavior is discussed as a qualitative rationale rather than a demonstrated relationship.

CONCLUSION

This work integrated molecular docking, molecular dynamics, MM/GBSA, ADMET prediction, and DFT descriptors to evaluate phloroglucinol derivatives from *R. tomentosa* against the 6GL8 target in a cervical cancer-relevant context. CPD1 consistently ranked highest, showing the best docking score (–37.36 kJ/mol) *versus* Belzutifan (–25.73 kJ/mol) with extensive engagement of the conserved pocket, and stable MD behavior over 100 ns. MM/GBSA supported stronger binding for CPD1 (ΔTOTAL = –138.78±15.4 kJ/mol) than Belzutifan (–63.72±14.31 kJ/mol), driven by more favorable gas-phase interactions (ΔGGAS = –258.49±38.79 *vs.* –183.47±41.59 kJ/mol) while ΔGSOLV remained equal (119.75 kJ/mol). ADMET outputs indicated similar solubility but higher intestinal absorption for CPD1, alongside distinct safety/transport alerts (hepatotoxicity negative yet hERG II positive for CPD1; hepatotoxicity positive yet hERG II negative for Belzutifan). DFT further characterized CPD1 by a smaller ΔE (2.9498 *vs.* 11.2689 eV) and higher ω (13.2696 *vs.* 1.6450 eV), supporting greater electrophilic character, which is interpreted as an electronic-property context for binding energetics rather than a direct surrogate for biological potency, and is presented as supportive electronic context in the absence of correlation analysis.

Despite the utility of computational screening for triaging candidates, experimental confirmation remains essential to establish the translational robustness of findings. A further limitation of this study is that Belzutifan, although used here as a reference compound under the same computational protocol, is not a canonical Bcl-2 inhibitor. Therefore, comparisons against Belzutifan should be interpreted cautiously and not as equivalent to benchmarking against a target-validated Bcl-2 inhibitor. No *in vitro* or *in vivo* validation is available within the present dataset, limiting inference beyond the predicted binding and property space. Future work should prioritize biochemical target-engagement assays, cell-based efficacy testing in cervical cancer models, and safety-oriented profiling that addresses electrophysiology-relevant endpoints, hepatic liability and absorption, distribution, metabolism and excretion (ADME) behavior. Additional limitations include the absence of an explicit entropic term in MM/GBSA and the lack of dedicated evaluation of off-target or unintended covalent mechanisms. If subsequent experimental studies corroborate potency and an acceptable safety margin, progression toward more advanced preclinical characterization would be justified, with the current computational results providing a mechanistic foundation to guide rational follow-up and lead optimization.

ИЗВОД

IN SILICO МОДЕЛОВАЊЕ ОДАБРАНИХ ФЛОРОГЛУЦИНОЛСКИХ ДЕРИВАТА ИЗ Rhodomyrtus tomentosa: МЕХАНИСТИЧКИ УВИД У ЊИХОВ ПОТЕНЦИЈАЛ ПРОТИВ КАРЦИНОМА ГРЛИЋА МАТЕРИЦЕ

HUNG DUC NGUYEN

Thai Nguyen University of Education, 24000 Thai Nguyen, Vietnam

Карцином грлића материце остаје један од водећих узрока оболевања и смртности на глобалном нивоу, а примарни покретач је перзистентна инфекција високо-ризичним типовима HPV. Природни флороглуцинолски деривати из *Rhodomyrtus tomentosa* показали су потенцијал против карцинома грлића материце, али њихови механизми повезани са апоптозом и даље су недовољно разјашњени. У овом раду, одабрани флороглуцинолски деривати процењени су као потенцијални инхибитори анти-апоптотског протеина Bcl-2 (PDB: 6GL8) применом интегрисаног *in silico* приступа који обухвата молекулски докинг, 100 ns молекулску динамику, MM/GBSA процену слободне енергије везивања, ADMET профилисање и DFT анализу електронских својстава. Докинг резултати су издвојили CPD1 као најповољнији лиганд (−37,36 kJ/mol), бољи од белзутифана (−25,73 kJ/mol), уз стабилно уклапање у конзервирани везујући џеп. Трајекторије MD симулација подржале су стабилно формирање комплекса током 100 ns. MM/GBSA анализа додатно је указала на јаче везивање CPD1 (ΔTOTAL = −138,78±15,4 kJ/mol) у односу на белзутифан (−63,72±14,31 kJ/mol), пре свега услед повољнијих интеракција у гасној фази, уз задржавање упоредивог солватационог доприноса. ADMET предвиђања указала су на сличну растворљивост, али и већу интестиналну апсорпцију CPD1, као и присуство hERG II сигнала који захтева даљу оптимизацију у контексту кардиотоксичности. Добијени DFT дескриптори су у складу са појачаним електрофилним карактером CPD1. У целини, CPD1 је рачунарски идентификован као приоритетни скелет за даљу експерименталну валидацију и структурално вођену оптимизацију.

(Примљено 13. децембра 2025, ревидирано 26. фебруара, прихваћено 23. марта 2026)

REFERENCES

1. F. Bray, M. Laversanne, H. Sung, J. Ferlay, R. L. Siegel, I. Soerjomataram, A. Jemal, *CA Cancer J. Clin.* **74** (2024) 229 (https://doi.org/10.3322/caac.21834)
2. K. S. Okunade, *J. Obstet. Gynaecol.* **40** (2020) 602 (https://doi.org/10.1080/01443615.2019.1634030)
3. M. Bida, B. Mosoane, B. Phakathi, M. Sebitloane, M. Z. Muallem, R. Hull, Z. Dlamini, in *Cancer Sensitizing Agents for Chemotherapy*, Z. Dlamini, Ed., Academic Press, Oxford, 2024, p. 17 (https://doi.org/10.1016/B978-0-443-28985-9.00005-7)
4. S. Ashique, M. Bhowmick, R. Pal, H. Khatoon, P. Kumar, H. Sharma, A. Garg, S. Kumar, U. Das, *Adv. Cancer Biol. – Metastasis* **10** (2024) 100114 (https://doi.org/10.1016/j.adcanc.2024.100114)
5. P. Ray, D. Paul, *Pharmacol. Res. – Mod. Chinese Med.* **12** (2024) 100497 (https://doi.org/10.1016/j.prmcm.2024.100497)
6. F. Qi, L. Zhao, A. Zhou, B. Zhang, A. Li, Z. Wang, J. Han, *Biosci. Trends* **9** (2015) 16 (https://doi.org/10.5582/bst.2015.01019)
7. Y. Zhou, J. Zheng, Y. Li, D. P. Xu, S. Li, Y. M. Chen, H. B. Li, *Nutrients* **8** (2016) 515 (https://doi.org/10.3390/nu8080515)

8. M. H. Kang, I. H. Kim, T. J. Nam, *Int. J. Oncol.* **45** (2014) 1036 (https://doi.org/10.3892/ijo.2014.2521)
9. Y. Peng, Y. Wang, C. Zhou, W. Mei, C. Zeng, *Front. Oncol.* **12** (2022) 819128 (https://doi.org/10.3389/fonc.2022.819128)
10. E. C. Aniogo, B. P. George, H. Abrahamse, *Molecules* **25** (2020) 5308 (https://doi.org/10.3390/molecules25225308)
11. N. V. Pervushin, G. S. Kopeina, B. Zhivotovsky, *Biol. Direct* **18** (2023) 69 (https://doi.org/10.1186/s13062-023-00431-4)
12. T. I. Adelusi, A. Q. K. Oyedele, I. D. Boyenle, A. T. Ogunlana, R. O. Adeyemi, C. D. Ukachi, M. O. Idris, O. T. Olaoba, I. O. Adedotun, O. E. Kolawole, Y. Xiaoxing, M. Abdul-Hammed, *Informatics Med. Unlocked* **29** (2022) 100880 (https://doi.org/10.1016/j.imu.2022.100880)
13. D. Jeong, W. S. Yang, Y. Yang, G. Nam, J. H. Kim, D. H. Yoon, H. J. Noh, S. Lee, T. W. Kim, G. H. Sung, J. Y. Cho, *J. Ethnopharmacol.* **146** (2013) 205 (https://doi.org/10.1016/j.jep.2012.12.034)
14. Y. B. Zhang, W. Li, L. Jiang, L. Yang, N. H. Chen, Z. N. Wu, Y. L. Li, G. C. Wang, *Phytochemistry* **153** (2018) 111 (https://doi.org/10.1016/j.phytochem.2018.05.018)
15. J. B. Murray, J. Davidson, I. Chen, B. Davis, P. Dokurno, C. J. Graham, R. Harris, A. Jordan, N. Matassova, C. Pedder, S. Ray, S. D. Roughley, J. Smith, C. Walmsley, Y. Wang, N. Whitehead, D. S. Williamson, P. Casara, T. Le Diguarher, J. Hickman, J. Stark, A. Kotschy, O. Geneste, R. E. Hubbard, *ACS Omega* **4** (2019) 8892 (https://doi.org/10.1021/acsomega.9b00611)
16. G. M. Morris, R. Huey, W. Lindstrom, M. F. Sanner, R. K. Belew, D. S. Goodsell, A. J. Olson, *J. Comput. Chem.* **30** (2009) 2785 (https://doi.org/10.1002/jcc.21256)
17. H. D. Nguyen, *Not. Sci. Biol.* **17** (2025) 12642 (https://doi.org/10.55779/nsb17312642)
18. D. van Der Spoel, E. Lindahl, B. Hess, G. Groenhof, A. E. Mark, H. J. C. Berendsen, *J. Comput. Chem.* **26** (2005) 1701 (https://doi.org/10.1002/jcc.20291)
19. N. Guex, M. C. Peitsch, *Electrophoresis* **18** (1997) 2714 (https://doi.org/10.1002/elps.1150181505)
20. V. Zoete, M. A. Cuendet, A. Grosdidier, O. Michielin, *J. Comput. Chem.* **32** (2011) 2359 (https://doi.org/10.1002/jcc.21816)
21. H. D. Nguyen, *Indian J. Chem.* **64** (2025) 383 (https://doi.org/10.56042/ijc.v64i4.15530)
22. M. S. Valdés-Tresanco, M. E. Valdés-Tresanco, P. A. Valiente, E. Moreno, *J. Chem. Theory Comput.* **17** (2021) 6281 (https://doi.org/10.1021/acs.jctc.1c00645)
23. D. E. Pires, T. L. Blundell, D. B. Ascher, *J. Med. Chem.* **58** (2015) 4066 (https://doi.org/10.1021/acs.jmedchem.5b00104)
24. F. Neese, *WIREs Comput. Mol. Sci.* **15** (2025) e70019 (https://doi.org/10.1002/wcms.70019)
25. G. Knizia, J. E. Klein, *Angew. Chem. Int. Ed.* **54** (2015) 5518 (https://doi.org/10.1002/anie.201410637)
26. M. D. Hanwell, D. E. Curtis, D. C. Lonie, T. Vandermeersch, E. Zurek, G. R. Hutchison, *J. Cheminform.* **4** (2012) 17 (https://doi.org/10.1186/1758-2946-4-17)
27. J. Luo, Z. Q. Xue, W. M. Liu, J. L. Wu, Z. Q. Yang, *J. Phys. Chem., A* **110** (2006) 12005 (https://doi.org/10.1021/jp063669m)
28. R. Das, J. L. Vigneresse, P. K. Chattaraj, *Int. J. Quantum Chem.* **114** (2014) 1421 (https://doi.org/10.1002/qua.24706)

29. P. C. Agu, C. A. Afiukwa, O. U. Orji, E. M. Ezeh, I. H. Ofoke, C. O. Ogbu, E. I. Ugwuja, P. M. Aja, *Sci. Rep.* **13** (2023) 13398 (https://doi.org/10.1038/s41598-023-40160-2)
30. D. A. Schaller, C. D. Christ, J. D. Chodera, A. Volkamer, *J. Chem. Inf. Model.* **64** (2024) 8848 (https://doi.org/10.1021/acs.jcim.4c00905)
31. R. Patil, S. Das, A. Stanley, L. Yadav, A. Sudhakar, A. K. Varma, *PLoS One* **5** (2010) e12029 (https://doi.org/10.1371/journal.pone.0012029)
32. G. Bitencourt-Ferreira, M. Veit-Acosta, W. F. de Azevedo, in *Docking Screens for Drug Discovery*, W. F. de Azevedo Jr., Ed., Springer, New York, 2019, p. 79 (https://doi.org/10.1007/978-1-4939-9752-7_6)
33. H. Alonso, A. A. Bliznyuk, J. E. Gready, *Med. Res. Rev.* **26** (2006) 531 (https://doi.org/10.1002/med.20067)
34. L. Martínez, *PLoS One* **10** (2015) e0119264 (https://doi.org/10.1371/journal.pone.0119264)
35. M. L. Verteramo, M. M. Ignjatović, R. Kumar, S. Wernersson, V. Ekberg, J. Wallerstein, G. Carlström, V. Chadimová, H. Leffler, F. Zetterberg, D. T. Logan, U. Ryde, M. Akke, U. J. Nilsson, *iScience* **27** (2024) 109636 (https://doi.org/10.1016/j.isci.2024.109636)
36. H. D. Nguyen, *Phys. Chem. Res.* **13** (2025) 783 (https://doi.org/10.22036/pcr.2025.535946.2708)
37. H. Rohit, H. Tandon, *J. Mol. Model.* **31** (2025) 291 (https://doi.org/10.1007/s00894-025-06487-5)
38. B. Bashir, A. Z. Clayborne, *Molecules* **30** (2025) 2254 (https://doi.org/10.3390/molecules30112254).

Journal of the Serbian Chemical Society
JSCS-info@shd.org.rs • www.shd.org.rs/JSCS
J. Serb. Chem. Soc. 91 (5) 479–499 (2026)
JSCS–5504
Original scientific paper
Published 12 June, 2026

Fabrication of chitosan membrane modified by vanillin and gelatin for crystal violet dye adsorption

KHABIBI KHABIBI*, NABILA AMALIA IZAAZ AANISA and RETNO ARIADI LUSIANA

Department of Chemistry, Faculty of Sciences and Mathematics, University of Diponegoro 50275 Semarang, Central Java, Indonesia

(Received 9 January, revised 27 January, accepted 9 April 2026)

Abstract: Crystal violet is a cationic dye that poses serious environmental risks when accumulated in aquatic ecosystems due to its high toxicity to living organisms. Therefore, effective treatment methods are required to remove this dye from wastewater. In this study, a chitosan (Cs)-based bioadsorbent membrane, cross-linked with vanillin (V) and modified with gelatin (G), was developed to adsorb crystal violet dye. The chitosan/vanillin membrane was mixed with gelatin at various concentrations of 0.5 (CsVG1), 0.75 (CsVG2) and 1 % (CsVG3). The adsorption process was examined as a function of pH, contact time, initial dye concentration and temperature. Physicochemical characterization of the membranes included porosity, swelling degree, water absorption, FTIR and SEM analysis. The results showed that the optimal parameters for dye adsorption were pH 6, contact time of 80 min, and temperature of 298 K, resulting in 88 % dye removal. The adsorption kinetics followed a pseudo-second-order model and the Freundlich model best described the adsorption isotherm. The thermodynamic analysis demonstrated that the adsorption process was spontaneous and exothermic. Thus, the CsVG membrane has the potential to serve as an effective alternative for removing crystal violet from textile industrial wastewater.

Keywords: biopolymers; bioadsorbent; adsorption membrane; dye removal.

INTRODUCTION

Industrial waste containing synthetic dyes poses substantial risks to environmental integrity and public health. Dyes in water can reduce light penetration and lower dissolved oxygen levels, disrupting the photosynthesis of aquatic organisms. Furthermore, these dyes have the potential to cause carcinogenic and mutagenic consequences in aquatic creatures and humans.[1] It is estimated that approximately 800,000 t of dyes are produced each year, of which about 20 % are discharged into water bodies at the final stage of industrial processes.[2] One type of synthetic dye

* Corresponding author. E-mail: khabibi@live.undip.ac.id
https://doi.org/10.2298/JSC260109020K

that is widely used is cationic dyes, such as crystal violet. The chemical composition of these dyes is characterized by a complex, highly stable aromatic structure, which renders them difficult to degrade naturally.[3] Crystal violet can significantly reduce the amount of light that passes through and alter the appearance of water, even at low concentrations.[4] Given these challenges, recent research highlights the importance of developing practical, environmentally friendly ways to remove these dangerous compounds.

Various waste treatment methods have been developed, such as adsorption, flocculation, membrane filtration, photocatalysis and ion exchange.[5,6] Among these technologies, adsorption is a viable approach for dye waste treatment owing to its high efficacy, cost-effectiveness and operational simplicity. The choice of adsorbent material significantly influences the adsorption process; however, traditional adsorbents, such as commercial activated carbon, have drawbacks including elevated production and regeneration costs, limited selectivity, and reduced reusability.

To improve the efficiency of the adsorption process, bio-based materials are a promising alternative because they are simple, effective and utilize renewable resources. The increasing demand for environmentally friendly processing technologies has encouraged the use of natural biopolymers as efficient adsorbents. Recent studies show that biopolymers such as cellulose, chitin and chitosan are gaining attention for dye adsorption applications due to their abundance, affordability and customizable properties, including surface area, pore size and volume, ease of modification and environmental sustainability.[7] The review also confirms that chitosan is a superior candidate material as a membrane base for effective dye removal in wastewater treatment.

Chitosan is a biopolymer produced by the deacetylation of chitin extracted from marine crustaceans, formed from basic structural units of amino glucose and *N*-acetyl amino glucose connected by *β*-1,4-glycosidic bonds.[8] Chitosan-based adsorbents are effective for dye adsorption owing to their high surface area, numerous functional groups and good biocompatibility. Chitosan contains numerous amino and hydroxyl groups, which are crucial for its interaction with dyes.[9,10] Chitosan's solubility in acidic solutions and its limited mechanical strength necessitate physical and chemical modifications to improve stability and adsorption efficiency.[11] Vanillin is a phenolic aldehyde that can serve as a natural cross-linking agent due to its non-toxic properties and its ability to enhance the mechanical properties of chitosan membranes, thereby offering a safer alternative to synthetic cross-linking agents such as glutaraldehyde.[11] Gelatin is a mixture of peptides and proteins produced from the controlled hydrolysis of collagen. Gelatin has a high adsorption capacity due to the presence of hydroxyl, carboxyl and amino groups along its molecular chain,[12] thereby increasing the number of active sites on the membrane for dye adsorption.

In this study, vanillin-crosslinked chitosan membranes were synthesized *via* a Schiff base modification reaction on chitosan, then combined with gelatin to increase the number of active sites on the membrane surface during dye removal from aqueous solutions. The chitosan/vanillin/gelatin (CsVG) membrane was characterized to determine its physicochemical properties using swelling degree tests, Fourier transform infrared spectroscopy (FTIR), scanning electron microscopy (SEM) and X-ray diffraction (XRD). Crystal violet was used as a model toxic cationic dye to assess the adsorption capacity of the CsVG membrane. The adsorption mechanism, isotherm model, kinetics and thermodynamic parameters were also analyzed to understand the interaction process between the dye and the membrane. The novelty of this research is that there are no reports in the literature describing the use of modified chitosan, vanillin and gelatin biopolymers as adsorbent membranes for the removal of crystal violet dye. The development of CsVG membranes as adsorbent membranes is expected to be a promising technology for effective, environmentally friendly dye removal from wastewater.

EXPERIMENTAL

Materials

The materials used in this study were chitosan (*MW* = 40,000 g/mol, *DD* = 88.5 %, Cv. Bio Chitosan Indonesia), CH_3COOH (*MW* = 131.11 g/mol, Merck), NaOH (*MW* = 40 g/mol, Merck), vanillin (*MW* = 152.15 g/mol, Merck), gelatin (Merck), crystal violet ($C_{25}H_{30}C_lN_3$, *BM*= 407.98 g/mol, Merck), HCl, (37 %, Merck) and distilled water.

Synthesis of chitosan membrane

1.5 g of chitosan was dissolved in 100 mL of 1 % acetic acid. The solution was stirred continuously for 24 h at room temperature. The resulting chitosan solution was poured into a Petri dish and dried at 40–50 °C. The chitosan membrane was immersed in 1 M NaOH, washed with distilled water and then dried.

Synthesis of chitosan/vanillin/gelatin (CsVG) membrane

Chitosan (1.5 g) was dissolved in 60 mL of 1 % acetic acid solution with stirring for 24 h at room temperature. Separately, vanillin (0.5 g) was dissolved in 100 mL of 1 % acetic acid and stirred for 2 h at 50 °C. The gelatin solution was prepared by dissolving gelatin in 100 mL of distilled water at 50 °C with agitation for 2 h, at concentrations of 0.5 (CsVG1), 0.75 (CsVG2) and 1 % (CsVG3). The chitosan solution was subsequently combined with 20 mL of vanillin solution and agitated for 4 h at 60 °C to facilitate cross-linking reactions. Next, the gelatin solution was added to the chitosan–vanillin mixture, and stirring was continued for 24 h until a homogeneous solution was formed. The resulting solution was then poured into Petri dishes and dried at 50 °C until a membrane was formed. The preparation process of the CsVG membrane is illustrated in Fig. 1.

Characterization of membrane

All CS, CS/Van, and Cs/Van/Gel (CsVG) membranes were characterized using various analytical techniques. Fourier-transform infrared (FTIR) spectra were recorded in the range of 4000–400 cm^{-1} at a resolution of 1 cm^{-1} resolution with 25 scans per measurement using a Shimadzu FTIR spectrometer to identify changes in functional groups and the formation of new

bonds. The crystal structure was analyzed using X-ray diffraction (XRD) using a Rigaku Mini-flex 600 instrument with CuKα radiation over a 2θ range of 3–70° scanning angle with a step size of 0.02° and a scan rate of 1° min. Dye concentrations were analyzed using a UV–Vis spectrophotometer (Shimadzu UV-1280, serial No. A120660) at the maximum wavelength of each dye. Surface morphology images were obtained using a scanning electron microscope (SEM, Thermo Scientific Quattro S).

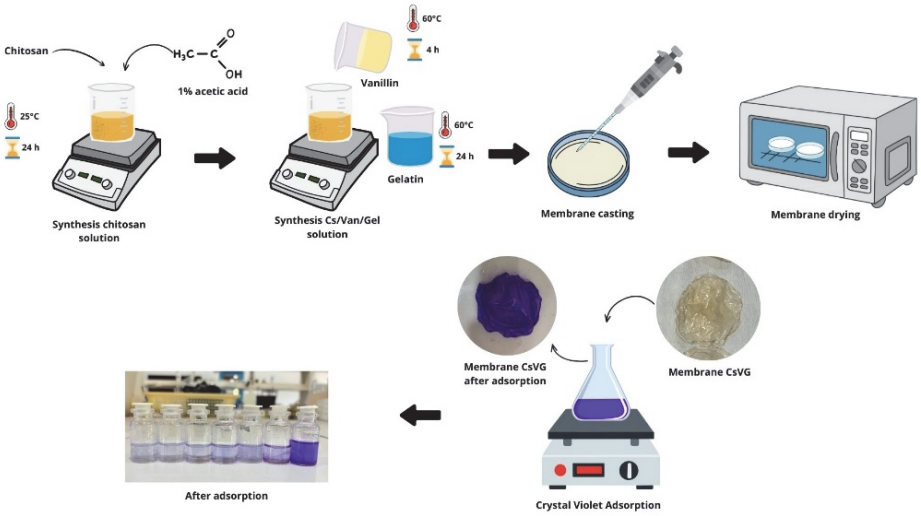

Fig. 1. Schematic diagram illustrating the preparation and dye adsorption processes of a Cs/Van/Gel membrane.

Point of zero charge (pzc)

The pHpzc of the membrane was determined through the pH shift method. 50 mL of a 0.1 M NaCl solution was prepared for the experiment. The pH of the solution was adjusted to range from 2 to 12 using 0.1 mol NaOH and 0.1 mol HCl. Each solution received 0.05 g of membrane and was allowed to stabilize for 24 h. The final pH value was recorded. The pHpzc value was determined by plotting ΔpH against pH_i and identifying the point at which ΔpH equaled zero. ΔpH can be calculatedas:

$$\Delta pH = pH_i - pH_f \quad (1)$$

where pH_i is and pH_f are initial and final pH, respectively.[13]

Physical characteristics of membranes

The membrane porosity was determined by the gravimetric method at room temperature and neutral pH. The membrane's initial weight was measured, and it was then immersed in water for 24 h. The immersed membrane was removed from the water, excess water was removed by draining on tissue paper, and it was weighed again. For each membrane, the test was repeated three times, and the porosity value was calculated using Eq (2)

$$\text{Porosity} = 100\frac{w_w - w_d}{V_m \rho_w} \quad (2)$$

where w_d is the dry membrane mass (g), w_w is the wet membrane mass after being immersed in distilled water for 24 h (g), V_m is the membrane volume (cm^3) and ρ_w is the density of water (1 g/cm^3).[14]

To determine the degree of swelling in water, the membrane was measured for its initial and final diameters after immersion in water for 24 h. The test was conducted three times. The swelling ratio was calculated using Eq. (3), where l_w is the wet membrane diameter after immersion (cm) and l_d is the dry membrane diameter (cm):[15]

$$\text{Swelling} = 100\frac{l_w}{l_d} \tag{3}$$

Water absorption was calculated from the dry membrane weight and the membrane weight after 5 h of soaking. Every hour, the membrane was dried and then weighed. Eq. (4) shows the relationship between the wet membrane and the dry membrane mass used to determine the water uptake value:[16]

$$\text{Water uptake} = 100\frac{w_w - w_d}{w_d} \tag{4}$$

Dye adsorption study

The adsorption test was based on the work by Farasati Far.[17] To make a 1000 mg/L stock solution of crystal violet, 1 g of dye was dissolved in 1 L of distilled water until fully dissolved. The initial test was conducted using 50 mL of a 5 mg/L dye solution, with a contact time of 2 hours, a solution temperature of 25 °C, and a pH ranging from 4.0 to 8.0 adjusted by adding HCl (0.01 M) and NaOH (0.01 M). The dye solution and membrane were placed in an Erlenmeyer flask and stirred with a shaker at 150 rpm. After that, 5 mL of the dye solution was taken, and its absorbance was measured at 591 nm. The test continued with different settings, including contact time (20, 60, 80, 100 and 120 min), initial dye concentration (3, 5, 7, 9 and 12 mg/L) and temperature (25, 35 and 45 °C). We systematically tested these parameters to determine the optimal conditions for crystal violet adsorption. The dye removal efficiency was determined using Eqs. (5) and (6):

$$q = \frac{c_i - c_t}{c_i}V \tag{5}$$

$$RE\% = 100\frac{c_i - c_t}{c_i} \tag{6}$$

Re% is the removal efficiency, c_i and c_t (mg/L) are the initial and final concentrations or equilibrium concentrations of the cationic dye crystal violet, V is the solution volume (L), and w is the mass of adsorbent (g).

Adsorption kinetics

The adsorption kinetics of the crystal violet dye were analyzed to understand the rate and mechanism of adsorption. The kinetic study was conducted using two commonly used models: first-order and second-order.

Pseudo-first order kinetics

This analysis is based on the principle that the adsorption rate is directly proportional to the difference between the maximum adsorption capacity and the amount of dye adsorbed at a given time. Linear and non-linear forms of the pseudo-first-order model were used.[18]

Pseudo-second-order kinetics

The pseudo-second-order kinetic model indicates that the adsorption process is influenced by intricate interactions, such as chemical bonding or the involvement of adsorption sites, suggesting a slow equilibrium system, particularly at elevated concentrations of the substance.[19] The linear and non-linear forms of the pseudo-second-order model were used.

Adsorption isotherm

An adsorption isotherm is an adsorption phenomenon that occurs at a constant temperature. The adsorption isotherm was studied using the Langmuir[20] and the Freundlich[21] models.

Thermodynamics of adsorption

The effect of temperature on dye adsorption was investigated to evaluate the thermodynamics of adsorption. Thermodynamic parameters such as Gibbs energy change (ΔG), enthalpy change (ΔH) and entropy change (ΔS) can be calculated to provide a comprehensive understanding of the adsorption process.[22] Analysis of thermodynamic parameters is useful for analyzing the nature of adsorption interactions and the stability of the complexes formed.[23]

RESULTS AND DISCUSSION

Preparation of Cs/Van/Gel (CsVG) membrane

The polymer chain of chitosan, a cationic polysaccharide, has a high density of hydroxyl and amino groups.[10] A positively charged ammonium group ($-NH_3^+$) was created by protonating the amino groups in chitosan after it was dissolved in acetic acid for this investigation. To enhance the membrane's properties, it was modified *via* vanillin cross-linking. The mechanism of the cross-linking reaction between chitosan and vanillin involves two different stages. The first stage involves the aldehyde group of vanillin reacting with the amine group of chitosan to form a Schiff base and an imine group. The imine group indicates that chitosan has been successfully cross-linked with vanillin. The covalent bonds formed during cross-linking can increase the membrane's mechanical strength. During the second stage, hydrogen bonds form between the hydroxyl group of vanillin and the hydroxyl group of chitosan or gelatin, thereby enhancing hydrophilicity and fostering a more organized structure.[25] Gelatin is subsequently incorporated *via* mixing to enhance the membrane's active sites. The $-NH_3^+$ group on protonated chitosan interacts with the carboxylate group on gelatin, which is often negatively charged in solution, thus generating electrostatic interactions.[26] The functional groups on chitosan and gelatin interact with the target chemicals, establishing hydrogen bonds.

Characterization studies

FTIR Analysis. The FTIR spectrum of the membrane shown in Fig. 2 confirms that changes occur at various stages of modification. Based on Fig. 2, chitosan shows peaks at 3358 (O–H stretching) and 3293 (primary N–H), 2878 (C–H stretching with CH_2 symmetry), 1644 and 1589 (amine twin groups), 1378 (asymmetric C–H from CH_2) and 1028 cm^{-1} (C–O–C). In the Cs/VAN membrane spectrum, the peaks at 3354 and 3297 cm^{-1} shifted from the chitosan spectrum due

to the formation of hydrogen bonds between the NH_2 of chitosan and the OH of vanillin.[27] The peak at 1644 cm^{-1} in chitosan shifted to 1639 cm^{-1}, indicating C=N stretching vibrations, which indicate the formation of a Schiff base bond between the vanillin aldehyde group and the chitosan amine group.[28] The overlap of C=O stretching vibrations originating from the secondary amide group in chitosan can make C=N stretching difficult to identify in the FTIR spectrum.[29] The broad peak at 1588 cm^{-1}, assigned to N–H bending vibrations of a secondary amine, becomes weaker, indicating that some of the amine groups have been involved in the cross--linking process.[30] In addition, a peak at 1503 cm^{-1} is attributed to the benzene ring of vanillin, and a peak at 827 cm^{-1} corresponds to the bending vibration of the phenolic hydroxyl group in vanillin. This is similar to the study by Zhang,[31] in which the addition of vanillin produced a new peak at a wavelength of 1633 cm^{-1} (C=N), a shift in the absorption peak of the benzene ring from 1584 to 1586 cm^{-1}, and a peak at 857 cm^{-1} indicating the phenolic –OH group.

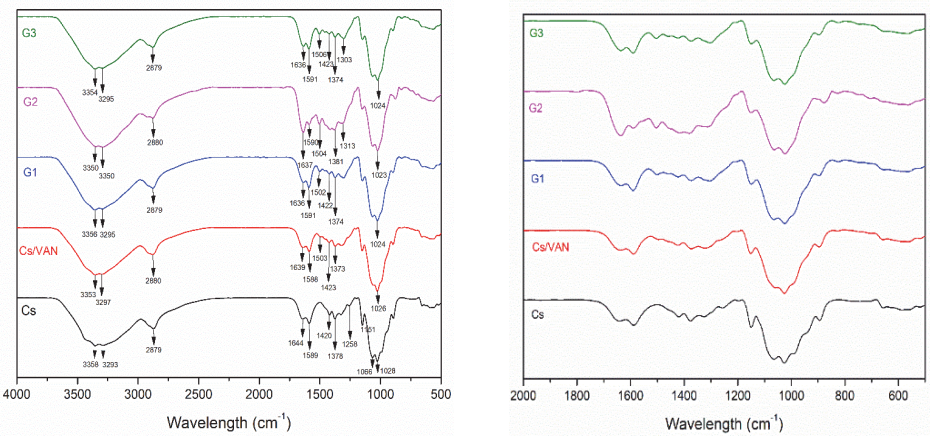

Fig. 2. FTIR spectra of Cs, Cs/VAN, G1 (Cs/Van/Gel 0.5 %), G2 (Cs/Van/Gel 0.75 %), G3 (Cs/Van/Gel 1 %) in different wavelength regions.

In the CsVG1, CsVG2, and CsVG3 membrane spectra, the OH and –NH bands shifted to lower wavenumbers because these peaks indicate intermolecular hydrogen bonds from the hydroxyl group and NH stretching from the amide group in gelatin and chitosan. At the same time, the peak at a wavelength of 1637 cm^{-1} confirms the formation of imine bonds (C=N). The C–O and C–N group peaks appear at 1024 cm^{-1}.

XRD Analysis. The XRD patterns of Cs, Cs/VAN and CsVG2 membranes are shown in Fig. 3. Pure Cs exhibits two characteristic semi-crystalline peaks at 2θ 10.89 and 20.36°,[32] which are related to the partial regularity of the polymer chain due to intra- and intermolecular hydrogen bonds between the NH_2 and OH groups.[33] The diffraction peak at about 20° became broader and less intense after

cross-linking with vanillin. It also moved to 2θ 22.29°. This change shows that chitosan and vanillin interact at the molecular level, altering the regularity of the chitosan structure. The lower intensity indicates that crystallinity has decreased because there are fewer free NH_2 groups.[34]

In the CsVG membrane, a new reflection appears at 2θ 16.99° and a peak shift from 20.36 and 22.33° and in the Cs peak shift from 22.42 to 23.39°. The shift to a higher angle indicates a decrease in *d*-spacing and the formation of a more compact polymer network through interactions among chitosan, vanillin, and gelatin.

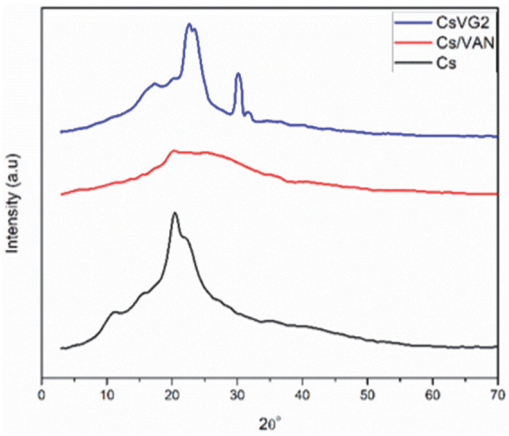

Fig 3. X-ray diffraction patterns of Cs, Cs/VAN and CsVG2 membranes.

SEM Analysis. Scanning electron microscopy (SEM) images of the Cs, Cs/VAN and CsVG membrane surfaces are shown in Fig. 4.

In Fig. 4a, SEM analysis of the chitosan membrane reveals an uneven, dense surface morphology with no visible voids, indicating reduced permeability and adsorption capacity. Fig. 4b illustrates the cross-sectional morphology of the Cs/ /VAN membrane surface, showing a smoother surface accompanied by the formation of cavities. This may be due to cross-linking, which can significantly affect the film's internal microstructure, including cavities, adhesion, smoothness and compactness. The uniformity of the pores is due to the formation of Schiff bases and hydrogen-bond interactions arising from vanillin cross-links. In Fig. 4c, the CsVG2 membrane with a gelatin concentration of 0.75 % exhibits a more consistent and smoother surface than the chitosan and chitosan/vanillin membranes, and it shows visible pores. This indicates good homogeneity among chitosan, gelatin and vanillin. The addition of gelatin to the membrane produces a smoother surface with a more homogeneous structure, thereby increasing water absorption.[35] Research by Bakouri[36] also shows that cross-sections of arginine-modified chitosan/ /gelatin films exhibit a similar dense internal structure, indicating a smooth, uniform cross-section. The more porous structure of the CsVG membrane results from

electrostatic interactions between chitosan and gelatin, which form a sponge-like structure that enhances the membrane's overall integrity.

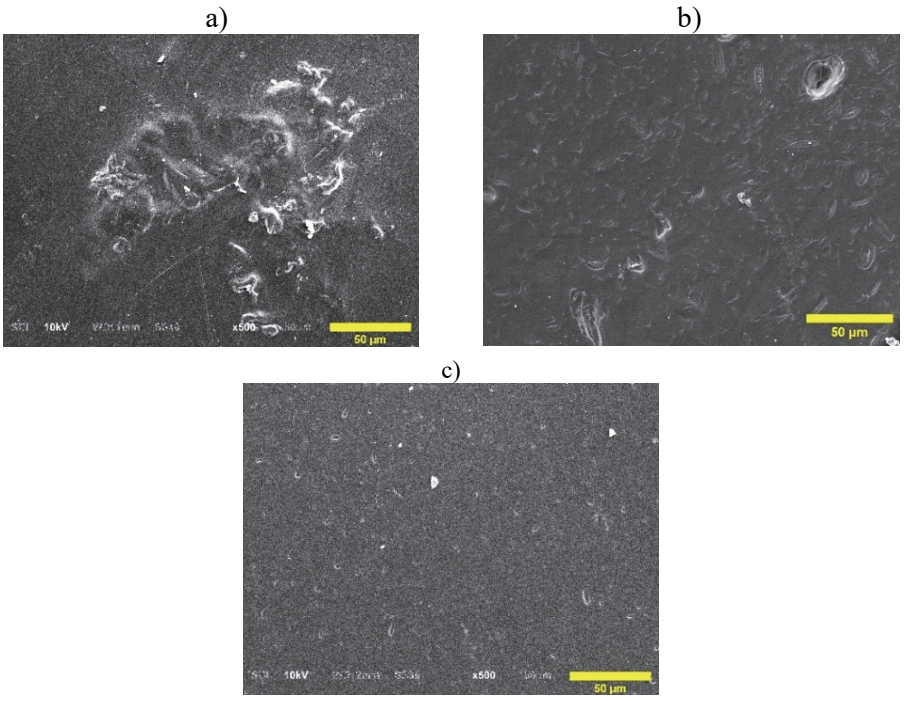

Fig. 4. SEM images at 500× magnification of: a) Cs, b) Cs/VAN and c) CsVG2 membranes after adsorption.

Point of zero charge. The point of zero charge (pHpzc) is the pH value at which the surface charge of the adsorbent is neutral.[13] At pH values below the pHpzc, Fig. 5, the adsorbent surface is positively charged, whereas at pH values above the pHpzc, it becomes negatively charged. This surface charge property plays an important role in the adsorption process because it affects the interaction between the adsorbent and the adsorbate. In this study, the cationic dye crystal

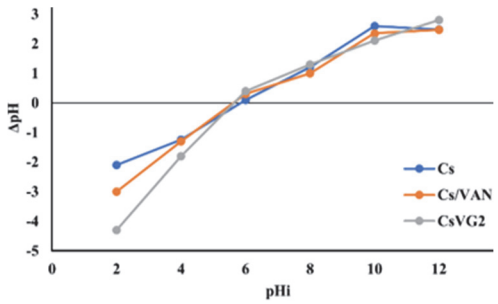

Fig. 5. pHpzc graph in the pH range 2–12.

violet (CV) was used, and it must be adsorbed at a high pH (pH > pHpzc) to achieve maximum adsorption.[37] Based on Fig. 5, the pHpzc values obtained were 5.8 for the Cs membrane and 5.6 for the Cs/VAN and CsVG2 membranes.

Physical characterization of membrane

Porosity, swelling and water uptake are critical physicochemical parameters in membranes, as they influence permeation, fouling, and polymer–water interactions, which in turn determine adsorption capacity and kinetics. The results of the physicochemical characterization of the membrane are presented in Fig. 6.

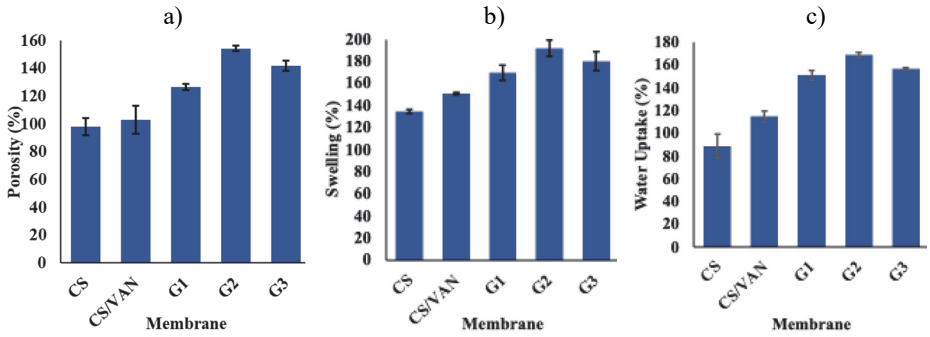

Fig. 6. a) Porosity, b) swelling degree and c) water uptake for the pure membrane and modified membranes.

To determine the effect of membrane modification with vanillin and gelatin, membrane characteristics, including porosity, degree of swelling and water absorption, were measured, as shown in Fig. 6. Fig. 6 shows that porosity, degree of swelling and water absorption increased linearly. The lowest values were obtained for the pure chitosan membrane and the physicochemical properties of the membrane increased with increasing modification levels. Among the tested variations, the CsVG2 membrane (Cs/Van/Gel 0.75 %) exhibited the best physicochemical characteristics.

Fig. 6a shows that the porosity of the pure chitosan membrane is 97.99 %, whereas that of the CsVG2 membrane it increases to 141.86 %. This indicates that increasing the gelatin concentration results in a more porous membrane structure. The presence of carboxyl groups in gelatin increases porosity through electrostatic interactions between chitosan and gelatin.[38] This increase in porosity indicates that the membrane has more empty spaces that can be filled with water, thereby increasing the internal surface area and available pore volume, which ultimately improves adsorption capacity.

The degree of swelling values in Fig. 6b indicate that the lowest swelling occurs in the pure chitosan membrane, at 134.59 %. After adding the vanillin cross-linking agent to the Cs/VAN membrane, the degree of swelling increased to

150.60 %. The addition of gelatin to the membrane significantly increased the degree of swelling. In the CsVG1 membrane, the swelling value increased to 169.78 %, and in the CsVG2 membrane with a gelatin concentration of 0.75 %, it reached 191.98 %. However, when the gelatin concentration was increased to 1 % (CsVG3 membrane), the membrane's swelling decreased to 180.01 %. The formation of cross-links between chitosan and vanillin via the Schiff base reaction produces a more compact membrane structure, reducing the number of available hydrophilic groups and thereby decreasing the membrane's swelling value.[39] However, in this study, the addition of vanillin still increased the degree of expansion. This indicates that the number of remaining hydrophilic groups is still sufficient to allow swelling, in line with the findings reported by Hu.[40]

The increase in the degree of swelling is also supported by the addition of gelatin to the chitosan matrix because gelatin has carboxyl groups that are hydrophilic and can increase the number of active groups on the membrane surface. A denser polymer network formed by stronger interactions among chitosan, vanillin, and gelatin can reduce swelling at higher gelatin concentrations. This tighter structure makes the membrane less able to absorb and expand with water, as it has less free space and fewer internal pores.

Along with the increase in porosity and degree of swelling, the percentage of water absorption shown in Fig. 6c indicates that the CsVG2 membrane has the most optimal physicochemical characteristics. A higher water-absorption capacity shows that water molecules are more strongly attracted to the membrane surface, thereby increasing the membrane's hydrophilicity. This increased hydrophilicity is critical for improving membrane performance, as it enhances its ability to absorb dyes.

Adsorption removal of crystal violet

Adsorption with variation in pH. The effect of pH on the adsorption capacity of the Cs/Van/Gel membrane was assessed by adjusting the pH of the dye solution from 4 to 8 at an initial concentration of 5 mg/L. This pH range was chosen because it represents conditions that are practically relevant for dye adsorption applications. Variations in pH are important because solution pH is a significant parameter that affects adsorption, both by altering the adsorbent surface charge and the degree of adsorbate ionization. As shown in Fig. 7, the percentage of dye removal increased with increasing solution pH from 4, reached a maximum at pH 6, and then decreased at higher pH values. Under strongly acidic conditions (pH < 4), chitosan may partially dissolve because of excessive protonation of amino groups, leading to structural swelling. Conversely, highly alkaline conditions can result in structural instability.

In acidic environments, the concentration of H^+ is significantly elevated, leading these ions to compete with positively charged crystal violet (CV) molecules

for negatively charged active sites on the adsorbent's surface. This condition reduces the number of sites available for CV molecules and decreases adsorption efficiency. As pH increases, the number of H^+ decreases, and the adsorbent surface tends to become negatively charged, thereby increasing electrostatic interactions with positively charged CV molecules.[41] However, when the pH is increased from 6 to 7 and 8, CV adsorption decreases. This suggests that, alongside electrostatic forces in the acidic range, mechanisms such as π–π stacking and/or hydrogen bonding are anticipated to become more prominent and potent at neutral or alkaline pH.[42,43]

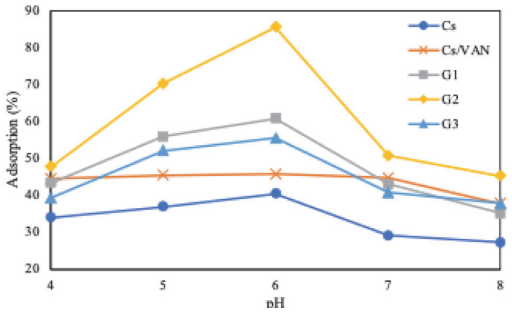

Fig. 7. Effect of pH on the CV adsorption efficiency (%); initial dye concentration, 5 mg/L, 25 °C, contact time 120 min.

At pH values above 6, adsorption efficiency decreases again, possibly due to changes in surface charge or the formation of repulsive forces between the adsorbate and adsorbent. Crystal violet is a basic dye with a pK_a value of 0.8.[44] Because of its low pK_a, this molecule remains ionized across the experimental pH range, behaving as a cationic dye under all pH conditions tested.

Adsorption with variation in time: kinetic studies. The removal of crystal violet dye by chitosan membranes and modified CsVG membranes is shown in Fig. 8. The adsorption capacity of the membrane increased until the 80th min, which facilitated greater adsorption. Subsequently, the adsorption rate decreased because most active sites were gradually filled, thereby inhibiting the diffusion of crystal violet molecules to the membrane surface. The adsorption capacity of the Cs membrane at 80 min was 35.86 %, and the maximum adsorption capacity of

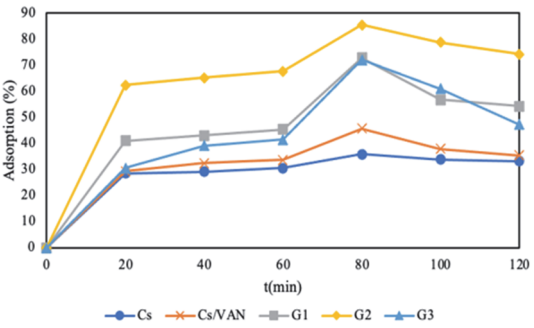

Fig. 8. Effect of contact time (min) on the CV adsorption efficiency (%); initial dye concentration, 5 mg/L; pH 6.

the CsVG2 membrane reached 85.57 %. Based on these data, the optimum adsorption time for crystal violet removal by this membrane system is 80 min.

The dye adsorption process was then analyzed using first-order and second-order pseudo-kinetic models. Adsorption kinetics provide information about the adsorption rate, the mechanism of CV adsorption by the membrane, and help determine the possible rate-controlling steps. The experimental data were analyzed using first-order and second-order pseudo-kinetic equations *via* linear and non-linear fitting. Kinetic parameters obtained from the analysis are summarized in Table I.

TABLE I. Adsorption kinetics study

Form	Plot	Parameter	Value
	Pseudo-first-order		
Linier	c_e/q_e *vs.* c_e	k_1 / min^{-1}	0.0011
		q_e / mg g^{-1}	2.3165
		R_2	0.61
		SSE	0.8653
Non-linear	q_t *vs.* t	k_1 / min^{-1}	0.074
		q_e / mg g^{-1}	1.4817
		R_2	0.9549
		SSE	0.0835
	Pseudo-second-order		
Linier	log qe vs log Ce	k_2 / g mg^{-1} min^{-1}	0.1852
		q_e / mg g^{-1}	2.3479
		R_2	0.9928
		SSE	1.4788
Non-linear	q_t *vs.* t	k_2 / g mg^{-1} min^{-1}	0.0809
		q_e / mg g^{-1}	1.6173
		R_2	0.9648
		SSE	0.065

Based on the kinetic parameters obtained from linear and non-linear regression analyses, the adsorption process is better described by the pseudo-second-order model than by the pseudo-first-order model. The pseudo-second-order model yielded higher coefficients of determination (R^2 of 0.9928 and 0.9648) than the pseudo-first-order model. Due to potential changes in the error structure resulting from linearization, model suitability was primarily assessed using nonlinear regression and *SSE* values. The pseudo-second-order model demonstrated a lower *SSE*, signifying a better fit to the experimental data. The fit of the pseudo-second-order model to the experimental data showed that the adsorption rate was controlled by the interaction between the active sites of the adsorbent and the dye molecules, where the dye-binding process involved the exchange or sharing of electron pairs between the active sites of the adsorbent and the cationic groups on the

adsorbate.[45] Other studies by Agbor Tabi[46] and Ahmad and Ejaz[47] also showed that crystal violet dye is adsorbed through chemisorption.

Adsorption with variation in initial concentration of adsorbates. The effect of the initial dye concentration on adsorption was studied by varying the concentration of crystal violet in the range of 3, 5, 7, 9 and 12 mg/L. Conversely, all other adsorption variables were kept constant, namely pH 6.0 and an adsorption time of 80 min.

Based on the results shown in Fig. 9, increasing the initial dye concentration gradually decreases the adsorption efficiency. At low crystal violet concentrations, the number of dye molecules is relatively proportional to the number of active sites available on the membrane surface, allowing CV molecules can be easily adsorbed through various interaction mechanisms, such as hydrogen bonding, electrostatic interactions, and π–π interactions between the CsVG membrane and the functional groups of crystal violet. At higher crystal violet concentrations, the number of dye molecules increases, but the number of available active sites remains limited. This discrepancy between the number of dye molecules and the number of available adsorption sites reduces the effectiveness of adsorption.[48]

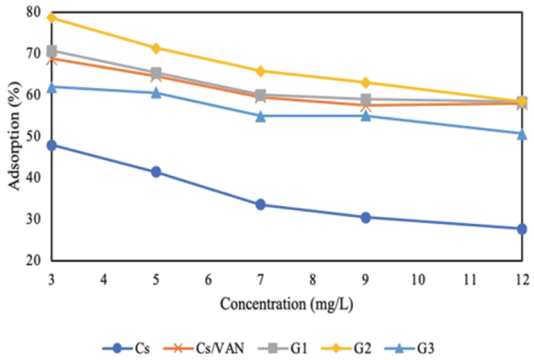

Fig. 9. Effect of dye concentration on the CV adsorption efficiency (pH 6.0; t = 80 min).

The adsorption performance of crystal violet on CsVG membranes was evaluated using adsorption isotherm studies with the Langmuir and Freundlich models. The results of the isotherm studies were used to determine the qualitative properties of the adsorbate–adsorbent systems. According to the Langmuir adsorption isotherm, adsorption occurs as a monolayer on a homogeneous surface. In contrast, the Freundlich isotherm refers to the amount of adsorbate adsorbed per unit mass of adsorbent in a heterogeneous system. The results of the CsVG membrane isotherm study are shown in Table II.

The adsorption process can be determined by the highest regression coefficient value (R^2) based on the isotherm parameters and membrane regression coefficients in Table II. The R^2 value for the Cs membrane in Langmuir is 0.9693 and in Freundlich is 0.9873, while in the CsVG2 membrane (Cs/Van/Gel 0.75 %), the

R^2 value in Langmuir is 0.9657 and in Freundlich is 0.9989. This finding suggests that the crystal violet adsorption system on all adsorbents follows the Freundlich isotherm model, as evidenced by an R^2 value exceeding the Langmuir model threshold and approaching 1. The Freundlich isotherm model assumes adsorption on a heterogeneous surface, leading to the formation of a multilayer. Additionally, the phenomenon is attributed to physical adsorption through van der Waals or weak interactions between crystal violet and the adsorbent surface.[49]

TABLE II. Isotherm adsorption study

Membrane	Langmuir			Freundlich		
	K_L	*Qmax* / mg g^{-1}	R^2	K_F / L mg^{-1}	*n*	R^2
Cs	2.6205	0.2683	0.9693	0.7796	2.1372	0.9873
Cs/VAN	8.5034	0.1633	0.8456	0.9880	1.4438	0.9896
CsVG1	8.1766	0.1823	0.854	0.8958	1.4925	0.99
CsVG2	6.0827	0.3939	0.9657	0.6103	1.8758	0.9989
CsVG3	7.8247	0.1440	0.9528	1.0899	1.3976	0.99

Adsorption with variation in temperature: thermodynamic studies. The effect of temperature on the adsorption process is shown in Fig. 10. The temperature applied in this experiment were 298, 308, 318 and 328 K. The best results were obtained with the CsVG2 membrane (Cs/Van/Gel 0.75 %), which achieved adsorption percentages of 88.12 % at 298 K and 47.33 % at 328 K. The adsorption efficiency of crystal violet decreased with increasing temperature.

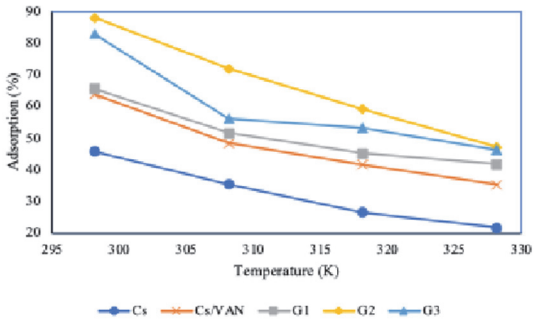

Fig. 10. Effect of temperature on the CV adsorption efficiency (pH 6.0; *t* = = 80 min: dye concentration, 3 mg/L).

The exothermic nature of the adsorption process is indicated by the decrease in adsorption capacity with increasing temperature. Thermodynamic parameters used to describe the adsorption process, such as ΔG, ΔH and ΔS, support this observation. The slope and intercept of the van't Hoff plot are used to obtain the values of $\triangle H$ and $\triangle S$. Table III presents the results of the thermodynamic parameter calculations.

According to Table III, as the temperature increases, the ΔG value indicates that the adsorption process becomes more spontaneous. The negative ΔH value

indicates that the adsorption process of crystal violet is exothermic. The Δ*S* value yields good affinity between the CsVG2 membrane and crystal violet, thereby reducing unpredictability at the solid/liquid interface during adsorption.

TABLE III. Thermodynamic parameters for CV adsorption

Membrane	Temperature, K	Δ*G* / J mol^{-1}	Δ*H* / kJ mol^{-1}	Δ*S* / J mol^{-1} K^{-1}
Cs	298.15	–201	–32.86	–111
	308.15	–1489		
	318.15	–2684		
	328.15	–3490		
CsVG2	298.15	–4229	–48.98	–150
	308.15	–2429		
	318.15	–1001		
	328.15	–291		

Interactions between CsVG membrane and the adsorbates

The adsorption mechanism depends on the functional groups and surface porosity of the adsorbent and the adsorbate molecules. An estimate of the mechanism by which the membrane-bound active groups interact with crystal violet is shown in Fig. 11.

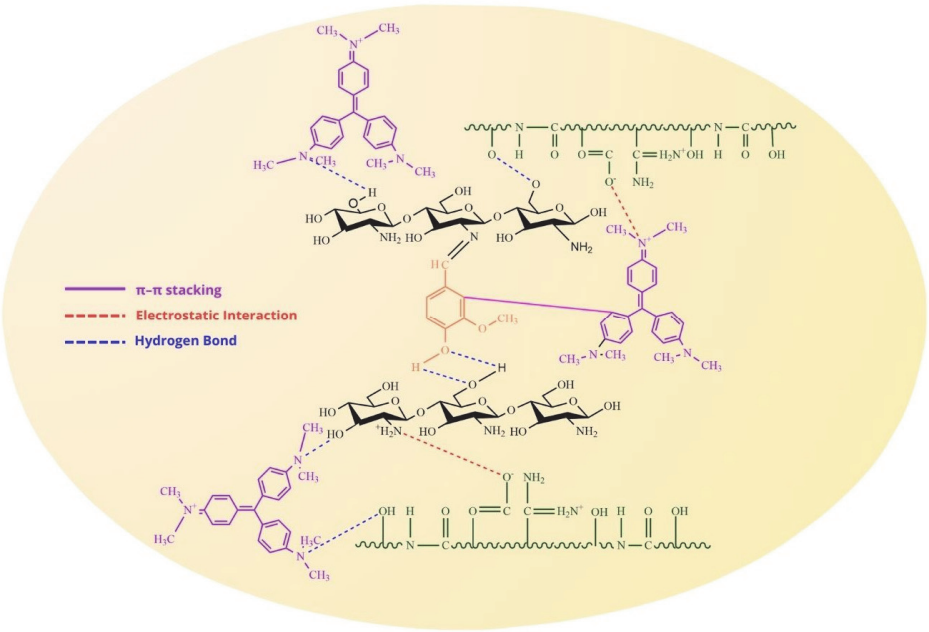

Fig. 11. Estimated adsorption mechanism.

Possible interreaction mechanisms between the active sites on the surface of the chitosan/vanillin/gelatin membrane and crystal violet include electrostatic interactions, π–π interactions and hydrogen bonding. Electrostatic bonds occur between the negative charge of the $–COO^-$ group in gelatin and the positive group (N^+) in crystal violet. The hexagonal structure of vanillin and the benzene ring of crystal violet can enhance adsorption by acting as electron donors and acceptors *via* π–π stacking. In addition, H atoms from oxygen-containing functional groups on the surface of the CsVG membrane can form hydrogen bonds with N atoms in crystal violet.

Reusability study

Reusability and stability are important parameters in evaluating the performance of adsorbents for water treatment. Therefore, the Cs and CsVG2 membranes were retested at the optimum pH for three consecutive adsorption cycles. Based on Fig. 12, the initial use showed the highest adsorption efficiency. After three cycles, the CsVG2 membrane still maintained a fairly high adsorption capacity, although the efficiency of crystal violet (CV) adsorption decreased from 89 to 49 %. This reduction in efficiency is probably caused by some CV molecules being strongly bound to active sites *via* electrostatic interactions, π–π interactions or hydrogen bonds. As a result, the number of available active sites is reduced. In addition, pore blocking by residual dye molecules may occur, inhibiting the diffusion of adsorbates into the membrane structure. This decrease indicates that optimization of the regeneration method is still needed to improve membrane reuse performance.

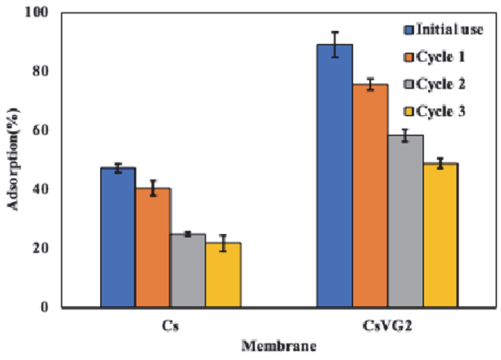

Fig. 12. The cycles of reusability of the membrane.

CONCLUSION

In this study, CsVG membranes were developed from chitosan crosslinked with vanillin and modified with varying concentrations of gelatin (0.5, 0.75 and 1 %). The modified membranes exhibited good adsorption of crystal violet, with the optimum membrane (CsVG2) obtained at a gelatin concentration of 0.75 %. The addition of vanillin and gelatin improved the physical characteristics of the membrane, such as

porosity, swelling and water absorption, in comparison to the pure chitosan membrane. The optimal parameters for dye adsorption were identified as pH 6, a contact time of 80 min, an initial dye concentration of 3 mg/L and a temperature of 298 K, yielding 88 % dye removal.

Adsorption kinetics conformed to a pseudo-second-order model, suggesting that both the contact time and the concentration of the dye influenced the adsorption rate and that chemical interactions occurred between the adsorbent and the adsorbate. The isotherm best fits the Freundlich model, with an R^2 value of 0.9989 at 298 K. The thermodynamic results showed that the adsorption process is exothermic ($\Delta H < 0$) and spontaneous ($\Delta G < 0$).

Overall, the results of this study indicate that the CsVG bioadsorbent membrane has good physicochemical properties and the potential to be developed as an effective, environmentally friendly adsorbent for the removal of crystal violet dye from wastewater. Further research is needed to evaluate the membrane's regeneration and reuse capabilities and to examine its application in more complex wastewater systems.

Acknowledgement. The authors would like to acknowledge the Institute for Research and Community Service, Diponegoro University, for its support through the 2025 research program.

ИЗВОД

ИЗРАДА ХИТОЗАНСКЕ МЕМБРАНЕ МОДИФИКОВАНЕ ВАНИЛИНОМ И ЖЕЛАТИНОМ ЗА АДСОРПЦИЈУ БОЈЕ КРИСТАЛ-ВИОЛЕТ

KHABIBI KHABIBI, NABILA AMALIA IZAAZ AANISA и RETNO ARIADI LUSIANA

Department of Chemistry, Faculty of Sciences and Mathematics, University of Diponegoro, 50275 Semarang, Central Java, Indonesia

Кристал-виолет (CV) је катјонска боја која представља озбиљне ризике по животну средину када се акумулира у воденим екосистемима због своје високе токсичности за живе организме. Због тога су потребне ефикасне методе третмана за уклањање ове боје из отпадних вода. У овој студији, хитозанска (Cs) биоадсорбент мембрана, умрежена са ванилином (V) и модификована желатином (G), развијена је за апсорпцију CV. Хитозан/ /ванилин мембрана је помешана са желатином у различитим концентрацијама, 0,5 (CsVG1), 0,75 (CsVG2) и 1 % (CsVG3). Процес адсорпције је испитан у функцији pH, времена контакта, почетне концентрације боје и температуре. Мембрана је окарактерисана мерењем порозности, степена бубрења, апсорпције воде, FTIR и SEM. Резултати су показали да су оптимални параметри за адсорпцију боје били pH 6, време контакта 80 min и температура 298 K, што је резултирало уклањањем 88 % боје. Кинетика адсорпције пратила је модел псеудо-другог реда, а Freundlich модел најбоље је описао изотерму адсорпције. Термодинамичка анализа је показала да је процес адсорпције био спонтан и егзотерман. Дакле, CsVG мембрана има потенцијал да послужи као ефикасна алтернатива за уклањање кристално љубичасте из текстилних индустријских отпадних вода.

(Примљено 9. јануара, ревидирано 27. јануара, прихваћено 9. априла 2026)

REFERENCES

1. E. Alver, A. Ü. Metin, *Chem. Eng. J.* **200**–**202** (2012) 59 (https://doi.org/10.1016/j.cej.2012.06.038)
2. M. Greluk, Z. Hubicki, *Desalination* **278** (2011) 219 (https://doi.org/10.1016/j.desal.2011.05.024)
3. C. Ruiz, M. Vera, B. L. Rivas, S. Sánchez, B. F. Urbano, *RSC Adv*. **10** (2020) 43799 (https://doi.org/10.1039/D0RA08188D)
4. A. K. Hady, M. E. Owda, R. E. Abouzeid, H. A. Shehata, A. S. Elzaref, A. S. Elfeky, *Biomass Convers. Biorefinery* **15** (2025) 759 (https://doi.org/10.1007/s13399-023-05146-0)
5. R. Mohammad-Rezaei, B. Khalilzadeh, F. Rahimi, S. Moradi, M. Shahlaei, H. Derakhshankhah, M. Jaymand, *Environ. Res.* **214** (2022) 113966 (https://doi.org/10.1016/j.envres.2022.113966)
6. D. Ordonez, A. Valencia, B. Pereira, N.-B. Chang, *Environ. Res*. **212** (2022) 113208 (https://doi.org/10.1016/j.envres.2022.113208)
7. R. S. Dassanayake, S. Acharya, N. Abidi, *Molecules* **26** (2021) 4697 (https://doi.org/10.3390/molecules26154697)
8. X. Zhao, X. Wang, T. Lou, *J. Hazard. Mater*. **403** (2021) 124054 (https://doi.org/10.1016/j.jhazmat.2020.124054)
9. W. Liu, T. Lou, X. Wang, *Int. J. Biol. Macromol*. **242** (2023) 124711 (https://doi.org/10.1016/j.ijbiomac.2023.124711)
10. C. Miao, W. Huang, K. Li, Y. Yang, *Environ. Res*. **263** (2024) 120195 (https://doi.org/10.1016/j.envres.2024.120195)
11. B. Tomadoni, A. Ponce, M. Pereda, M. R. Ansorena, *Polym. Test*. **78** (2019) 105935 (https://doi.org/10.1016/j.polymertesting.2019.105935)
12. R. Resmi, S. Unnikrishnan, L. K. Krishnan, V. Kalliyana Krishnan, *J. Appl. Polym. Sci*. **134** (2017) (https://doi.org/10.1002/app.44529)
13. D. Mangla, A. Sharma, S. Ikram, *React. Funct. Polym*. **175** (2022) 105261 (https://doi.org/10.1016/j.reactfunctpolym.2022.105261)
14. R. A. Lusiana, N. B. A. Prasetya, K. Khabibi, *Indonesian J. Chem. Sci.* **9** (2020) 194 (https://journal.unnes.ac.id/sju/ijcs/article/view/41759/17209) (In Indonesian)
15. J. Yuan, Z.-Z. Pan, Y. Jin, Q. Qiu, C. Zhang, Y. Zhao, Y. Li, *J. Power Sources* **500** (2021) 229983 (https://doi.org/10.1016/j.jpowsour.2021.229983)
16. U. S. Malik, Q. Duan, M. B. K. Niazi, Z. Jahan, U. Liaqat, F. Sher, Y. Gan, H. Hou, *Chin. Chem. Lett*. **34** (2023) 108071 (https://doi.org/10.1016/j.cclet.2022.108071)
17. B. Farasati Far, M. R. Naimi-Jamal, M. Jahanbakhshi, S. A. Khalafvandi, M. Alian, D. Razeghi Jahromi, *J. Mol. Liq*. **395** (2024) 123839 (https://doi.org/10.1016/j.molliq.2023.123839)
18. N. Parshi, D. Pan, V. Dhavle, B. Jana, S. Maity, J. Ganguly, *Int. J. Biol. Macromol*. **141** (2019) 626–635 (https://doi.org/10.1016/j.ijbiomac.2019.09.025)
19. C. Ye, B. Yan, X. Ji, B. Liao, R. Gong, X. Pei, G. Liu, *Ecotoxicol. Environ. Saf*. **180** (2019) 366–373 (https://doi.org/10.1016/j.ecoenv.2019.04.086)
20. S. El Bourachdi, A. El Amri, A. R. Ayub, F. Moussaoui, Y. Rakcho, F. El Ouadrhiri, A. Adachi, M. Lechheb, J. A. Herrera-Melián, A. Lahkimi, *Int. J. Biol. Macromol*. **305** (2025) 141030 (https://doi.org/10.1016/j.ijbiomac.2025.141030)
21. G. Purwiandono, P. Lestari, *J. Ecol. Eng*. **24** (2023) 137 (https://doi.org/10.12911/22998993/166319)

22. L.-C. Juang, C.-C. Wang, C.-K. Lee, *Chemosphere* **64** (2006) 1920 (https://doi.org/10.1016/j.chemosphere.2006.01.024)
23. S. Jabbarvand Behrouz, A. Khataee, M. Safarpour, S. Arefi-Oskoui, S. Woo Joo, *Sep. Purif. Technol*. **269** (2021) 118720 (https://doi.org/10.1016/j.seppur.2021.118720)
24. S. Wang, H. Wang, S. Wang, L. Fu, L. Zhang, *Sep. Purif. Technol*. **307** (2023) 122783 (https://doi.org/10.1016/j.seppur.2022.122783)
25. H. Yu, Y. Ge, H. Ding, Y. Yan, L. Wang, Int. J. Biol. *Macromol*. **253** (2023) 126726 (https://doi.org/10.1016/j.ijbiomac.2023.126726)
26. S. J. Peighambardoust, S. Imani Zardkhaneh, M. Foroughi, R. Foroutan, H. Azimi, B. Ramavandi, *Environ. Res*. **258** (2024) 119428 (https://doi.org/10.1016/j.envres.2024.119428)
27. G. Michailidou, E. N. Koukaras, D. N. Bikiaris, *Int. J. Biol. Macromol*. **192** (2021) 1266 (https://doi.org/10.1016/j.ijbiomac.2021.10.093)
28. C. Xu, W. Zhan, X. Tang, F. Mo, L. Fu, B. Lin, *Polym. Test*. **66** (2018) 155 (https://doi.org/10.1016/j.polymertesting.2018.01.016)
29. R. L. C. G. da Silva, O. D. Bernardinelli, E. C. G. Frachini, H. Ulrich, E. Sabadini, D. F. S. Petri, *Carbohydr. Polym*. **292** (2022) 119725 (https://doi.org/10.1016/j.carbpol.2022.119725)
30. J. R. Westlake, M. Laabei, Y. Jiang, W. C. Yew, D. L. Smith, A. D. Burrows, M. Xie, *ACS Food Sci. Technol*. **3** (2023) 1680 (https://doi.org/10.1021/acsfoodscitech.3c00222)
31. Z. Zhang, J. Zhao, W. Li, H. Yuan, Y. Chi, J. Tang, J. Wang, Z. Xie, *J. Environ. Chem. Eng.* **13** (2025) 118743 (https://doi.org/10.1016/j.jece.2025.118743)
32. M. Carpintero, I. Marcet, C. Cortizo, P. Guerrero, K. de la Caba, M. Rendueles, M. Díaz, *Food Hydrocoll*. **171** (2026) 111838 (https://doi.org/10.1016/j.foodhyd.2025.111838)
33. Y. Peng, Y. Yu, Z. Su, Y. Zhong, S. Vijayakumar, Y. Chen, Y. Mao, M. Xin, M. Li, *Carbohydr. Polym*. **367** (2025) 124015 (https://doi.org/10.1016/j.carbpol.2025.124015)
34. Y. Yang, Y. Zhang, G. Wang, Z. Yang, J. Xian, Y. Yang, T. Li, Y. Pu, Y. Jia, Y. Li, Z. Cheng, S. Zhang, X. Xu, *J. Environ. Chem. Eng*. **9** (2021) 105407 (https://doi.org/10.1016/j.jece.2021.105407)
35. L. Chen, H.-H. Cheng, J. Xiong, Y.-T. Zhu, H.-P. Zhang, X. Xiong, Y.-M. Liu, J. Yu, Z.-X. Guo, *Chin. J. Polym. Sci*. **36** (2018) 1063 (https://doi.org/10.1007/s10118-018-2112-0)
36. H. Bakouri, A. Ziane, K. Guemra*, Int. J. Biol. Macromol*. **230** (2023) 123181 (https://doi.org/10.1016/j.ijbiomac.2023.123181)
37. F. Mashkoor, A. Nasar, C. Jeong, *Biomass Convers. Biorefinery* **14** (2024) 313 (https://doi.org/10.1007/s13399-021-02282-3)
38. S. Haider, S. Y. Park, S. H. Lee, *Soft Matter* **4** (2008) 485 (https://doi.org/10.1039/b713944f)
39. S. Amjadi, S. Emaminia, S. Heyat Davudian, S. Pourmohammad, H. Hamishehkar, L. Roufegarinejad, *Carbohydr. Polym*. **216** (2019) 376 (https://doi.org/10.1016/j.carbpol.2019.03.062)
40. J. Hu, Z. Wang, J. M. Miszuk, M. Zhu, T. I. Lansakara, A. V. Tivanski, J. A. Banas, H. Sun, *Carbohydr. Polym*. **271** (2021) 118440 (https://doi.org/10.1016/j.carbpol.2021.118440)
41. H. Mittal, A. Al Alili, P. P. Morajkar, S. M. Alhassan, *J. Mol. Liq*. **323** (2021) 115034 (https://doi.org/10.1016/j.molliq.2020.115034)

42. S. A. Ganiyu, M. A. Suleiman, W. A. Al-Amrani, A. K. Usman, S. A. Onaizi, *Sep. Purif. Technol*. **318** (2023) 123765 (https://doi.org/10.1016/j.seppur.2023.123765)
43. S. A. Bahadi, M. Iddrisu, M. K. Al-Sakkaf, M. A. A. Elgzoly, Q. A. Drmosh, W. A. Al-Amrani, U. Ahmed, U. Zahid, S. A. Onaizi, *Emergent Mater*. **7** (2024) 959 (https://doi.org/10.1007/s42247-023-00513-z)
44. H. Jayasantha Kumari, P. Krishnamoorthy, T. K. Arumugam, S. Radhakrishnan, D. Vasudevan, *Int. J. Biol. Macromol*. **96** (2017) 324 (https://doi.org/10.1016/j.ijbiomac.2016.11.077)
45. C. Zhou, S. Lee, K. Dooley, Q. Wu, *J. Hazard. Mater*. **263** (2013) 334 (https://doi.org/10.1016/j.jhazmat.2013.07.047)
46. G. Agbor Tabi, L. Ngouateu Rene Blaise, K. Daouda, A. Naphtali Odogu, A. Aime Victoire, N. Nsami Julius, K. Joseph Mbadcam, *Arab. J. Chem.* **15** (2022) 103515 (https://doi.org/10.1016/j.arabjc.2021.103515)
47. R. Ahmad, M. O. Ejaz, *Dyes Pigments* **216** (2023) 111305 (https://doi.org/10.1016/j.dyepig.2023.111305)
48. A. Salah Omer, G. A.El Naeem, A. I. Abd-Elhamid, O. O.M. Farahat, A. A. El-Bardan, H. M.A. Soliman, A. A. Nayl, *J. Mater. Res. Technol*. **19** (2022) 3241 (https://doi.org/10.1016/j.jmrt.2022.06.045)
49. L. Liu, Z. Y. Gao, X. P. Su, X. Chen, L. Jiang, J. M. Yao, *ACS Sustain. Chem. Eng*. **3** (2015) 432 (https://doi.org/10.1021/sc500848m).

Journal of the Serbian Chemical Society
JSCS-info@shd.org.rs • www.shd.org.rs/JSCS
J. Serb. Chem. Soc. 91 (5) 501–513 (2026)
JSCS–5505
Original scientific paper
Published 12 June, 2026

Adsorptive removal of Pb(II) from industrial effluent using nitric acid modified activated carbon: Optimization using Taguchi method

SAURABH MESHRAM[1]*, ANURADHA N. JOSHI[1], GAUTAM PRASAD DEWANGAN[1], CHANDRAKANT THAKUR[2] and ANUPAM B. SONI[2]

[1]*Department of Chemical Engineering, Guru Ghasidas Vishwavidyalaya, Bilaspur, 495009, Chhattisgarh, India* and [2]*Department of Chemical Engineering, National Institute of Technology Raipur, 492010, Chhattisgarh, India*

(Received 19 August, revised 22 October, accepted 25 December 2025)

Abstract: The study aimed to examine the use of nitric-acid-modified granular activated carbon to treat the wastewater of a lead-acid battery recycling unit for lead removal. The adsorbent was characterized using FTIR, SEM and XRD analyses. Surface functional groups, surface morphology and crystallinity were altered due to the modification. The batch adsorption study was conducted to evaluate the effects of adsorbent dose, initial pH, and contact time on adsorption performance for lead removal. Experiments were performed according to the Taguchi design of experiment method and factors were optimized based on SNR analysis to maximize the response. The ideal factor values were found to be pH 6, an adsorbent dose of 0.05 g, and a time of 240 min for the adsorption of lead onto the adsorbent, with an adsorbent uptake capacity of 9.93 mg g^{-1}. According to the ANOVA analysis, pH was found to be the most significant factor with an *F*-value of 28.07. Isotherm and kinetic studies were also carried out to understand the mechanism of adsorption. Adsorption was found to follow the Langmuir isotherm and the second order kinetic model.

Keywords: lead-acid battery; Taguchi optimization; adsorption; granular activated carbon; impregnation.

INTRODUCTION

Recycling of lead-acid batteries (LAB) is a crucial source of lead for storage battery production and also protects the environment. However, the recycling process generates wastewater with a pH of 1–1.5 and Pb concentrations ranging from 2 to 300 mg L^{-1}.[1] If this effluent is discharged untreated, it may adversely affect soil fertility and groundwater quality. If it enters the food chain, Pb may interfere with the functioning of major systems of the human body, such as the

* Corresponding author. E-mail: saurabhmeshram88@gmail.com
https://doi.org/10.2298/JSC250819003M

nervous system, digestive system, reproductive system, and urinary system by affecting major organs.[2] Conventionally, sodium carbonate is used to desulfurize and neutralize the effluent, separating the lead in the form of sludge.[3] According to a 2011 market survey report by the Mineral Economics Division, Indian Bureau of Mines, there were only 316 registered recyclers in India in 2010, including five in the Chhattisgarh state. However, many backyard smelters dispose of effluent without any treatment to increase profits. These smelters require an efficient and inexpensive technique to treat the effluent and keep the Pb(II) concentration in the discharge within safe limits (0.1 mg L^{-1}).

Various methods are available to remove Pb(II) from water, such as precipitation, membrane separation, ion exchange, electrocoagulation, filtration and adsorption.[4] Adsorption is a widely used technique due to its operational simplicity, cost-effectiveness and low capital cost. Activated carbon is often used in water treatment processes due to its different chemical characteristics, porous structure, and high surface area.[5] Activated carbon is available in both powder (PAC) and granular (GAC) forms, with PAC having larger pores and GAC having smaller internal pores and a lower adsorption rate than PAC. GAC is preferred over PAC due to its ease of handling and disposal and reduced losses during operation.[6] Several investigations have utilized GAC to treat wastewater, including removing lead from aqueous solutions by Dwivedi *et al.*, removing copper, zinc and lead ions by Chen and Wang, removing amoxicillin from water by Franco *et al.*, removing phenol from synthetic water by Sulaymon *et al.* and removing cadmium and lead by Jusoh *et al.*[6–10]

Activated carbon is a widely used adsorbent for water treatment because of its porous structure, abundant active sites, functional groups, and high surface area. However, its adsorption capacity is limited, and researchers have modified it using chemical agents to enhance its efficiency by promoting chemisorption of pollutants on the surface. Wang *et al.* modified GAC with magnesium, resulting in an increased adsorption capacity from 3.47 to 8.08 mg g^{-1} for the adsorption of Cd(II).[11] Fan and Anderson used the manganese oxide for the removal of Cu(II) and Cd(II), and Yao *et al.* modified activated carbon derived from rice husk using nitric acid, which increased its uptake capacity by improving the surface characteristics and porous structure.[12,13] In another study, Jiang *et al.* found that modifying activated carbon with HNO_3 as an impregnating agent after oxidizing it using concentrated sulfuric acid increased the mesoporous volume, specific surface area, and uptake capacity for the separation of dibenzothiophene and methylene blue.[14]

The modification of activated carbon with nitric acid has been widely; however, this study investigates the effect of modification on granular activated carbon. HNO_3-modified GAC was used for the first as an adsorbent for the treatment of LAB recycling unit effluent. The characteristics of GAC and HNGAC were analyzed using SEM, FTIR and XRD to determine the effect of modification. The

adsorption experiments were conducted based on a Taguchi orthogonal L16 array (4^3) with four levels of the parameters: adsorbent dose, retention time and pH. The parameters were optimized using the signal-to-noise ratio (*SNR*) obtained from Taguchi analysis.

EXPERIMENTAL

Wastewater

The wastewater of a lead-acid battery (LAB) recycling plant was obtained from a smelter in Raipur, Chhattisgarh, India. The pH of the effluent was 1.2, and the concentration of Pb(II) was 11.2 mg L^{-1}. Prior to the batch adsorption study, the pH of the wastewater was adjusted using standard solutions of sodium hydroxide and hydrochloric acid.

Adsorbent

Granular activated carbon (GAC) was commercially procured and improved using nitric acid following the process described by El-Wakil *et al.*[15] To prepare the modified GAC, a mixture of HNO_3 and distilled water in a 1:1 ratio was heated to 110 °C. Then, 1 g of GAC was added to 5 mL of the heated solution and heated for 3 h. The resulting solution was filtered, and the solid fraction was collected and washed with distilled water until the pH reached 6. Finally, the nitric-acid-modified GAC (HNGAC) was dried for 24 h at 100 °C in a hot air oven.

Characterization

The surface functional groups of the adsorbents were analyzed using FTIR (Bruker, Alpha Model) within the 4000–400 cm^{-1} range. The Zeiss EVO Series scanning electron microscope (SEM) was used to obtain surface micrographs and elemental composition of the adsorbents before and after the nitric acid modification. A PANalytical multifunctional XRD analyzer was used to obtain XRD spectra to determine the surface nature of the adsorbents. Standard ASTM methods were followed for proximate analysis.

Batch adsorption and optimization

A three factor, four level Taguchi L16 orthogonal array was obtained using Minitab 18.0 to perform the experiments. The three factors were initial pH of the wastewater (1.5, 3, 4.5, 6), dose (0.1, 0.4, 0.7, 1.0 g $(50\ mL)^{-1}$) and contact time (30, 60, 90, 240 min, Table I). For batch adsorption, a fixed amount of HNGAC was added to 250 ml of wastewater in an Erlenmeyer flask and kept in an orbital shaker for a defined time at 30 °C and 100 rpm. The Pb(II) concentration of the filtered effluent was analyzed using an atomic absorbance spectroscope (ECIL, India). Experimental runs were performed in duplicate and average values were reported. Eqs. (1) and (2) were used to determine the removal of Pb(II) and the uptake capacity of the adsorbent, respectively:

$$\text{Removal of Pb(II)} = 100\frac{c_0 - c_e}{c_0} \tag{1}$$

$$q_e = \frac{c_0 - c_e}{m}V \tag{2}$$

where c_0 and c_e are the initial and final concentration of Pb(II) in the effluent, respectively. V is the volume of effluent and m is the mass of adsorbent.

Taguchi analysis, which uses a signal-to-noise ratio (*SNR*), was used to optimize the parameters and determine the optimal levels and their contribution to achieving the desired response.[16] *SNR* analysis utilizes three response characteristic functions based on the minimization,

maximization and nominalization of the responses.[17] In this study, a larger-the-better characteristic function was used for *SNR* analysis since the goal was to recover Pb(II), as represented:

$$\left(\frac{S}{N}\right)_{\text{Larger is better}} = -10\log\left(\frac{1}{n}\sum_{i=1}^{n}\frac{1}{y_i^2}\right) \quad (3)$$

where y_i is the response and n is the number of experiments performed. The response factors were optimized using Minitab version 18.1. The significance and effect levels of the various factors in the batch adsorption study were determined using ANOVA analysis.

TABLE I. Batch adsorption parameters and their levels

Factor	Name	Level 1	Level 2	Level 3	Level 4
P	pH	1.5	3.0	4.5	6.0
D	Dose, g (50 mL)$^{-1}$	0.1	0.4	0.7	1.0
T	Time, min	30	60	90	240

RESULTS AND DISCUSSION

Characterization

Fig. 1 shows a comparison of the FTIR spectra of GAC and HNGAC. After modification, the intensity of the surface functional group O–H, which corresponds to the peak at 3441 cm^{-1} in GAC, increased and is represented by the peak at 3448 cm^{-1} in HNGAC. The signal at 2926 cm^{-1} in GAC indicates the presence of weakly bonded methyl and methylene groups (vibrational C–H bond). These C–H groups were oxidized and vanished from the HNGAC spectra following modification. It is evident that following modification, the peak at about 1630 cm^{-1} in GAC, which is attributed to C=O groups, became noticeably more intense in HNGAC. The small peak in both spectra at around 1400 cm^{-1} could be due to the presence of $-CH_2$ and $-CH_3$ groups. The peaks in the 1000–1200 cm^{-1} region can be attributed to C–O stretching and O–H bending vibrations of ether, lactonic and phenol. The peak in the HNGAC spectrum at 607.50 cm^{-1} may be due to newly formed surface groups of oxygen and nitrogen-containing groups.[18–21]

In Fig. 2, SEM micrographs of GAC and HNGAC are presented. GAC has an irregular porous structure and a rough surface. Acid treatment with nitric acid decreased the internal micropores of GAC and removed impurities from its surface. Because nitric acid is a potent oxidant, the acid treatment created canal-like mesopores on the surface, which reduced the pore volume and surface area.[22,23] The impregnation of nitric acid reduced the microporous pore volume and specific surface area of the activated carbon, as found by Jiang *et al.*[24] EDS elemental analysis showed that impurities from GAC were removed and oxygen-containing groups increased after acid treatment. Moreover, HNGAC was found to contain nitrogen, indicating that nitrogen-containing groups were formed on the surface after modification.

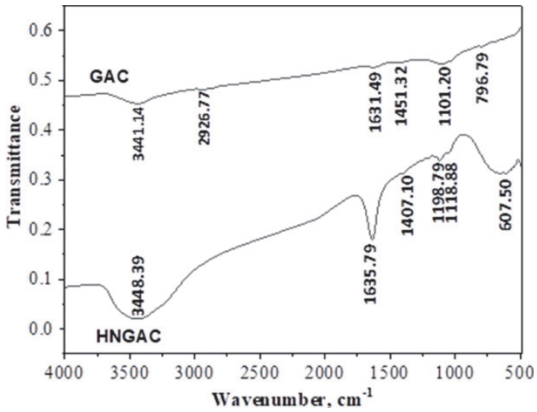

Fig. 1. FTIR spectra of GAC and HNGAC in the wavenumber range of 500–4000 cm^{-1}.

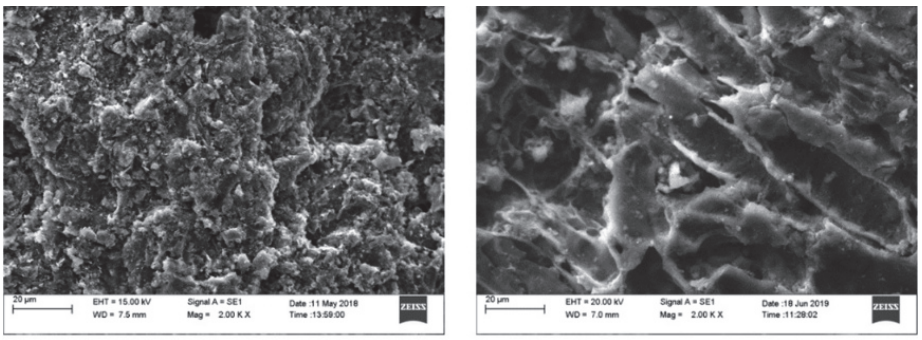

a) b)

Fig. 2. Surface morphology images of: a) GAC and b) HNGAC obtained by SEM.

The crystalline or amorphous character of GAC and HNGAC was determined using the XRD spectra shown in Fig. 3. The peaks at 2θ 26 and 42° correspond to the (002) and (100) diffraction planes, respectively, and signify the amorphous

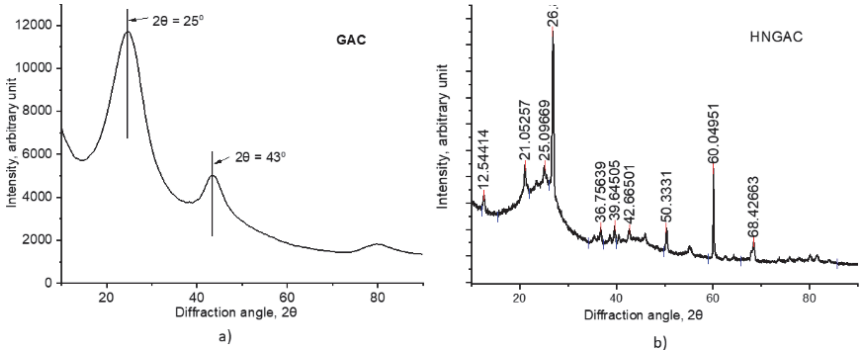

a) b)

Fig. 3. XRD spectra of: a) GAC and b) HNGAC at 2θ values between 0 and 90°.

nature of activated carbon. The diffraction pattern of HNGAC exhibited several diffraction peaks, showing an increase in crystallinity due to modification. Similar effects of HNO_3 modification on adsorbent prepared from olive tree prune waste were observed by Calero *et al.*[25]

Taguchi optimization

Three parameters at four different levels were used in the batch adsorption study using the Taguchi L16 orthogonal array. Table II displays the results for each run's adsorbent capacity and Fig. 4 displays the mean signal-to-noise ratio (*SNR*) plot for every variable associated with HNGAC's uptake capacity. It was found that while the *SNR* value decreased with increasing dose, it increased with increasing pH and time. At *P*4-*D*1-*T*4, the mean *SNR* value was highest. The optimal factor values were found to be pH 6, an adsorbent dose of 0.05 g, and a contact time of 240 min, based on the maximization feature of *SNR*. Nonetheless, there was little difference in uptake capacity for pH values of 4.5 and 6, so a pH value of 4.5 could be selected from an economic perspective for both adsorbents. The *SNR* analysis revealed that pH was the most influential factor in the adsorption of lead onto HNGAC.

TABLE II. Taguchi experimental runs for adsorption of lead onto HNGAC and the response variable (adsorbent uptake capacity)

Exp. No.	*P* (pH)	*D* (Dose, g)	*T* (Time, min)	q_e / mg g^{-1}
1	*P*1	*D*1	*T*1	0.12
2	*P*1	*D*2	*T*2	0.21
3	*P*1	*D*3	*T*3	0.20
4	*P*1	*D*4	*T*4	0.21
5	*P*2	*D*1	*T*2	2.38
6	*P*2	*D*2	*T*1	1.31
7	*P*2	*D*3	*T*4	0.95
8	*P*2	*D*4	*T*3	0.77
9	*P*3	*D*1	*T*3	9.43
10	*P*3	*D*2	*T*4	5.74
11	*P*3	*D*3	*T*1	3.18
12	*P*3	*D*4	*T*2	2.92
13	*P*4	*D*1	*T*4	**9.93**
14	*P*4	*D*2	*T*3	5.92
15	*P*4	*D*3	*T*2	3.96
16	*P*4	*D*4	*T*1	2.54

To determine the significance level of the factors on the adsorbent uptake capacity, an analysis of variance (ANOVA) was carried out and is presented in Table III. As observed, the coefficient of determination (R^2) was found to be 95.71, which signifies that the ANOVA model fitted well to the data. The ratio of variance between samples to variance within samples is termed the *F*-value and it indicates

the parameters which affect the response largely. The initial pH of the effluent was found to have the highest significance on the adsorption of lead onto HNGAC with an *F*-value of 28.07, whereas the least significant factor was adsorbent dose with an *F*-value of 0.007.

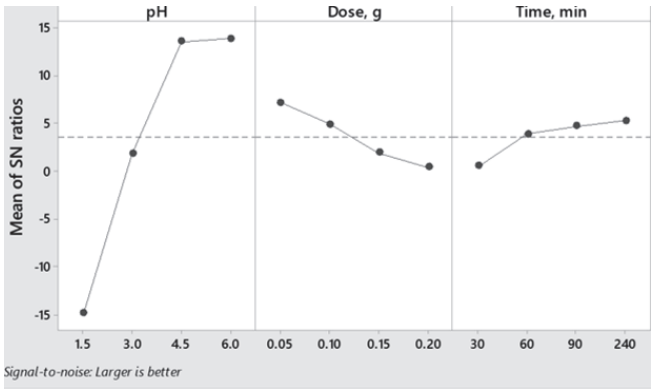

Fig. 4. Signal to noise ratio plot for the uptake capacity of HNGAC for pH, dose and time at different levels.

TABLE III. ANOVA analysis for adsorption of lead onto HNGAC

Source	*DF*	*SS*	*MS*	*F*-Value	*P*-Value
pH	3	90.629	30.210	28.07	0.001
Dose, g	3	35.563	11.854	11.01	0.007
Time, min	3	17.743	5.914	5.50	0.037
Error	6	6.457	1.076		
Total	15	150.393			
	R^2	R^2(adj)			
	95.71 %	89.27 %			

Effect of each factor

The effect of pH on the adsorption of Pb(II) by HNGAC is shown in Fig. 5. The pH of the effluent has a significant impact on the adsorption process, affecting the charge on the surface and the ionization of Pb(II) in the effluent. To investigate this, the pH was varied from 1.5 to 6, as Pb(II) tends to precipitate at alkaline pH values.[26] At low pH values, Pb(II) and H^+ compete for adsorption onto HNGAC and consequently result in slow adsorption. Increasing the initial pH of the effluent led to an increase in the uptake capacity of HNGAC, as the competition between hydrogen and lead ions for adsorption sites decreased. Pb(II) ions were then able to bond with functional groups like –OH and –COOH present on the adsorbent surface.[26,27] Moreover, at high pH, the negative charge on the surface increased, as protons are removed from the functional groups present on the surface, which results in enhanced electrostatic attraction for Pb(II), thereby improving adsorption.[28]

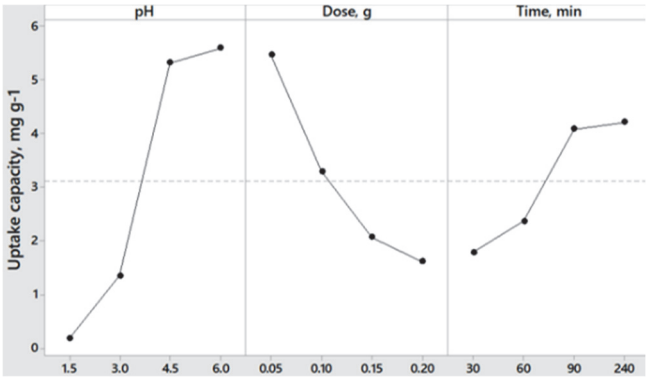

Fig. 5. Effect of initial pH, adsorbent dose and contact time on adsorption performance of HNGAC for the removal of Pb(II).

According to the results presented in Fig. 5, an increase in adsorbent dose led to a decrease in the uptake capacity of Pb(II). The reason behind this trend may be the existence of either unsaturated adsorption sites or overlapping and aggregation of adsorption sites due to maximum adsorption being reached at a certain dose of adsorbent.[29]

The effect of contact time on Pb(II) uptake capacity was investigated, and as shown in Fig. 5, the uptake increased up to 90 min, after which it reached a plateau. This trend could be attributed to the initial availability of more than enough active sites for the adsorption of Pb(II), which became occupied over time, resulting in effective utilization of the adsorbent. As the number of active sites decreased with time, the competition between the lead ions in the effluent and the adsorbent surface for the remaining adsorption sites slowed down the adsorption process.

Fig. 6 displays response surface plots that illustrate the impact of two factors on the adsorption. Fig. 6a indicates that, to achieve optimal adsorbent capacity, adsorbent dose should be less than 0.1 g (50 mL)$^{-1}$, and the pH should exceed 4. This suggests that competition between Pb(II) and H^+ decreased at higher pH and that complete saturation of adsorption sites occurred at lower adsorbent doses. It can be found from Fig. 6b that higher adsorbent capacity is obtained at pH > 4.5 and time > 80 min. This implies that insufficient interaction between the lead ions and adsorbent sites prevented high absorption capacity from being reached at the start of adsorption, even at high pH. High lead uptake capacity of HNGAC was achieved at doses <0.1 g/(50 mL) and time > 90 min as can be observed in Fig. 6c.

Isotherm study

The fitting graphs for the Langmuir and Freundlich models fitted to the experimental data for Pb(II) adsorption onto HNGAC are shown in Fig. 7. Table IV displays the parameters of the isotherm models obtained from fitting the experimental data. The correlation coefficient (R^2) of the Langmuir model is higher than

that of the Freundlich model. This shows that the adsorption equilibrium data fit the Langmuir equation and the adsorption involves monolayer adsorption. The maximum monolayer adsorption capacity obtained from the Langmuir model is 9.93 mg g^{-1} for HNGAC.

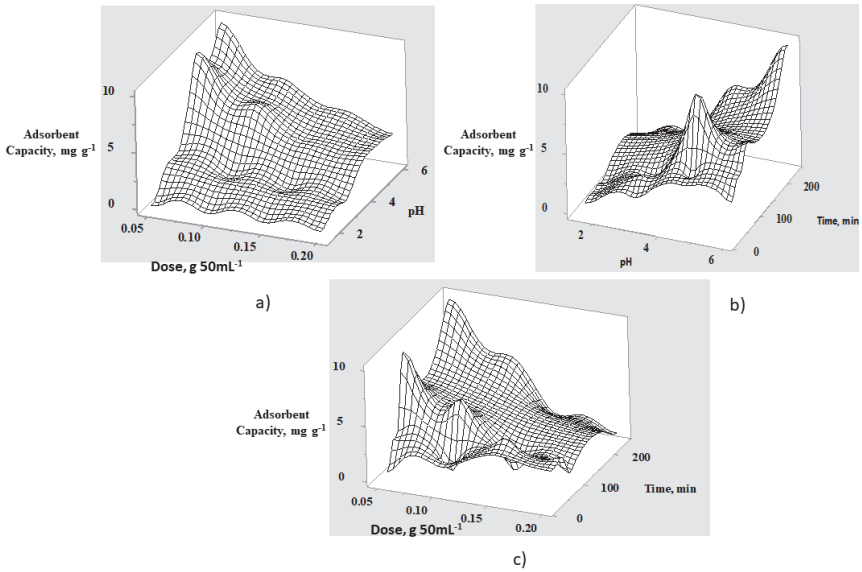

Fig. 6. Plots of simultaneous effect of two factors on lead adsorption onto HNGAC: a) initial pH and dose, b) time and pH and c) time and dose.

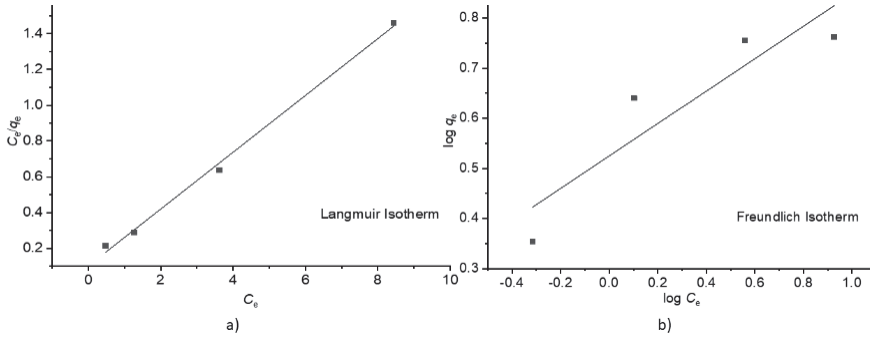

Fig. 7. Isotherm plots for Pb(II) adsorption onto HNGAC: a) Langmuir isotherm and b) Freundlich isotherm (pH 4.5; time 60 min; speed 100 rpm; volume 50 mL; temperature 30 °C; dose 2 g L^{-1}).

TABLE IV. Parameters of the isotherm models for Pb(II) adsorption onto HNGAC.

Langmuir			Freundlich		
q_m / mg g^{-1}	K_L / L mg^{-1}	R^2	$1/n$	K_F / mg g^{-1} ((mg L^{-1})$^{1/n}$)$^{-1}$	R^2
9.90099	0.639240506	0.99	0.323	1.688769234	0.836

Kinetic study

Both pseudo-first-order and pseudo-second-order kinetic models were used to assess the adsorption of Pb(II) onto HNGAC. Fig. 8 displays the kinetic plots, while Table V provides the correlation coefficient and kinetic model parameters. Because of its higher correlation coefficient of 0.99, the pseudo-second-order kinetic model better describes the adsorption kinetics than the pseudo-first-order. This implies that chemisorption may play a dominant role in the adsorption process. Compared to the pseudo-first-order model, the value of q_e derived from the pseudo-second-order model agrees better with the experimentally determined q_e value. Abbaszadeh *et al.* observed similar outcomes for the adsorption of Pb(II) on activated carbon from papaya peel biowaste.[26] They found a measured uptake capacity of 38.31 mg g^{-1} and a calculated uptake capacity of 42.55 mg g^{-1} from the pseudo-second-order kinetics.

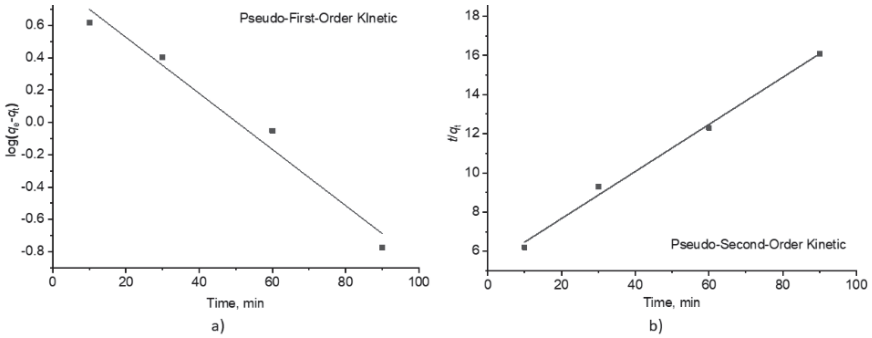

Fig. 8. Kinetic study graph for lead adsorption onto HNGAC: a) pseudo-first-order model and b) pseudo-second-order model (initial pH 4.5; adsorbent dose, 0.1 g (50 mL)$^{-1}$; Pb(II) concentration, 10.2 mg L^{-1}).

TABLE V. Kinetic model parameters for Pb(II) adsorption onto HNGAC for the PFO and PSO models.

PFO			PSO		
K_1 / h^{-1}	q_e	R^2	K_2 / g mg^{-1} h^{-1}	q_e	R^2
0.039151	2.394082	0.973	0.002738684	8.333333	0.994

Mechanism of adsorption

The adsorption of Pb(II) onto the adsorbents involves physical and chemical interactions with the surface functional groups. The adsorption of Pb(II) may be caused by ion exchange interactions with surface groups like hydroxyl and carboxyl. The FTIR analysis revealed that the intensity of these groups, especially –OH and –COOH, was higher in HNGAC compared to GAC, which supports the ion exchange between adsorbent and adsorbate. It was also observed that the amount of Pb(II) uptake by HNGAC was significantly higher than that of GAC, indicating that

chemisorption played a major role in the adsorption process rather than physisorption. Impregnation of GAC with HNO_3 considerably increased the negative surface charge of the adsorbent, which attracted the lead ions.

CONCLUSION

Pb(II) was separated from the effluent of a LAB recycling unit utilizing HNGAC as an adsorbent. The intensity of the –OH and –COOH functional groups present on the surface of GAC was found to increase after modification using nitric acid, moreover some new nitrogen-containing functional groups were formed after modification. Modification led to an increase in mesopores and a decrease in micropores. The optimum combination of parameters found using Taguchi analysis was: a time of 240 min, pH 6 and an adsorbent dose of 0.05 g (50 mL)$^{-1}$. The maximum adsorption capacity of GAC increased due to modification from 7.69 to 9.93 mg g^{-1}. From the isotherm and kinetic studies, it can be inferred that adsorption of lead onto HNGAC follows the Langmuir isotherm and pseudo-second-order kinetics. Adsorption of lead onto HNGAC include monolayer adsorption followed by chemical interaction with functional groups available on the adsorbent surface. Overall, it could be established that, adsorption can be used as an effective technique for the remediation of lead from the wastewater of a lead-acid battery recycling unit and HNGAC could be used as an efficient adsorbent.

Acknowledgements. The authors want to acknowledge the support and facilities provided by National Institute of Technology Raipur, India. The author also wants to acknowledge the Guru Ghasidas University Bilaspur, India, for granting the study leave to do Ph.D.

ИЗВОД

АДСОРПЦИОНО УКЛАЊАЊЕ Pb(II) ИЗ ИНДУСТРИЈСКОГ ЕФЛУЕНТА ПРИМЕНОМ АКТИВНОГ УГЉА МОДИФИКОВАНОГ АЗОТНОМ КИСЕЛИНОМ: ОПТИМИЗАЦИЈА ПРИМЕНОМ ТАГУЧИ МЕТОДЕ

SAURABH MESHRAM[1], ANURADHA N JOSHI[1], GAUTAM PRASAD DEWANGAN[1], CHANDRAKANT THAKUR[2] и ANUPAM B. SONI[2]

[1]*Department of Chemical Engineering, Guru Ghasidas Vishwavidyalaya, Bilaspur, 495009, Chhattisgarh, India u* [2]*Department of Chemical Engineering, National Institute of Technology Raipur, 492010, Chhattisgarh, India*

Циљ ове студије био је испитивање примене гранулисаног активног угља модификованог азотном киселином за третман отпадних вода из постројења за рециклажу оловно-киселинских акумулатора, ради уклањања олова. Адсорбенс је окарактерисан применом FTIR, SEM i XRD анализа. Модификацијом су промењене површинске функционалне групе, површинска морфологија и кристалиничност. Шаржна адсорпциона испитивања спроведена су ради процене утицаја дозе адсорбенса, почетне pH вредности и контактног времена на ефикасност адсорпције уклањања олова. Експерименти су изведени у складу са Тагучи методом дизајна експеримената, а фактори су оптимизовани на основу анализе односа сигнал/шум (*SNR*) у циљу максимизације одзива. Оптималне вредности фактора утврђене су као pH 6, доза адсорбенса од 0,05 g и време од 240 min за адсорпцију олова на адсорбенс, при чему је адсорпциони капацитет износио 9,93 mg g^{-1}.

На основу ANOVA анализе, pH је идентификован као најзначајнији фактор, са *F*-вредношћу од 28,07. Изотермска и кинетичка испитивања такође су спроведена ради разумевања механизма адсорпције. Утврђено је да адсорпција прати Лангмуирову изотерму и кинетички модел другог реда.

(Примљено 19. августа, ревидирано 22. октобра, прихваћено 25. децембра 2025)

REFERENCES

1. S. Meshram, R. S. Thakur, G. Jyoti, C. Thakur, A. B. Soni, *J. Indian Chem. Soc.* **99** (2022) 100469 (https://doi.org/10.1016/j.jics.2022.100469)
2. M. Caccin, M. Giorgi, F. Giacobbo, M. D. Ros, L. Besozzi, M. Mariani, *Desalin. Water Treat.* **57** (2016) 4557 (https://doi.org/10.1080/19443994.2014.992974)
3. S. Meshram, C. Thakur, A. B. Soni, *J. Serb. Chem. Soc.* **85** (2020) 953 (https://doi.org/10.2298/JSC191103015M)
4. S. Meshram, S. Dharmadhikari, R. S. Thakur, C. Thakur, A. B. Soni, *J. Hazard. Mater. Adv.* **10** (2023) 10297 (https://doi.org/10.1016/j.hazadv.2023.100297)
5. C. Thakur, I. D. Mall, V. C. Srivastava, *Theor. Found. Chem. Eng.* **48** (2014) 60 (https://doi.org/10.1134/S004057951401014X)
6. C. P. Dwivedi, J. N. Sahu, C. R. Mohanty, B. R. Mohan, B. C. Meikap, *J. Hazard. Mater.* **156** (2008) 596 (https://doi.org/10.1016/j.jhazmat.2007.12.097)
7. J. P. Chen, X. Wang, *Sep. Purif. Technol.* **19** (2000) 157 (https://doi.org/10.1016/S1383-5866(99)00069-6)
8. M. A. E. Franco, C. B. Carvalho, M. M. Bonetto, R. P. Soares, L. A. Féris, *J. Clean. Prod.* **161** (2017) 947 (https://doi.org/10.1016/j.jclepro.2017.05.197)
9. A. H. Sulaymon, D. W. Abood, A. H. Ali, *Hydrol. Curr. Res.* **2** (2011) 1000120 (http://dx.doi.org/10.4172/2157-7587.1000120)
10. A. Jusoh, L. S. Shiung, N. Ali, M. J. M. M. Noor, *Desalin.* **206** (2007) 9 (https://doi.org/10.1016/j.desal.2006.04.048)
11. K. Wang, J. Zhao, H. Li, X. Zhang, H. Shi, *J. Taiwan Inst. Chem. Eng.* **61** (2016) 287 (https://doi.org/10.1016/j.jtice.2016.01.006)
12. H. J. Fan, P. R. Anderson, *Sep. Purif. Technol.* **45** (2005) 61 (https://doi.org/10.1016/j.seppur.2005.02.009)
13. S. Yao, J. Zhang, D. Shen, R. Xiao, S. Gu, M. Zhao, J. Liang, *J. Colloid Interface Sci.* **463** (2016) 118 (https://doi.org/10.1016/j.jcis.2015.10.047)
14. Z. Jiang, Y. Liu, X. Sun, F. Tian, F. Sun, C. Liang, W. You, C. Han, C. Li, *Langmuir* **19** (2003) 731 (https://doi.org/10.1021/la020670d.)
15. A. M. El-Wakil, W. M. Abou El-Maaty, F. S. Awad, *J. Anal. Bioanal. Tech*. **5** (2014) 1000187 (https://doi.org/10.4172/2155-9872.1000187)
16. M. Nandhini, B. Suchithra, R. Saravanathamizhan, D. G. Prakash, *J. Electrochem. Sci. Eng.* **4** (2014) 227 (https://doi.org/10.5599/jese.2014.0056)
17. S. Meshram, C. Thakur, A. B. Soni, *Pollution* **6** (2020) 879 (https://doi.org/10.22059/poll.2020.302442.808)
18. M. A. Ramos, V. G. Serrano, C. V. Calahorro, A. J. L. Peinado, *Spectrosc. Lett.* **26** (1993) 1117 (https://doi.org/10.1080/00387019308011598)
19. V. G. Serrano, M. A. Ramos, A. J. L. Peinado, C. V. Calahorrro, *Thermochim. Acta* **291** (1997) 109 (https://doi.org/10.1016/S0040-6031(96)03098-5)

20. V. C. Srivastava, I. D. Mall, I. M. Mishra, *J. Hazard. Mater.* **134** (2006) 257 (https://doi.org/10.1016/j.jhazmat.2005.11.052)
21. T. S. Anirudhan, S. S. Sreekumari, *J. Environ. Sci.* **23** (2011) 1989 (https://doi.org/10.1016/S1001-0742(10)60515-3)
22. N. A. Kolur, S. Sharifian, T. Kaghazchi, *Turkish J. Chem.* **43** (2019) 663 (https://doi.org/10.3906/kim-1810-63)
23. M. Dutta, S. Mishra, M. Kaushik, J. K. Basu, *Res. J. Environ. Sci.* **5** (2011) 741 (https://doi.org/10.3923/rjes.2011.741.751)
24. X. Jiang, X. Lan, Y. Song, X. Xing, H. M. A. Hassan, *J. Chem.* (2019) 8593742 (https://doi.org/10.1155/2019/8593742)
25. M. Calero, A. Pérez, G. Blázquez, A. Ronda, M. A. M. Lara, *Ecol. Eng.* **58** (2013) 344 (https://doi.org/10.1016/j.ecoleng.2013.07.012)
26. S. Abbaszadeh, S. R. W. Alwi, C. Webb, N. Ghasemi, I. I. Muhamad, *J. Clean. Prod.* **118** (2016) 210 (https://doi.org/10.1016/j.jclepro.2016.01.054)
27. Z. Guo, J. Zhang, Y. Kang, H. Liu, *Ecotoxicol. Environ. Saf.* **145** (2017) 442 (https://doi.org/10.1016/j.ecoenv.2017.07.061)
28. Y. Li, Q. Du, X. Wang, P. Zhang, D. Wang, Z. Wang, Y. Xia, *J. Hazard. Mater.* **183** (2010) 583 (https://doi.org/10.1016/j.jhazmat.2010.07.063)
29. S. Meshram, C. Thakur, A. B. Soni, *Indian Chem. Eng.* **63** (2020) 460 (https://doi.org/10.1080/00194506.2020.1795933).

Journal of the Serbian Chemical Society
JSCS-info@shd.org.rs • www.shd.org.rs/JSCS
J. Serb. Chem. Soc. 91 (5) 515–527 (2026)
JSCS–5506
Original scientific paper
Published 12 June, 2026

Investigation of morphological and mechanical properties of hardened and tempered AISI 4340 steel

SUBHAN ALI[1]*, ABDUL QADEER LAGHARI[2]**, ARSHAD IQBAL[3], GHULAM MUSTAFA MEMON[4], IFITKHAR AHMED MEMON[1], FIDA HUSSAIN CHANNA[5], ABDUL SAMI CHANNA[6], MASROOR ABRO[2], KHAN MUHAMMAD[3] and SHOUKAT ALI NOONARI[7]

[1]Materials Engineering Department, Dawood University of Engineering and Technology, Karachi, 74800, Sindh, Pakistan, [2]Chemical Engineering Department, Mehran University of Engineering and Technology, Jamshoro,76080, Pakistan, [3]Chemical Engineering Department,, Dawood University of Engineering and Technology, Karachi, 74800, Sindh, Pakistan, [4]IRC for Industrial Nuclear Energy, King Fahd University of Petroleum & Minerals, Saudi Arabia, [5]Mining Engineering Department, Mehran University of Engineering and Technology, Jamshoro,76080, Pakistan, [6]Chemical Engineering Department, Qaid-e-Awam University of Engineering and Technology, Nawabshah, 74800, Pakistan and [7]Department of Mechanical Engineering, Isra University, Hyderabad, Sindh, Pakistan

(Received 23 November, revised 26 December 2025, accepted 9 March 2026)

Abstract: AISI 4340 steel is widely used in risk-intensive industries due to its excellent mechanical strength and impact resistance. The mechanical properties of AISI 4340 steel can be significantly enhanced through heat treatment, particularly tempering at controlled temperatures. This study investigates the effect of tempering on the microstructure and mechanical properties of AISI 4340 steel. The experimental analysis includes characterization before and after heat treatment to assess changes in strength, toughness and ductility. The results demonstrate that tempering at 450 °C for 45 min provides the optimum balance of impact energy and ductility while slightly reducing hardness and strength. Conversely, tempering at 550 °C results in a more pronounced increase in impact energy and ductility, but at the cost of a greater reduction in hardness and strength. Microstructural examination confirms the formation of tempered martensite, contributing to the observed mechanical behaviour. The findings provide valuable insights into optimizing heat treatment parameters for AISI 4340 steel to achieve a balanced combination of strength, toughness, and ductility for industrial applications.

Keywords: AISI 4340 steel; tempering; mechanical properties; heat treatment.

*,** Corresponding authors. E-mail: (*)subhan.jogi@duet.edu.pk, (**)abdul.qadeer@admin.muet.edu.pk
https://doi.org/10.2298/JSC251123012A

INTRODUCTION

Low alloy AISI 4340 steel has found application in the military sector, critical aircraft components, and nuclear power plants, attributable to its mechanical properties such as tensile strength, stiffness, exceptional processability, optimal hardness and improved weldment.[1,2] Nickel in steel, compared to that in other medium and low alloy steels, enhances tensile toughness and hardness.[3] It has been reported that high-strength steels used in industries suffer from unexpected brittle failure.[4] The catastrophic failure of engineering components under service conditions, shutdown of power plants, and elevated impairment costs of engineering machine components are serious consequences during operation.[5,6] Dual-phase steel structures produced by various means have been planned nowadays for the proud performance of structural steel.[7] Reported work clarified the effect of quenching and tempering treatments for optimising properties of AISI 4340 steel.[8] Additionally, quenching and tempering treatments significantly increase the ultimate tensile strength of the steel.[9] Published work rectified that quenching and tempering heat treatment can be used to develop the tempered martensitic steel.[10] Moreover, the hardening treatment of AISI 4340 steel substantially increases the toughness and minimised brittle fracture.[11,12] Furthermore, recommendations regarding the toughness and strength of AISI 4340 steel indicate that the heat treatments for homogenization, normalizing, quenching and tempering, inter-critical annealing, austempering and martempering may be required.[13] Subsequently, it was demanded that the upgrading of mechanical properties of AISI 4340 steel by numerous heat treatments procedures and by controlled metal-forming processes.[14] Likewise, an inter-critical quenching process was applied to produce austenite phase for TRIP steel.[15] Nevertheless, difficulties in metal forming processes and high operating equipment costs in process industries. In alternative, it was conveyed that a substantial alteration in the mechanical properties of steel is achieved by intermediate quenching treatment.[16] For the advancement of AISI 4340 steel is used in quench and temper form, though, it is susceptible to embrittlement when tempered at temperatures ranging from 300 to 400 °C.[17] The embrittlement problems addressed by many researchers in their findings that changes in micrographs and mechanical properties at diverse tempering temperatures.[18] Temper heat treatment can be used as a stress relief procedure, confirming reduction of tensile residual stresses, which have badly influence on fatigue life of components.[19] Despite widespread usage in industries of AISI 4340 steel and detailed study of the mechanical performance of the material, there is little published work in literature about the effect of heat treatment parameters on residual stresses.[20] The objective of the present work is to optimise mechanical properties of steel AISI 4340 through hardening treatment. The hardening method improves the strength and stiffness of materials by treating them at a specified temperature followed by quenching in water and oil medium.[21]

Temper treatment practice in ferrous materials is useful after hardening.[22] In tempering procedure, steel is subjected to heating and cooling below the transformation temperature range and takes time for cooling at a suitable rate.[23] Tempering treatment causes of reduction in hardness and increases the toughness to get the desired mechanical properties.[24,25] Hence, in current study, AISI 4340 high strength low alloy steel has been designated and treated at suitable temperature to stabilize the microstructure for optimisation of mechanical properties. AISI 4340 steel applied in machine components, but it is required for service conditions in various forms extending from aircraft structures to automotive crankshafts, where diverse characteristics are required.[26] In this study, hardening and tempering techniques are employed to alter the mechanical properties and microstructure of AISI 4340 high strength low alloy steel through heat treatment. In addition, outcomes of this research were compared with conventional hardening and tempering of steel. Conclusively, the optimal conditions for attaining the highest toughness were achieved.

EXPERIMENTAL PROCEDURE

Material

Work material for the heat-treatment procedure was made by partitioning AISI 4340 steel bar into cross-sectional areas of 0.621 m^2 and 0.914 m length. The material in the form of a billet is rolled into a round bar and then cooled in air during the manufacturing procedure of AISI 4340 steel in an industrial unit (Fig. 1).

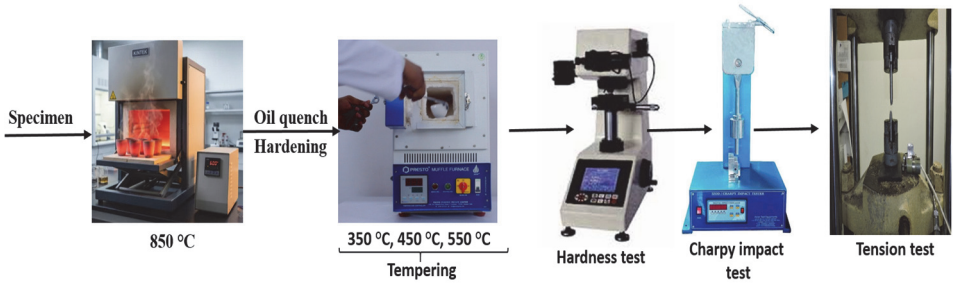

Fig. 1. Experimental setup of AISI 4340 steel bar.

Chemical configuration

The surface of the specimen was prepared by grinding followed by polishing to eliminate surface particles and additional contamination. An optical emission spark spectrometer was used to determine the chemical elements present in the samples. Argon gas was used as an inert atmosphere gas medium through a purifier in the spectrometer. After argon gas stabilization, the specimen was positioned on an anvil and clamped.[27] A minimum of three sparks per specimen were made on different positions of the polished surface to determine the average values and standard deviation. Percentage of the elements present in AISI 4340 steel at the initial stage of the study is discussed in Table I.[28]

TABLE I. Chemical analysis of AISI 4340 steel before heat treatment

Element	C	Si	Mn	Cr	Mo	Ni	T	Cu	Co	P	S	Fe
wt. %	0.37	0.25	0.70	0.82	0.02	0.11	0.14	0.15	0.006	0.016	0.019	Balance

Heat treatment procedure

The standard specimens for the impact and tensile tests were prepared from the round bars of AISI 4340 steel placed in a muffle furnace for hardening at 850 °C for 45 min, followed by oil quenching in mineral oil. The hardened heat-treated work material was tempered at 350, 450 and 550 °C and allowed to cool to room temperature.

Hardness testing trials

Hardened and tempered samples were investigated by using a Vickers hardness testing machine HM-100 Series (HV-100), Japan, to measure the resistance to indentation.[29] Indentation was made on well-prepared specimens. A 20 kg load was applied for indentation, and the indentations were examined using a microscope. Indentation was measured at an appropriate distance from the sample edge to avoid any edge effects. Three different measurements were made to identify the hardness value of the standard specimen.

Charpy impact testing technique

Impact testing for energy absorption of heat-treated samples was conducted by applying the force of a swinging pendulum. The geometry of the specimens for the Charpy impact test was in accordance with ASTM standard E23 using a Charpy impact testing machine XJJD-50 China.[30] The specimens were prepared according to ASTM standard E23.

Tension testing

In the tension test, standard samples were fixed in the grips of the tensile testing machine (ZwickRoell SE-250KN, ZwickRoell Group, Germany) equipped with an electronic load cell. The upper crosshead of the tension testing machine dragged the specimens upward to failure with a constant crosshead speed of 10 mm s^{-1}, to maintain a preliminary strain rate of 2.8×10^{-4}. The stress-strain diagram showed the mechanical properties such as yield strength, ultimate tensile strength and toughness before fracture. The dimension of tensile test samples were in accordance with ASTM standard E8.[31]

RESULTS AND DISCUSSION

AISI 4340 steel in the as-received condition

At first, the chemistry of AISI 4340 steel was analysed and given in Table II. In the chemical analysis, it was evident that 0.82 % Cr is an alloying element present in the steel to enhance resistance against degradation. The strength, toughness, hardness (30 kg load), energy absorption, and tensile properties of the initial samples are presented in Table II.

TABLE II. Mechanical properties of the work material before treatment

Material	*HVN* (30 kg)	Impact *E* J	*UTS* MPa	Breaking stress MPa	Elongation %
AISI 4340 before treatment	135	9.5	715	468.73	33.92

Pictorial views of as-received samples of AISI 4340 steel confirm the identification of ferrite structure and pearlite phase in microstructural examination, and the lighter phase corresponds to ferrite. Micrographs were recorded *via* a light optical microscope.

Heat treatment

This contemporary study is capable of enhancing the energy absorption and strength of AISI 4340 low-strength high-alloy steel *via* heat heat-treatment processes; consequently, once the work pieces were ready for mechanical characterization. At the begging selected samples were subjected to hardening at 850 °C for 45 min and followed by quenching. Secondly, the specimens were tempered at 350, 450 and 550 °C for 45 min and quenched in air.[32,33]

Hardening procedure of AISI 4340 steel

Following the hardening heat treatment of AISI 4340 steel, it was found that Vickers hardness values increased considerably to 625 (30 kg), whereas the absorbed energy and internal reactive force decreased to 7.53 J and 1520 MPa, respectively. The hardening of AISI 4340 steel reduced the ductility and increased the brittleness. The micrograph contains very fine-grained martensitic regions. Since martensitic regions have a BCT crystal structure and are considered as the hardest phase.[34] The pictorial views of the hardening treatment have good agreement with the outcomes reported previously.

Tempering technique of AISI 4340 steel

Tempering treatment after the hardening procedure improves the strength and ductility of the martensitic phase structure of AISI 4340 steel, whereas decreases the hardness.[35] Findings of tempering heat treatment are arranged in tabular form Table III. Statistical analysis of the mechanical properties of the materials (AISI 4340 steel) is presented in the comparative graph shown in Fig. 2.

TABLE III. Mechanical properties of the work material after temper treatment

Material	Tempering temp., °C	HVN (30 kg)	Impact *E* J	*UTS* MPa	Elongation %
AISI4340	350	232.6	10.49	1400.69	22.59
	450	219	20	1456.98	29.32
	550	198.13	39	1255.07	30.99

It was discovered that the toughness and hardness of the work material are affected by heating in a furnace for hardening and followed by tempering at different temperature levels. Hardening treatment achieved the utmost hardness and tensile strength and reduced the percentage elongation.[36] As reported by researchers, the phase change of AISI 4340 steel might be due to the quenching

route, where abrupt changes occur in crystal structure phase from gamma (γ), *i.e.*, FCC to BCT and a martensitic phase structure.[37] Rapid intensification in Vickers hardness and strengths occurs during transformation in platelets of the martensite phase, producing enormous alteration, and the same trend was also observed on similar materials.[38] It can be seen from the tempering results that improvement of hardness, ultimate strength and toughness is shown in Fig. 2.

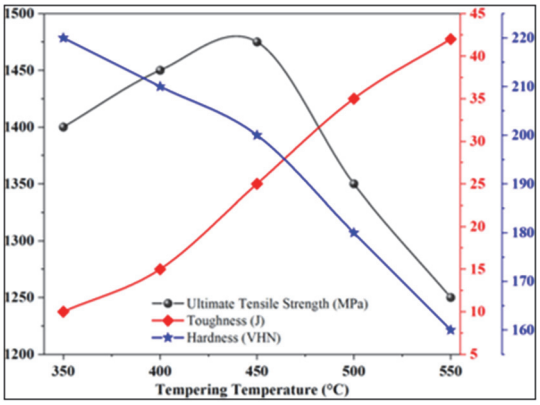

Fig. 2. Comparative analysis of mechanical properties after tempering of hardened AISI 4340 steel at 350–550 °C for 45 min.

The comparative analysis of the heat-treatment results showed that hardness and strength were drastically reduced from 625 to 232.6 *HVN* at 30 kg, and from 1520 to 1400.69 MPa, respectively, whereas the energy absorption increased from 7.53 to 10.49 J. Based on the results, it can be concluded that internal stresses produced by changes in martensitic morphology and contributed to improved ductility. Moreover, a notable change in mechanical properties of the AISI4340 steel was obtained after tempering at 450 °C for 45 min. Furthermore, analysis of the data after heat treatment of AISI 4340 steel showed a decline in hardness values and an increase in strengths and toughness. This can be attributed to the fact that the section was tempered at 550 °C for the same duration, resulting in a decrease in hardness and tensile strength but an increase in toughness. Hence, tempering heat treatment practice of AISI 4340 steel at 450 °C achieves an optimum balance of hardness, tensile strength and toughness.[13] Experimental evidence shows that low-carbon Mn–Si–Cr steel, when quenched after the hardening procedure, causes phase conversion and affects the mechanical properties.

Scanning electron microscopy analysis

High-strength low-alloy steel is designed particularly for space shuttle, aircraft, and missile structures for defence applications. AISI 4340 steel was subjected to heating and cooling processes to improve fracture resistance and enhance tensile strengths. By heat treatment, the mechanical strength properties of high

strength low alloy steel were modified through tempering and subsequent quenching.[39] Phase change of steel occurs by the hardening and tempering technique. The transformed microstructures, like retained austenite, lower bainite, martensite and some carbides, were recognized by means of a high-resolution transmission electron microscope.[40] It can also be discussed that retained austenite is capable of arresting crack propagation and increases resistance to fracture of low alloy medium carbon steel. Furthermore, research findings indicate that the cracks traveling through martensite are impassable while passing through a region of retained austenite. If internal reactive forces are present, cracks harvest the branches and started to increase close to austenite region, therefore more energy is absorbed through the martensite plates and this promotes the toughness of steel. AISI 4340 steel containing lower bainite and tempered martensite as a dual phase is extensively studied concerning its mechanical properties. It is notified that the dual-phase steel provides a healthier combination of strength and toughness compared with wholly martensitic structures.[41] discussed previously from the optical micrographs, detailed information regarding variations occurring through the phase alteration process was required, hence, it was found essential to inspect hardened and tempered work pieces by using SEM. The micrograph in Fig. 3a shows evidence of a dual-phase microstructure containing lower bainite and martensitic structure of AISI 4340 steel tempered at a temperature of 350 °C for 45 min. The SEM microstructure captured at high resolution and magnification is displayed in Fig. 3b, showing a dual-phase microstructure of lower bainite and martensite plates layered with an austenitic phase structure on the grain boundaries. A comparable topography was detected (Fig. 3c and d), for the specimens inspected with high resolution SEM after tempering at 450 and 550 °C for 45 min.

In this contemporary study, a steel grade was hardened and tempered to reduce the hardness associated with martensitic structure while enhancing the high-energy region. It has been testified by numerous investigators.[42] that P, S and Sn and antimony have an adverse effect on steel showing a brittle appearance once tempered. Impurities present in the steel tend to segregate near the austenitic region and decohesion across the grain boundaries, which eventually results in inter granular brittle failure. These consequences arise from impurity segregation promoted by tempering treatment of steel at elevated temperature. While the similar steel grade, when quenched from elevated temperature, irregularities within the material do not activate during cooling and therefore reduce the embrittlement mechanism of fracture. As is evident from reported results, tempered specimens failed during tensile test and were studied using a scanning electron microscope. The micrograph shown in Fig. 4a represents the fractured surface of a work piece tempered at 350 °C, scrutinized under a scanning electronic microscope and conforming stress-strain photograph. AISI 4340 sectioned pieces exhibited intergranular fracture, which is characteristic of brittle fracture. Illustration of stress-strain diagram

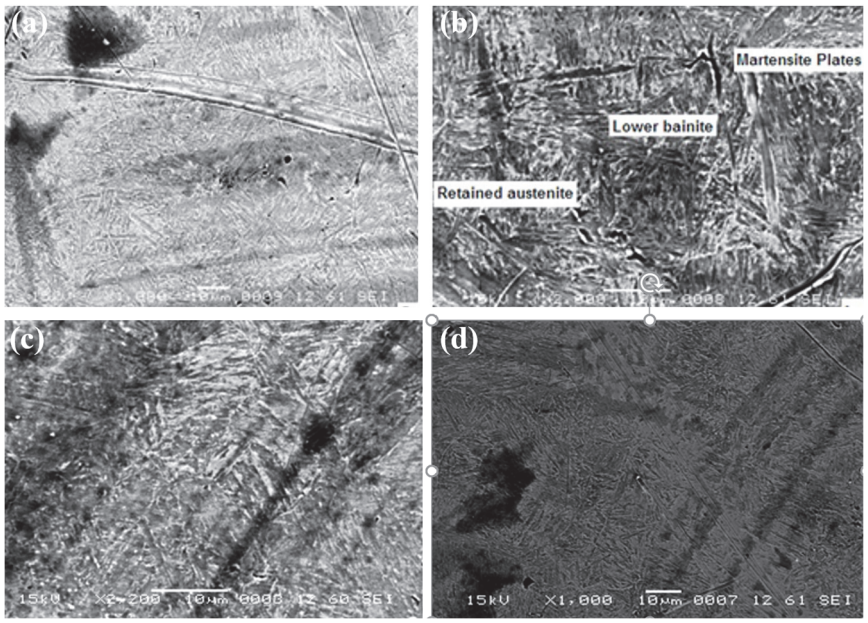

Fig. 3. SEM micrograph of AISI 4340 steel tempered at: a) 350 and b) 450 °C; comparative topography at: c) 450 and d) 550 °C.

did not present any yielding and elongation all through the tensile test. These values indicate brittle fracture material behaviour. Fracture along the grain boundaries of the tempered martensitic phase structure is in good agreement with discoveries conferred previously. New findings quantified in Table IV signify the tempering temperature at 350 °C. The hardness values are comparatively higher and impact energy is relatively lower than the finding of hardness and impact energy noted when tempered at 450 °C. Illustration of Table IV also indicates an increase in tensile strength of the work material. Therefore, the increase in impact energy is accompanied by considerable reduction in the hardness and strength of the specimens.[43] Micrographs were recorded for AISI 4340 steel tempered at 350, 450 and 550 °C, as presented in Fig. 4a–c. As the tempering temperature increases, the fracture morphology exhibits a distinct change in failure mode, which is directly correlated with modifications in mechanical behaviour. The fracture surface primarily displays intergranular and quasi-cleavage features in Fig. 4a, which corresponds to tempering at 350 °C. This suggests a relatively brittle fracture mechanism. Tempered martensite with high residual stresses and fine ε-carbides, which restrict plastic deformation and encourage crack initiation along previous austenite grain boundaries, is linked to this behaviour. As a result, this condition is usually characterized by increased strength and hardness but reduces toughness. As seen in Fig. 4b, the fracture mode changes towards ductile fracture when the tempering temperature is raised to 450 °C. Microvoid nucleation, growth and coalescence

produce uniformly distributed dimples on the fracture surface. This transition shows increased plasticity as a result of controlled cementite (Fe_3C) precipitation and partial martensitic structure recovery. Strength and toughness are better balanced at this tempering condition, which is frequently regarded as ideal for AISI 4340 steel. The fracture surface exhibits deeper and larger dimples at the maximum tempering temperature of 550 °C (Fig. 4c), indicating a fully ductile fracture mechanism. Carbide coarsening and spheroidisation, as well as substantial stress relief and martensite breakdown into a ferrite–carbide matrix are responsible for the increase in dimple size. This microstructural evolution leads to increased ductility and impact toughness but decreased hardness and strength. The evolution of carbide precipitation Fe_3C and the transformation of the martensitic phase are reflected in the progressive increase in dimple size with tempering temperature. The observed trends in the mechanical properties of tempered and hardened AISI 4340 steel are strongly supported by these morphological changes seen in SEM fractography.

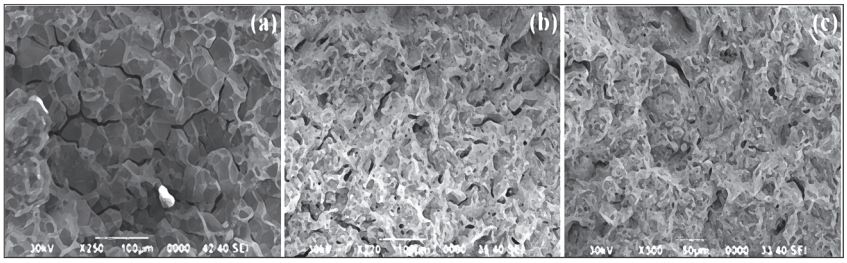

Fig. 4. SEM Analysis of samples after tempering at: a) 350, b) 450 and c) 550 °C.

TABLE IV. Tensile properties of AISI 4340 steel at various tempering temperatures

Sample	Tempering temp., °C	Diameter (d_0 / mm)	L_0 / mm	*Fmax* N/mm^2	F_{Break} %	*eBreak* %	*e-Fmax* %
(a)	350	12.5	35.08	1400.09	1400.09	22.59	22.59
(b)	450	12.5	35.14	1456.96	1186.72	36.53	29.32
(c)	550	12.5	30.07	1255.02	980.52	41.47	30.99

Table IV presents the tensile properties of three samples subjected to different tempering temperatures (350, 450 and 550 °C), has been fixed by chamber oven UF160-Memmeryt GmbH+Co. Kg, Germany, highlighting the influence of heat treatment on tensile behaviour. At 350 °C, the sample exhibits a maximum stress of 1400.09 N/mm^2, Fig. 5, which increases to 1456.96 N/mm^2 at 450 °C, indicating enhanced strength due to the tempering-induced microstructural changes, such as stress relief and carbide precipitation. However, a further increase in tempering temperature to 550 °C results in a reduction to 1255.02 N/mm^2, suggesting over-tempering, where coarsening of the microstructure and reduction in dislocation

density lead to decreased strength. A similar trend is observed in the fracture strength, which drops significantly from 1400.09 % at 350 °C to 980.52 % at 550 °C, reflecting a loss in the material's ability to withstand stress before failure as it becomes more ductile. Meanwhile, the elongation at break (*eBreak*) and at maximum stress (*e-Fmax*) increase progressively with tempering temperature, rising from 22.59 % at 350 °C to 41.47 and 30.99 %, respectively, at 550 °C. This indicates a clear enhancement in ductility due to the transformation of the brittle martensitic structure into a more plastic and deformable phase. The results reveal a classic trade-off between strength and ductility with increasing tempering temperature. The sample tempered at 450 °C demonstrates an optimal combination of high tensile strength and improved elongation, suggesting that it may offer the best mechanical performance among the three conditions for applications requiring both durability and formability.

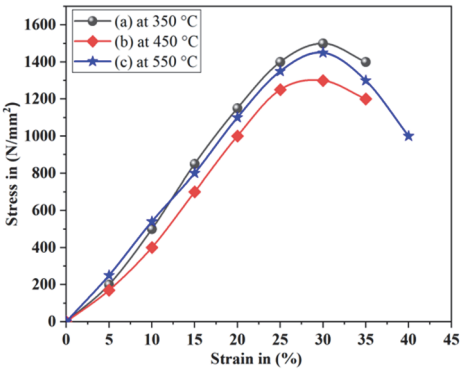

Fig. 5. Illustration of the tensile properties of AISI 4340 steel at different tempering temperatures.

CONCLUSION

This study investigated the tempering of AISI 4340 steel to optimize its mechanical properties, finding that different tempering temperatures yield distinct results. Tempering at 350 °C primarily enhances tensile strength without significantly improving ductility or impact energy, while a higher temperature of 450 °C for 45 min provides an optimal balance, effectively increasing both toughness and ductility while maintaining acceptable levels of strength and hardness. Conversely, tempering at 550 °C leads to a further increase in impact energy and ductility but results in a more significant reduction in strength and hardness. This observed behaviour is directly linked to the formation of tempered martensite within the steel's microstructure, as confirmed by microstructural analysis. Therefore, the findings suggest that a tempering treatment of 450 °C for 45 min is the most effective approach for achieving a desirable combination of mechanical properties for a wide range of engineering applications.

ИЗВОД

ИСПИТИВАЊЕ МОРФОЛОШКИХ И МЕХАНИЧКИХ СВОЈСТАВА КАЉЕНОГ И ОТПУШТЕНОГ ЧЕЛИКА AISI 4340

SUBHAN ALI[1], ABDUL QADEER LAGHARI[2], ARSHAD IQBAL[3], GHULAM MUSTAFA MEMON[4], IFITKHAR AHMED MEMON[1], FIDA HUSSAIN CHANNA[5], ABDUL SAMI CHANNA[6], MASROOR ABRO[2], KHAN MUHAMMAD[3] и SHOUKAT ALI NOONARI[7]

[1]Materials Engineering Department, Dawood University of Engineering and Technology, Karachi, 74800, Sindh, Pakistan, [2]Chemical Engineering Department, Mehran University of Engineering and Technology, Jamshoro,76080, Pakistan, [3]Chemical Engineering Department,, Dawood University of Engineering and Technology, Karachi, 74800, Sindh, Pakistan, [4]IRC for Industrial Nuclear Energy, King Fahd University of Petroleum & Minerals, Saudi Arabia, [5]Mining Engineering Department, Mehran University of Engineering and Technology, Jamshoro,76080, Pakistan, [6]Chemical Engineering Department, Qaid-e-Awam University of Engineering and Technology, Nawabshah, 74800, Pakistan и [7]Department of Mechanical Engineering, Isra University, Hyderabad, Sindh, Pakistan

Челик AISI 4340 се због своје изврсне механичке чврстоће и отпорности на удар широко користи у индустријама високог ризика. Механичка својства овог челика могу се значајно побољшати термичком обрадом, нарочито отпуштањем на контролисаним температурама. Ова студија истражује утицај отпуштања на микроструктуру и механичка својства челика AISI 4340. Експериментална анализа обухвата карактеризацију пре и после термичке обраде како би се проценили промене у чврстоћи, жилавости и дуктилности. Резултати испитивања показују да отпуштање на 450 °C (45 min) оптимално побољшава енергију удара и дуктилност, уз благо смањење тврдоће и чврстоће, док отпуштање на 550 °C доводи до израженијег повећања енергије удара и дуктилности, али по цену већег смањења тврдоће и чврстоће. Микроструктурна испитивања потврђују формирање отпуштеног мартензита, што доприноси уоченом механичком понашању. Ови налази пружају драгоцен увид у оптимизацију параметара термичке обраде челика AISI 4340 ради постизања баланса чврстоће, жилавости и дуктилности за индустријску примену.

(Примљено 23. новембра, ревидирано 26. децембра 2025, прихваћено 9. марта 2026)

REFERENCES

1. S. M. Safi, M. K. B. Givi, *Met. Sci. Heat Treat.* **56** (2014) 78 (https://doi.org/10.1007/s11041-014-9707-z)
2. C. Aygüzer, *MSc Thesis*, Middle East Technical University, Turkey, 2023, (https://hdl.handle.net/11511/107732)
3. L. Sharma,R. Chhibber, *Proc. Inst. Mech. Eng. E: J. Process Mech. Eng.* **235** (2021) 266 (https://doi.org/10.1177/0954408920958104)
4. L. Moravcikova-Gouvea, I. Moravcik, M. Omasta, J. Veselý, J. Cizek, P. Minárik, J. Cupera, A. Záděra, V. Jan, I. Dlouhy, *Mater. Charact.* **159** (2020) 110046 (https://doi.org/10.1016/j.matchar.2019.110046)
5. T. Siostrzonek, J. Wójcik, M. Dutka, W. Siostrzonek, *Energies* **17** (2024) 5675 (https://doi.org/10.3390/en17225675)
6. K. M. Groth, A. Al-Douri, M. West, K. Hartmann, G. Saur, W. Buttner, *Int. J. Hydrogen Energy* **51** (2024) 1023 (https://doi.org/10.1016/j.ijhydene.2023.07.165)
7. A. Fande, S. Kavishwar, V. Tandon, D. C. Narayane, D. Bandhu, *Mater. Res. Express.* **11** (2024) 056519 (https://doi.org/10.1088/2053-1591/ad4bab)

8. R. Seede, B. Zhang, A. Whitt, S. Picak, S. Gibbons, P. Flater, A. Elwany, R. Arroyave, I. Karaman, *Addit. Manuf.* **47** (2021) 102255 (https://doi.org/10.1016/j.addma.2021.102255)
9. Y. Zhang, J. Yang, D. Xiao, D. Luo, C. Tuo, H. Wu, *Metals* **12** (2022) 1087 (https://doi.org/10.3390/met12071087)
10. F. Deirmina, N. Peghini, B. AlMangour, D. Grzesiak, M. Pellizzari, *Mater. Sci. Eng., A* **753** (2019) 109 (https://doi.org/10.1016/j.msea.2019.03.027)
11. F. Hosseinifar, A. Ekrami, *Mater. Sci. Eng., A* **830** (2022) 142314 (https://doi.org/10.1016/j.msea.2021.142314)
12. A. Khodabandeh, D. Sayadi, S. Rajabi, M. Khosrojerdi, M. Khajehzadeh, M. R. Razfar, *Proc. Inst. Mech. Eng., C.*: *J. Mech. Eng. Sci.* **238** (2024) 7607 (https://doi.org/10.1177/09544062241232236)
13. M. Parvinzadeh, S. S. Karganroudi, N. Omidi, N. Barka, M. Kh Int. *J. Adv. Manuf. Technol.* **115** (2021) 1 (https://doi.org/10.1007/s00170-021-07351-5)
14. M. K. Sanij, S. G. Banadkouki, A. Mashreghi, M. Moshrefifar, *Mater. Des.***42** (2012) 339 (https://doi.org/10.1016/j.matdes.2012.06.017)
15. A. Kokosza, J. Pacyna, *Arch. Metall. Mater.* **59** (2014) 1017 (https://doi.org/10.2478/amm-2014-0170)
16. I. Dey, R. Saha, B. Mahato, M. Ghosh, S. Ghosh, *Metall. Mater. Trans., A* **55** (2024) 1 (https://doi.org/10.1007/s11661-024-07431-7)
17. M. de Souza, L. F. Serrão, J. M. Pardal, S. S. M. Tavares, M. C. Fonseca, *Int. J. Adv. Manuf. Technol.* **120** (2021) 1123 (https://doi.org/10.1007/s00170-022-08880-3)
18. S. Sharma, J. Singh, M. K. Gupta, M. Mia, S. P. Dwivedi, A. Saxena, S. Chattopadhyaya, R. Singh, D. Y. Pimenov, M. E. Korkmaz, *J. Mater. Res. Technol.* **12** (2021) 1564 (https://doi.org/10.1016/j.jmrt.2021.03.095)
19. M. Kumaran, S. Ravi, *Mater. Lett.* **377** (2024) 137427 (https://doi.org/10.1016/j.matlet.2024.137427)
20. D. Schröpfer, A. Kromm, T. Lausch, M. Rhode, R. Wimpory, T. Kannengießer, *Weld. World.* **14** (2021) 1 (https://doi.org/10.1007/s40194-021-01101-7)
21. J. Yang, Z. Zhu, S. Han, Y. Gu, Z. Zhu, H. Zhang, *J. Alloys Compd.* **1008** (2024) 176707 (https://doi.org/10.1016/j.jallcom.2024.176707)
22. T. Sonar, S. Lomte, C. Gogte, *Mater. Today: Proc.* **5** (2018) 25219 (https://doi.org/10.1016/j.matpr.2018.10.324)
23. V. S. J. Milton, Z. C. J. Wilmer, H. A. D. Bryan, Z. C. J. Gregorio, Á. R. A. Linzan, M. E. C. Guaigua, A. C. Z. Rodríguez, *Nanotechnol. Perceptions* **20** (2024) 307 (https://doi.org/10.62441/nano-ntp.vi.408)
24. E. Tkachev, S. Borisov, A. Belyakov, T. Kniaziuk, O. Vagina, S. Gaidar, R. Kaibyshev, *Mater. Sci. Eng., A* **868** (2023) 144757 (https://doi.org/10.1016/j.msea.2023.144757)
25. A. Panda, R. Bag, A. K. Sahoo, R. Kumar, *Int. J. Integr. Eng.* **12** (2020) 61 (https://publisher.uthm.edu.my/ojs/index.php/ijie/article/view/5667)
26. A. Saboori, A. Aversa, G. Marchese, S. Biamino, M. Lombardi, P. Fino, *Appl. Sci.* **9** (2019) 3316 (https://doi.org/10.3390/app9163316)
27. J. Miao, L.-l. Yu, X.-g. Liu, B.-f. Guo, *Trans. Nonferrous Met. Soc. China* **28** (2018) 2082 (https://doi.org/10.1016/S1003-6326(18)64852-6)

28. J. Yan, C. Zhang, J. Guo, G. Dong, S. Wang, J. Gao, H. Wu, H. Zhao, J. Lu, Y. Huang, X. Mao, *J. Mater. Res. Technol.* **38** (2025) 3264 (https://doi.org/10.1016/j.jmrt.2025.08.142)
29. M. A. Hafeez, M. Usman, M. A. Arshad, M. AdeelUmer, *Crystals* **10** (2020) 508 (https://doi.org/10.3390/cryst10060508)
30. L. F. Monaheng, W. B. du Preez, C. Polese, *Metals* **11** (2021) 1736 (https://doi.org/10.3390/met11111736)
31. J. Na, J. Middendorf, M. Lander, J. Waller, R. Rauser, in *Structural Integrity of Additive Manufactured Parts*, N. Shamsaei, S. Daniewicz, N. Hrabe, S. Beretta, J. Waller, M. Seifi, Eds., ASTM International, West Conshohocken, PN, 2020, p. 206 (https://doi.org/10.1520/STP162020180095)
32. S. Bakhshi, M. Asadi Asadabad, S. Bakhshi, S. Bakhshi, *Ironmak. Steelmak.* **50** (2023) 295 (https://doi.org/10.1080/03019233.2022.2107111)
33. S. Khatai, A. K. Sahoo, R. Kumar, A. Panda, *Proc. Inst. Mech. Eng., C: J. Mech. Eng. Sci.* **238** (2024) 10997 (https://doi.org/10.1177/09544062241276347)
34. W. Tan, , *PhD Thesis*, New York State College of Ceramics at Alfred University, 2017, (http://hdl.handle.net/10829/24629)
35. M. M. Bilal, K. Yaqoob, M. H. Zahid, W. H. Tanveer, A. Wadood, B. Ahmed, *J. Mater. Res. Technol.* **8** (2019) 5194 (https://doi.org/10.1016/j.jmrt.2019.08.042)
36. S. Sharma, A. Kini, G. Shankar, T. Rakesh, H. Raja, K. Chaitanya, M. Shettar, *J. Mech. Eng. Sci.* **12** (2018) 3866 (https://doi.org/10.15282/jmes.12.3.2018.8.0339)
37. A. F. Brust, *PhD Thesis*, Ohio State University, 2019 (http://rave.ohiolink.edu/etdc/view?acc_num=osu1555523646156822)
38. M. Motyka, *Metals* **11** (2021) 481 (https://doi.org/10.3390/met11030481)
39. F. P. Li, N. Li, X. L. Wang, M. H. Liang, *Mater. Sci. Forum* **1035** (2021) 424 (https://doi.org/10.4028/www.scientific.net/MSF.1035.424)
40. X. Wang, C. Liu, Y. Qin, Y. Li, Z. Yang, X. Long, M. Wang, F. Zhang, *Mater. Sci. Eng., A* **832** (2022) 142357 (https://doi.org/10.1016/j.msea.2021.142357)
41. M. Elitas, *Mater. Test.* **63** (2021) 124 (https://doi.org/10.1515/mt-2020-0019)
42. G. Muthukumaran,P. D. Babu, *Arab. J. Sci. Eng.* **1008** (2022) 1 (https://doi.org/10.1007/s13369-021-06350-8)
43. F. A. Khatir, M. H. Sadeghi,S. Akar, *J. Manuf. Process.* **61** (2021) 173 (https://doi.org/10.1016/j.jmapro.2020.09.073).

Journal of the Serbian Chemical Society
JSCS-info@shd.org.rs • www.shd.org.rs/JSCS
J. Serb. Chem. Soc. 91 (5) 529–543 (2026)
JSCS–5507
Original scientific paper
Published 12 June, 2026

Adsorption of clofibric acid on the activated carbon prepared from polyester cloth waste: Study of the operational parameters, kinetics and adsorptive equilibrium using the non-linear method

NASSIMA BOUDRAHEM-BOUALIT[1-3]*, NABIL MAMERI[3] and MOUNA CHALA[1]

[1]Laboratoire des Sciences et Techniques de l'Environnement, Ecole Nationale Polytechniques Alger, Avenue Pasteur El Harrach, 16110 Alger, Algeria, [2]Faculté de Technologie, Université de Bejaia, Bejaia 06000, Algeria and [3]Laboratoire de biotechnologie, Ecole Nationale Polytechniques Alger, Avenue Pasteur El Harrach, 16110 Alger, Algeria

(Received 15 May, revised 25 June, accepted 6 August 2025)

Abstract: The objective of this research work was to examine the feasibility of preparing adsorbent materials from textile waste (polyester) for the elimination of pharmaceutical products such as clofibric acid (CA). The results showed that the adsorbents prepared by chemical activation in the presence of phosphoric acid followed by pyrolysis at 600 °C led to microporous materials with large specific surfaces. Batch experiments were conducted to study the effect of contact time, initial CA concentration, solution pH and temperature. Elimination yields by adsorption of CA in aqueous solution greater than 95 % were obtained with dilute solutions (10 mg L^{-1}) at room temperature and at pH 3. The adsorption kinetics is perfectly described by the pseudo-second-order model and the isotherms are of the Freundlich types. The results indicate that this process is spontaneous, efficient and potentially applicable in the removal of CA from water.

Keywords: activated carbon cloth; pharmaceutical active compounds; waste water; H_3PO_4.

INTRODUCTION

Pharmaceutical active compounds (PhACs) are a class of emergent pollutants that are being continuously introduced into the environment mainly due to improper disposal of unused or expired drugs and through excretion and inefficient removal in sewage treatment plants (STPs).[1] Even though the amounts found in the environment are usually low (they are often detected in trace concentrations (ng L^{-1}), long-term exposure of aquatic and terrestrial organisms may provoke adverse effects on respective ecosystems.[2] Some of these compounds such as carbamazepine, clofibric acid, diclofenac, tetracycline, paracetamol and caffeine

* Corresponding author. E-mail: nassima.boudrahem@g.enp.edu.dz
https://doi.org/10.2298/JSC250515063B

have shown persistent behavior, which may lead to their bioaccumulation when present in the environment. Moreover, the degradation of some drugs can produce highly toxic and carcinogenic compounds.

It is thus important to remove all these pharmaceutical products from wastewater and this can be done using electrochemical methods, membrane filtration, adsorption, biodegradation and advanced oxidation processes (AOPs). Compared with the above methods, adsorption is considered as a promising method for removing various pollutants from wastewater due to its economical, renewable, and flexible operation.[3]

Activated carbon cloths (ACCs) present technological advantages over more traditional powder or granular forms of activated carbons, including high adsorption capacity, uniform porosity and high rates of adsorption/desorption from the gas or liquid phase, as well as new applications such as molecular sieves, catalysts and electrodes.[3,4] The textural and chemical characteristics of activated carbon depend on the nature of the precursor used as well as the methods and conditions of production.[5] Currently, the major precursors for producing ACC include synthetic materials such as acrylic, nylon and polyester fibres and natural materials such as wool, flax, viscose and cotton.[3] The preparation of activated carbon from polyester woven waste, similar to that of conventional activated carbon, involves its treatment by physical or chemical activation processes.[6]

Some researchers have shown ACCs' efficiency in aqueous media for the removal of organic and inorganic compounds for example Brasquet *et al*.[7] examined the quantitative structure–property relationship for the adsorption of 55 organic compounds onto activated carbon cloth. Brasquet and Cloirec[8] studied the effects of activated carbon cloth surface properties on organic adsorption in aqueous solutions. Ayranci and Dumain[9] evaluated the adsorption capacity of ACCs vis-a-vis of phenolic compounds (phenol, hydroquinone, *m*-cresol, *p*-cresol and *p*-nitrophenol). Adsorption of cadmium by activated carbon cloth based on polyacrylonitrile fibre as a precursor was oxidised using nitric acid, ozone and electrochemical oxidation has been reported by Rangel-Mendez and Streat.[10] Álvarez-Merino *et al*.[11] investigated the adsorption of Zn(II) ions from aqueous solution under static conditions using commercial activated carbons in the form of grains and cloth. Akkouche *et al.*[12] studied the adsorption of tetracycline and paracetamol from aqueous solutions using activated carbon derived from cotton textile waste modified with H_3PO_4. Boudrahem *et al*.[3] studied the adsorption of clofibric acid from aqueous solutions using activated carbon derived from cotton textile waste activated with H_3PO_4.

In this work we investigated the feasibility of using polyester cloth waste as precursor for the production of activated carbons with activation by H_3PO_4. The physicochemical properties of ACs, such as BET surface area, morphology and surface functional groups, were analyzed to better understand the mechanism of

adsorption of clofibric acid (2-(*p*-chlorophenoxy)-2-methylpropionic acid, CA. The effects of initial concentration of the adsorbate, pH of the solutions, contact time and temperature were evaluated. Moreover, different adsorption isotherm models, including Langmuir and Freundlich were used to analyze the adsorption equilibrium data. Pseudo-first and pseudo-second order models were used to study the kinetic process.

The choice of textile waste in this study is linked to its great availability, its low cost and the need to preserve natural resources for future generations. For example, it is estimated that the production of textile waste in Algeria in the year 2014 was 1,430,000 t. As for the choice of the target molecule (clofibric acid), this is due to its belonging to a class of consumer products, to its presence in the environment and its specific action on microorganisms.

EXPERIMENTAL

Materials

Polyester cloth waste used in this study was obtained from a clothing production factory (ALCOST-Bejaia-Algeria). Nitrogen gas was industrial grade of 99 % purity. The reagent grade chemicals used in the study (H_3PO_4, H_2SO_4, HCl, NaOH) and clofibric acid (CA), were purchased from Aldrich and Junsei chemical companies.

Preparation of the activated carbon (AC)

Polyester cloths residues were used as a precursor for the preparation of AC. The cloths, previously weighed, were immersed in the H_3PO_4 solution for 7 h at 85 °C to ensure the access of the activating agent to the interior of the precursor, and then the temperature of the mixture was increased and maintained at 100 °C until it was completely dry. Three activation ratios, 25, 50 and 75 wt. % (wt = mass of H_3PO_4/mass of precursor) were tested. The dried samples were pyrolyzed at 600 °C for 1h under an inert gas stream (N_2 flow). The heating rate was 10 °C min^{-1}. The AC samples were cooled down to room temperature while still under N_2 flow. Afterwards, the resulting activated carbons were rinsed thoroughly with distilled hot water until a neutral pH was obtained in order to remove all acid, then dried and kept in a desiccator before use.

Characterization of the AC prepared

The surface area, micropore volume and pore size distribution were determined using the nitrogen adsorption isotherm technique measurements at the liquid nitrogen temperature of 77 K (Micromeritics Instrument Corporation MicroActive Tristar II 3020).

The surface morphology of ACs was examined by scanning electron microscopy (SEMJSM820, Jeol Ltd., Japan).

The surface chemical properties of the samples were characterized by the Fourier-transform infrared spectroscopy (Shimadzu FTIR-8300, Japan) at room temperature. The spectra were recorded in the 4000–400 cm^{-1} wavenumber range.

The carbon surface charge is mainly determined by the pH of the adsorbate solution. The pH at the point of zero charge (pH_{PZC}) of the carbon was determined using the method reported by Khenniche and Aissani.[13]

Batch adsorption procedure

Adsorption experiments were carried out by mixing 0.25 g of ACs with 250 mL of each clofibric acid solution (10 to 100) mg L^{-1} in a batch reactor (500 mL) under the following

conditions: 360 rpm stirring speed, 3 h contact time, temperature, 20, 30, 40 and 50 °C, and desired initial pH value of the solution. The concentration of the clofibric acid was measured using a UV–Vis spectrophotometer at a wavelength of 227 nm. The CA adsorption capacity at time t, q_t, was evaluated using as:

$$q_t = \frac{(C_o - C_t)V}{m} \quad (1)$$

in which q_t is the adsorption capacity at time t (mg g^{-1}), C_0 (mg L^{-1}) is the initial concentration of CA, C_t (mg L^{-1}) is the concentration of CA at time t, V (L) is the volume of the CA solution and m (g) is the mass of the ACs. At the equilibrium: $q_t = q_e$ and $C_t = C_e$.

RESULTS AND DISCUSSION

Optimization of adsorbent characteristics

Nitrogen adsorption – textural characteristics. Before attempting to obtain quantitative information, a study of the form and textural characteristics was imposed. Nitrogen adsorption–desorption isotherms were plotted for the various adsorbents prepared by plotting the amount of nitrogen adsorbed or desorbed per g of adsorbent as a function of relative pressure. The results presented in Fig. 1 show that all nitrogen adsorption isotherms are type I (Langmuir isotherm) according to the IUPAC classification.[14] This type of isotherm suggests that the adsorbents are of the microporous type. This result was confirmed by the desorption isotherm. The speed of reaching the plateau is an indication of the pore size distribution and the presence of the horizontal plateau suggests a very low external surface area.

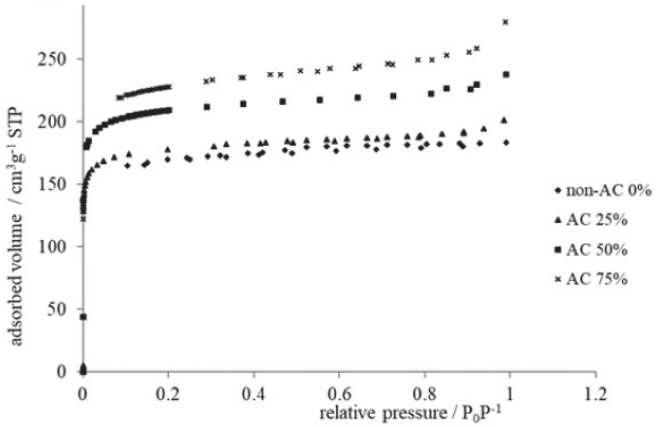

Fig. 1. Adsorption–desorption isotherms of nitrogen at 77 K of ACs with different H_3PO_4 impregnation ratios.

The physical properties results obtained from the N_2 adsorption–desorption isotherms of all ACs were determined and reported in Table I.

Analysis of the Table I data reveals that activated carbons prepared from polyester are characterized by large specific surface areas. The activation increases the

S_{BET}. V_t, V_{mic} and V_{mes}. The microporosity ratio (V_{mic}/V_t), %, of the adsorbents prepared decreases with the impregnation ratio, decreasing from 99.74 % for non-activated carbon 0 % H_3PO_4 to 98.6 % for an activation rate of 75 % H_3PO_4. We have noticed in this case the development of mesoporosity. This effect may be due to the hydrolysis of the polyester during the impregnation with the acid, which means an important release of volatile compounds during the heat treatment.[15] These results are confirmed by Ramos *et al.*,[15] showing that the use of phosphoric acid as an activating agent not only contributes to the creation of new micropores but also to the enlargement of the pores already existing in the precursor.

TABLE I. Physicochemical properties of activated carbons

Parameter	Impregnation ratio with H_3PO_4			
	AC 0 %	AC 25 %	AC 50 %	AC 75 %
V_{tot} / $cm^3\ g^{-1}$	0.271	0.335	0.285	0.369
V_{mic} / $cm^3\ g^{-1}$	0.271	0.326	0.274	0.363
Microporosity, V_{mic}/V_{tot} in %	99.74	97.41	96.18	98.6
V_{mes} / $cm^3\ g^{-1}$	0.00072	0.0087	0.011	0.0052
Mesoporosity, V_{mes}/V_{tot} in %	0.264	2.591	3.819	1.4
S_{BET} / $m^2\ g^{-1}$	415.45	776.23	534.08	826.2
S_{ext} / $m^2\ g^{-1}$	89,17	101.21	75.92	152.2
S_{mic} / $m^2\ g^{-1}$	326.28	675.02	458.16	674
$d_p = 4V_{tot}/S$ in Å	26.13	17.25	21.32	17.85
pH_{PZC}	5.1	4.25	4	3.9
q_e / mg g^{-1}	34.45	63.66	75.39	80.46

Morphological characterization of the ACs

The scanning electron micrographs (SEM) of the non-activated carbon (non-AC 0 %) and the AC 75 % are presented in Fig. 2a and b. The non-activated carbon (0 % H_3PO_4) and activated carbon (75 % H_3PO_4) samples derived from the polyester precursor show visible signs of fibers collapse and breakage, likely due to an intensified reaction with the polyester caused by the acid in the impregnation stage and the pyrolysis temperature, with the woven form of the precursor is gone. Unlike carbon prepared from cotton, it has kept its woven and fibrous character,[3] the polyester-derived carbon lost this structure.

It is also noticed that the porous structure (size of the pores) is well-developed, containing different sizes and shapes of pores which result from the activation process.

FTIR analysis

The FTIR spectra of the ACs prepared with different ratios (0, 25, 50 and 75 %) are presented in Fig. 3. It is noted that the spectra corresponding to the different adsorbents are similar with respect to the type of functional groups. The difference

is only in the intensity of the peaks. The higher the activation rate, the more intense the peaks. Examination of all these spectra reveals the following absorption bands.

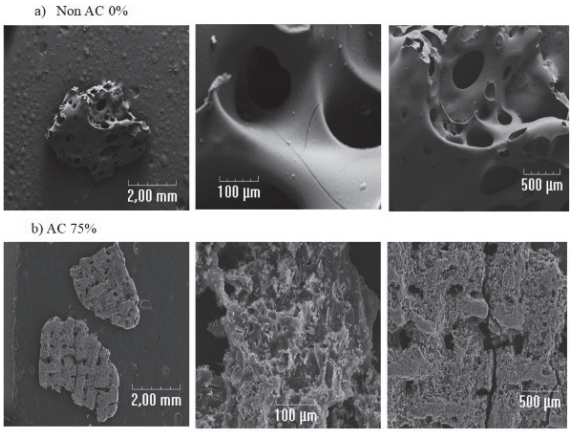

Fig. 2. SEM micrographs of: a) the non-activated carbon (0 % H_3PO_4) and b) the activated carbon (75 % H_3PO_4).

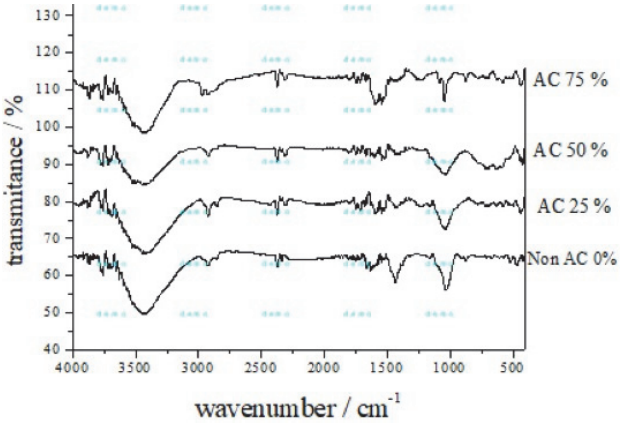

Fig. 3. FTIR spectra of the carbon.

A broad absorption band observed between 3600–3300 cm^{-1} with a maximum around 3400 cm^{-1} is characteristic of the hydrogen elongation vibration of hydroxyl groups (of carboxyls, phenols or alcohols) and water adsorbed by the materials analyzed.[16]

The peaks at approximately 2300 and 2370 cm^{-1} are characteristic of the C≡C stretching vibration of alkyne groups.[17]

The new band appearing in the AC 25 %, AC 50 % and AC 75 % around 1715 and 1600 cm^{-1} absent on the spectrum of non-AC 0 %, is most likely due to the

C=O indicating the formation of carbonyl-containing groups (ketones, aldehydes, lactones, and carboxyl groups).[18]

The peak at 1556 cm^{-1} is characteristic of the C=O stretch of the carbonyl group in a quinone and represents the γ-pyrone structure with strong vibrations from a combination of C=O and C–C.[19]

The broad band at 1300–500 cm^{-1} was assigned to the C–O stretching and O–H bending modes such as phenols, alcohols, esters and carboxylic acids.[20]

The presence of hydroxyl groups of phenolic and carboxylic acids gives an acidic character to the activated carbon surface whereas carbonyl and quinone groups confer a basic character to the adsorbent surface.

The pH_{PZC} (Table I) shifted towards lower pH values when the impregnation ratio increased due to the introduction of acidic groups.

Effect of impregnation ratio on adsorption amount of clofibric acid

The impregnation ratio variation effect on the adsorption kinetics of the CA onto activated carbon is presented in Table I. A higher elimination of CA is observed when the impregnation ratio is increased from 0 to 75 % H_3PO_4. The best adsorption rate (% removal) of activated carbon obtained at 75 % phosphoric acid was 80.46 mg g^{-1}. This may be attributed to the increase in adsorbent surface area, microporosity development (≈ 99 %) and availability of more adsorption sites resulting from the increase in impregnation ratio. Consequently, the activated carbon prepared with an activation ratio of 75 % H_3PO_4 was used in all subsequent experiments.

Effect of pH on the removal of clofibric acid

pH is an important factor in any adsorption study. It can condition both the surface charge of the adsorbent and the structure of the adsorbate. This quantity characterizes the water, and its value will depend on the origin of the effluent. The treatment technique to be adopted will strongly depend on the pH value. This is the reason why, in any adsorption study, the influence of pH on the adsorption capacity of a given solute on a specific adsorbent is essential.

The kinetic results of the adsorption of clofibric acid showed that the pH studied in the range 3–9 is a critical factor. From Fig. 4a, it appears that CA elimination is best at a very acidic pH (pH 3). The adsorption capacity gradually decreases when the pH increases. It reaches its minimum at basic pH (pH 9). A similar value was found in a previous study on the adsorption of clofibric acid by an activated carbon prepared from cotton[3].

The pH_{PZC} of AC 75 % is 3.9; thus, the surface carries a positive charge at solution pH values less than 3.9, is neutral for pH = pH_{PZC} and is negative for solution pH values above 3.9.

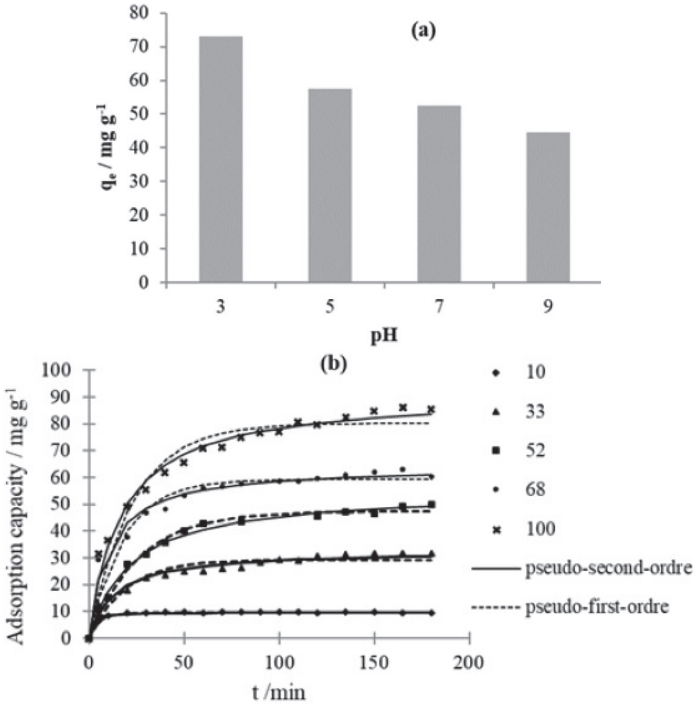

Fig. 4. Adsorption of CA onto AC 75 % at different: a) initial pH; conditions: AC 75 %, agitation speed = 360 rpm and T = 20 °C and b) contact time and initial CA concentration; conditions: AC 75 %, agitation speed = 360 rpm; T = 20 °C and pH 3.

The increase of the CA adsorption capacity with increasing the acidic degree of the solution is attributed to the anionic and molecular forms of the CA and the positive surface charge of the activated carbon at lower pH. Therefore, the anionic form of CA is attracted by the positive charges of the activated carbon surface area. When the pH increases (pH > pH_{PZC}), the surface becomes more negatively charged and above the pKa value clofibric acid is in the anionic form. This results in high electrostatic repulsions, leading to no significant adsorption.

Effect of contact time and initial clofibric acid concentration

One of the factors known to influence the amount of solute removed by adsorption is the adsorbent–adsorbate contact time. Therefore, we have monitored the CA adsorption capacity over a period of 3 h for different initial acid concentrations.

Fig. 4b indicates that equilibrium is almost reached after 60 min. It also shows that the adsorption takes place in two stages. At the start of the experiment, adsorption is rapid, which is due to the high availability of vacant active sites on the surface of the adsorbent. This step is followed by a second, slower step as there are fewer and fewer active sites to which clofibric acid can bind. The acid adsorption

capacity tends to stabilize, which is evidenced by the appearance of a plateau. Given these results, we set the duration of our experiences to 180 min to make sure there is no desorption of adsorbed molecules at contact times.

The influence of initial CA concentration on the adsorption capacity and kinetics is shown in Fig. 4b. The results show that the CA adsorption capacity increases with increasing initial solution concentration. This development can be explained by the existence of a strong gradient in the concentration of CA between the solution and the surface of the adsorbent when C_0 increases.

Adsorption kinetics

In order to examine the mechanism of the adsorption process, several models are given in the literature. We have tested three kinetic models in particular to analyze our experimental results: the pseudo-first-order model (Eq. (2)), the pseudo-second-order model (Eq. (3)) and the intra-particle diffusion model (Eq. (4)):[3]

$$q_t = \mathrm{q_e}(1 - e^{-k_1 t}) \tag{2}$$

$$q_t = \frac{q_\mathrm{e}^2 k_2 t}{1 + q_\mathrm{e} k_2 t} \tag{3}$$

$$q_t = x_\mathrm{i} + k_\mathrm{d} t^{0.5} \tag{4}$$

where q_e and q_t (mg g^{-1}) are the adsorption capacity at equilibrium and at time t, respectively, k_1 (min^{-1}), k_2 (g mg^{-1} min^{-1}) and k_d (g mg^{-1} min^{-1}) are the rate constant of the pseudo-first-order, pseudo-second-order and intra-particular diffusion equations, respectively and x_i is the intercept of the straight line which is related to the boundary-layer thickness.

All the constants of the models tested (Table II) were determined by maximizing the error function and using the solver add-in with Microsoft's spreadsheet, Microsoft Excel.[21] The error function (coefficient of determination, R^2) employed was defined as follows:

$$R^2 = \frac{\sum (q_\mathrm{cal} - \overline{q_t})^2}{\sum (q_\mathrm{cal} - \overline{q_t})^2 + \sum (q_\mathrm{cal} - q_t)^2} \tag{5}$$

where q_cal and q_t both expressed in mg g^{-1}, represent the adsorption capacities of clofibric acid (CA) onto AC 75 % at time t. q_cal is obtained from the model, while q_t is determined experimentally. $\overline{q}_t$ denotes the average of the experimental values (q_t).

According to Fig. 4b and the values of the parameters presented in Table II, based on the high R^2 and the difference between $q_{\mathrm{e(cal)}}$ and $q_{\mathrm{e(exp)}}$ values, the adsorption kinetics of CA onto AC 75 % is described by a pseudo-second-order

model. The matching adsorption process to the pseudo-second-order model indicates that various mechanisms such as chemisorption and diffusion into the pores contribute to the adsorption of CA onto active sites of the adsorbent.[22]

TABLE II. Kinetic parameters for adsorption of CA onto AC 75 %; k_{d1} and k_{d2} in g mg^{-1} min^{-1}

Initial		Pseudo-first-order kinetics			Pseudo-second-order kinetics		
C_0 mg L^{-1}	$q_{e\,exp}$ mg g^{-1}	$q_{e\,cal}$ mg g^{-1}	k_1 L min^{-1}	R^2	$q_{e\,cal}$ mg g^{-1}	k_2 g mg^{-1} min^{-1}	R^2
100	80.88	80.16	0.04	0.95	81	0.0007	0.98
68	59.37	59.21	0.056	0.94	58.85	0.0016	0.97
52	46.34	47.45	0.038	0.991	46.03	0.0008	0.994
33	30	29.33	0.05	0.93	30.04	0.002	0.97
10	9.6	9.56	0.21	0.996	9.62	0.07	0.999

Intra-particle diffusion				
C_0 / mg L^{-1}	k_{d1}	R^2	k_{d2}	R^2
100	7.24	0.99	2.84	0.95
70	4.95	0.98	1.06	0.80
50	6.19	0.98	1.25	0.93
30	2.36	0.99	1.28	0.96
10	2.7	0.99	0.014	0.048

Fig. S-1 of the Supplementary material to this paper shows two distinct linear segments, indicating a two-step adsorption process. The first linear portion corresponds to adsorption on the external surface (film diffusion), which is considered a fast step. The second portion is attributed to intra-particle diffusion, representing a slower phase of the adsorption process. The analysis of the intra-particle diffusion model (Table II) demonstrated that this diffusion is not the rate-limiting mechanism, and that diffusion through the boundary layer surrounding the adsorbent plays a non-negligible role.

Adsorption isotherms

Isotherms comprise an essential part of adsorption studies. From them, it is possible to evaluate the physical interactions between adsorbate and adsorbent.[23]

In the present study, the Langmuir and Freundlich models (Table III) were tested by using the non-linear method to evaluate the adsorption capacity of our adsorbent and to determine the equilibrium isotherm. Fig. 5 shows the experimental data for the adsorption of CA on AC 75 % at different temperatures and the predicted equilibrium curves.

The adsorption isotherms obtained (Fig. 5) have a similar appearance and correspond to type L, according to the classification of Giles *et al.*[24] This type of isotherm suggests that the molecules adsorb flat on the surface of the adsorbent, and that there is no competition between clofibric acid and water molecules for the adsorption sites.

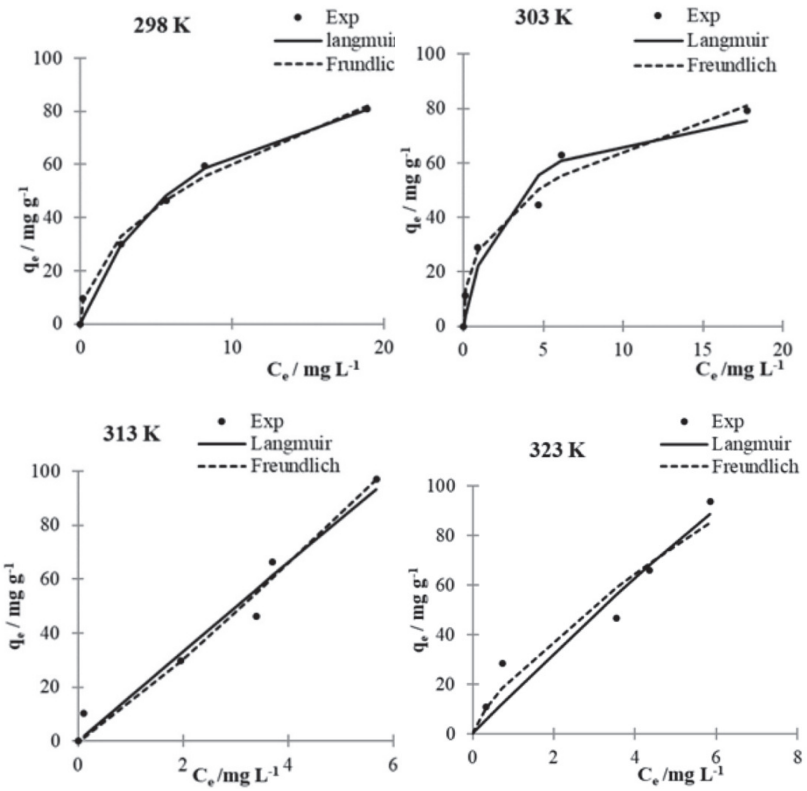

Fig. 5. Langmuir and Freundlich isotherms for the adsorption of CA onto AC75 % (conditions: 0.25 adsorbent, 250 mL of adsorbate solution, adsorption time 180 min, agitation speed 360 rpm, pH 3 and temperature 293–323 K).

It can be deduced (Fig. 5 and Table III) that the equilibrium data are well described by the Freundlich isotherm model.[25] The fitting results show that the value of n is superior to 2 at the temperatures of 293 and 303 K, indicating that the adsorption is good, while at 313 (n = 0.9) and 323 K (n = 1.36) adsorption is poor and moderately difficult, respectively.

A comparison is made between the adsorption capacity of AC 75 % for the removal of the pharmaceutical compound (CA) and other adsorbents reported in the literature. Mestre *et al.*[26] studied the adsorption of clofibric acid (pK_a 3.6) from aqueous solutions using two activated carbons derived from cork waste: CAC (chemically activated with K_2CO_3) and CPAC (physically activated from CAC *via* steam treatment). Textural analyses showed that CAC is predominantly microporous, with 68 % of its microporous volume consisting of narrow mesoporosity. CPAC had the highest specific surface area (1060 m^2 g^{-1}) and total porosity. Kinetic data were modeled using a pseudo-second-order kinetic model. The study demonstrated that pH significantly influenced clofibric acid adsorption, with peak

efficiency at pH 2, followed by progressive declines at pH 3.6 and 5. The sigmoidal adsorption isotherms were fitted with the Dubinin–Astakhov model, revealing a maximum adsorption capacity of 295 mg g^{-1} for CPAC.

TABLE III. Parameters of the Langmuir and Freundlich models for the adsorption of CA onto ACC 75 %; q_m = maximum adsorption capacity; K_L = Langmuir constant; K_F and n = Freundlich constants

Model	Ref.	Parameter	293 K	303 K	313 K	323 K
Langmuir	19	q_m / mg g^{-1}	112.71	86.94	3868	803.66
$q_t = \frac{q_m K_L C_e}{1 + K_L C_e}$		K_L / L mg^{-1}	0.132	0.38	0.004	0.02
		R^2	0.98	0.95	0.96	0.94
Freundlich	19	K_f / $mg^{-1/n}$ $L^{1/n}$	20.75	28.94	13.95	23.25
$q_e = K_L C_e^{1/n}$		$1/n$	0.47	0.36	1.11	0.73
		N	2.22	2.77	0.9	1.36
		R^2	0.99	0.97	0.97	0.95

Roza *et al.*[27] investigated the comparative adsorption behavior of ibuprofen (IBP) and clofibric acid (CA) onto activated carbon derived from bamboo waste, prepared by chemical activation with $ZnCl_2$ followed by microwave heating (ABW). Textural analyses revealed that ABW exhibits a porous structure combining micropores and mesopores (type II isotherm with a low-pressure hysteresis loop), and a specific surface area of 722.27 m^2 g^{-1}. The adsorption of both compounds was more effective under acidic conditions, particularly at pH values between 2 and 5, due to favorable electrostatic interactions. The adsorption kinetics followed a pseudo-second-order model, suggesting that the process is governed by both chemical adsorption and intraparticle diffusion. The adsorption isotherms were best described by the Langmuir model, indicating monolayer adsorption, with maximum adsorption capacities of 278.55 mg g^{-1} for IBP and 229.35 mg g^{-1} for CA. The calculated Gibbs energy changes (–6.15 kJ mol^{-1} for IBP and –5.56 kJ mol^{-1} for CA) indicate that the adsorption processes are spontaneous and thermodynamically favorable.

Lu *et al.*[28] studied the adsorption and removal of clofibric acid (CA) and diclofenac (DCF) from water using a magnetic ion exchange (MIEX) resin. Adsorption was found to be optimal within a pH range of 5 to 9, where both compounds predominantly exist in their anionic forms, thus favoring their exchange with the quaternary ammonium groups on the resin. The kinetic data primarily fit the pseudo-first-order model, and the study revealed that the process is jointly controlled by external mass transfer and surface diffusion. The maximum adsorption capacities reported were 133.69 mg g^{-1} for CA and 322.31 mg g^{-1} for DCF.

Hasan *et al.*[29] investigated the removal of clofibric acid (CA) from water by adsorption using metal–organic frameworks (MOFs), particularly MIL-101, which they compared to activated carbon. MIL-101 exhibited a higher maximum adsorption

capacity (312 mg g^{-1} *versus* 244 mg g^{-1} for activated carbon), which was attributed to its high specific surface area (~3100 m^2 g^{-1}) and well-developed porosity. The adsorption process followed a pseudo-second-order kinetic model, with equilibrium reached more rapidly using MIL-101 than with the other adsorbents. Furthermore, the adsorption was strongly pH-dependent: it was more effective under acidic conditions, suggesting a favorable electrostatic interaction between the anionic functional groups of CA and the cationic sites of the MOF.

A detailed comparison of all the discussed adsorbents is presented in Table S-I of the Supplementary material.

CONCLUSION

This study demonstrated that polyester textile waste can be effectively valorized into high-performance adsorbent materials for the removal of the pharmaceutical pollutant, clofibric acid, present in wastewater. The adsorbent obtained through chemical activation with phosphoric acid (H_3PO_4) followed by pyrolysis at 600 °C resulted in a microporous activated carbon with a high specific surface area (up to 826 m^2 g^{-1} for a 75 % impregnation ratio). Textural analyses (type I isotherms) and morphological characterizations (SEM) confirmed the dominance of microporosity, while FTIR spectroscopy revealed the presence of functional groups (C=O, –OH) that enhance adsorption.

Adsorption tests showed:

– a removal efficiency greater than 95 % for low CA concentrations (10 mg L^{-1}),

– adsorption kinetics described by the pseudo-second-order model, indicating chemisorption-type interactions,

– optimal adsorption at pH 3, highlighting the importance of the carbon surface charge and the ionic form of the pollutant,

– equilibrium data well-fitted by the Freundlich isotherm model, suggesting heterogeneous adsorption on various types of sites and

– the most efficient sample corresponded to an impregnation ratio of 75 % H_3PO_4, for which the maximum measured adsorption capacity reached 80.46 mg g^{-1}.

From an environmental perspective, this research offers an economical and sustainable solution for managing textile waste and treating water contaminated with pharmaceutical compounds. The produced ACs show promising potential for large-scale applications, particularly in hospital or industrial wastewater treatment.

SUPPLEMENTARY MATERIAL

Additional data and information are available electronically at the pages of journal website: https://www.shd-pub.org.rs/index.php/JSCS/article/view/13381, or from the corresponding author on request.

ИЗВОД

АДСОРПЦИЈА КЛОФИБРИНСКЕ КИСЕЛИНЕ АКТИВНИМ УГЉЕМ ДОБИЈЕНИМ ОД ОТПАДНЕ ПОЛИЕСТЕРСКЕ ТКАНИНЕ: ИСПИТИВАЊЕ ЕКСПЕРИМЕНТАЛНИХ ПАРАМЕТАРА, КИНЕТИЧКЕ И АДСОРПЦИОНЕ РАВНОТЕЖЕ ПРИМЕНОМ НЕЛИНЕАРНЕ МЕТОДЕ

NASSIMA BOUDRAHEM-BOUALIT[1,2,3], NABIL MAMERI[3] и MOUNA CHALA[1]

[1]Laboratoire des Sciences et Techniques de l'Environnement, Ecole Nationale Polytechniques Alger, Avenue Pasteur El Harrach, 16110 Alger, Algeria, [2]Faculté de Technologie, Université de Bejaia, Bejaia 06000, Algéria и [3]Laboratoire de biotechnologie, Ecole Nationale Polytechniques Alger, Avenue Pasteur El Harrach, 16110 Alger, Algerie

Предмет овог истраживања је студија изводљивости припреме адсорбената од текстилног отпада (полиестера) за уклањање фармацеутских производа као што је клофибринска киселина (CA). Резултати су показали да су адсорбенти припремљени хемијском активацијом у присуству фосфорне киселине, а затим пиролизом на 600 °C, микропорозни материјали са великим специфичним површинама. Испитан је утицај времена контакта, почетне концентрације КА, pH раствора и температуре на адсорпцију. Проценти уклањања КА из воденог раствора адсорпцијом већи од 95 % добијени су у случају разблажених раствора (10 mg L^{-1}) на собној температури и при pH 3. Кинетика адсорпције је успешно описана моделом псеудо-другог реда, а добијени изотерме су Фројндлиховог типа. Резултати указују да је овај процес спонтан, ефикасан и потенцијално применљив у уклањању CA из воде.

(Примљено 15. маја, ревидирано 25. јуна, прихваћено 6. августа 2025)

REFERENCES

1. A. V. Dordio, C. Duarte, M. Barreiros, A. J. P. Carvalho, A. P. Pinto, C. T. da Costa, *Bioresour. Technol.* **100** (2009) 1156 (http://doi.org/10.1016/j.biortech.2008.08.034)
2. V. Rakić, V. Rac, M. Krmar, O. Otman, A. Auroux, *J. Hazard. Mater.* **282** (2015) 141 (http://doi.org/10.1016/j.jhazmat.2014.04.062)
3. N. Boudrahem, F. Aissani-Benissad, F. Boudrahem, C. Vial, F. Audonnet, L. Favier, *Water Sci. Technol.* **82** (2020) 2513 (http://doi.org/10.2166/wst.2020.524)
4. M. E. Ramos, P. R. Bonelli, S. Blacher, M. M. L. Ribeiro Carrott, P. J. M. Carrott, A. L. Cukierman, *Colloids Surfaces, A* **378** (2011) 87 (http://doi.org/10.1016/j.colsurfa.2011.02.005)
5. Y. Sun, Q. Yue, B. Gao, Q. Li, L. Huang, F. Yao, X. Xu, *J. Colloid Interface Sci.* **368** (2012) 521 (http://doi.org/10.1016/j.jcis.2011.10.067)
6. A. C. Pastor, F. Rodríguez-Reinoso, H. Marsh, M. A. Martínez, *Carbon* **37** (1999) 1275 (http://doi.org/10.1016/S0008-6223(98)00324-8)
7. C. F. Brasquet, B. Bourges, P. L. Cloirec, *Environ. Sci. Technol.* **33** (1999) 4226 (https://doi.org/10.1021/es981358m)
8. C. F. Brasquet, P. L. Cloirec, *Langmuir* **15** (1999) 5906 (https://doi.org/10.1021/la9811160)
9. E. Ayranci, O. Duman, *J. Hazard. Mater.* **124** (2005) 125 (https://doi.org/10.1016/j.jhazmat.2005.04.020)
10. J. R. Rangel-Mendez, M. Streat, *Water Res.* **36** (2002) 1244 (https://doi.org/10.1016/S0043-1354(01)00343-8)
11. M. A. Álvarez-Merino, V. López-Ramón, *J. Colloid Interface Sci.* **288** (2005) 335 (https://doi.org/10.1016/j.jcis.2005.03.025)

12. F. Akkouche, F. Boudrahem, I. Yahiaoui, C. Vial, F. Audonnet, F. Aissani-Benissad, *Water Environ. Res.* **39** (2021) 464 (https://doi.org/10.1002/wer.1449)
13. L. Khenniche, F. Aissani, *J. Chem. Eng. Data* **55** (2010) 728 (http://doi.org/10.1021/je900426a)
14. Y. Guo, D. A. Rockstraw, *Carbon* **44** (2006) 1464 (http://doi.org/10.1016/j.carbon.2005.12.002)
15. M. E. Ramos, P. R. Bonelli, A. L. Cukierman, *Colloids Surfaces A* **324** (2008) 86 (https://doi.org/10.1016/j.colsurfa.2008.03.034)
16. Y. Chen, S. R. Zhai, N. Liu, Y. Song, Q. Da An, X. W. Song, *Bioresour. Technol.* **144** (2013) 401 (http://doi.org/10.1016/j.biortech.2013.07.002)
17. I. I. Gurten, M. Ozmak, E. Yagmur, Z. Aktas, *Biomass Bioenergy* **37** (2012) 73 (https://doi.org/10.1016/j.biombioe.2011.12.030)
18. K. Y. Foo, B. H. Hameed, *Chem. Eng. J.* **180** (2012) 66 (http://doi.org/10.1016/j.cej.2011.11.002)
19. J. Zheng, Q. Zhao, Z. Ye, *Appl. Surf. Sci.* **299** (2014) 86 (http://doi.org/10.1016/j.apsusc.2014.01.190)
20. S. M. Yakout, G. Sharaf El-Deen, *Arab. J. Chem.* **9** (2016) S1155 (http://doi.org/10.1016/j.arabjc.2011.12.002)
21. N. Boudrahem, S. Delpeux-Ouldriane, L. Khenniche, F. Boudrahem, F. Aissani-Benissad, M. Gineys, *Process Saf. Environ. Prot.* **111** (2017) 544 (http://doi.org/10.1016/j.psep.2017.08.025)
22. K. Yahiaoui, F. Boudrahem, S. Ziani, I. Yahiaoui, F. Aissani-Benissad, *Int. J. Environ. Anal. Chem.* **102** (2022) 6670 (http://doi.org/10.1080/03067319.2020.1814272)
23. P. Del Vecchio, N. K. Haro, F. S. Souza, N. R. Marcílio, L. A. Féris, *Water Sci. Technol.* **79** (2019) 2013 (http://doi.org/10.2166/wst.2019.205)
24. C. H. Giles, T. H. MacEwan, S. N. Nakhwa, D. Smith, *J. Chem. Soc.* **846** (1960) 3973 (http://doi.org/10.1039/JR9600003973)
25. F. Boudrahem, F. Aissani-Benissad, A. Soualah, *Desalin. Water Treat.* **54** (2015) 1727 (http://doi.org/10.1080/19443994.2014.888686)
26. A. S. Mestre, M. L. Pinto, J. Pires, J. M. F. Nogueira, A. P. Carvalho, *Carbon* **48** (2010) 972 (http://doi.org/10.1016/j.carbon.2009.11.013)
27. R. A. Reza, M. Ahmaruzzaman, A. K. Sil, V. K. Gupta, *Ind. Eng. Chem. Res.* **53** (2014) 9331 (http://doi.org/10.1021/ie404162p)
28. X. Lu, Y. Shao, N. Gao, J. Chen, Y. Zhang, Q. Wang, Y. Lu, *Chemosphere* **161** (2016) 400 (http://doi.org/10.1016/j.chemosphere.2016.07.025)
29. Z. Hasan, J. Jeon, S. H. Jhung, *J. Hazard. Mater.* **209**–**210** (2012) 151 (http://doi.org/10.1016/j.jhazmat.2012.01.005).

Journal of the Serbian Chemical Society
JSCS-info@shd.org.rs • www.shd.org.rs/JSCS
J. Serb. Chem. Soc. 91 (5) S151–S152 (2026)
Supplementary material

SUPPLEMENTARY MATERIAL TO

Adsorption of clofibric acid on the activated carbon prepared from polyester cloth waste: Study of the operational parameters, kinetics and adsorptive equilibrium using the non-linear method

NASSIMA BOUDRAHEM-BOUALIT[1-3]*, NABIL MAMERI[3] and MOUNA CHALA[1]

[1]Laboratoire des Sciences et Techniques de l'Environnement, Ecole Nationale Polytechniques Alger, Avenue Pasteur El Harrach, 16110 Alger, Algeria, [2]Faculté de Technologie, Université de Bejaia, Bejaia 06000, Algeria and [3]Laboratoire de biotechnologie, Ecole Nationale Polytechniques Alger, Avenue Pasteur El Harrach, 16110 Alger, Algeria

J. Serb. Chem. Soc. 91 (5) (2026) 529–543

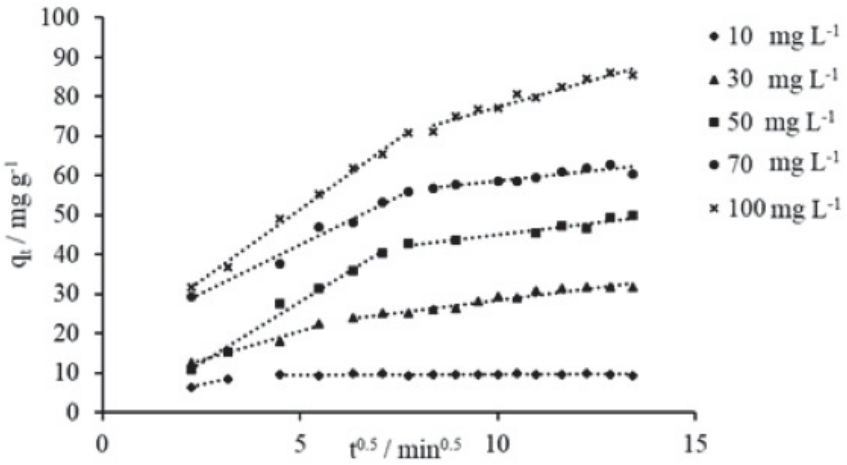

Fig. S-1. Kinetics intra-particle diffusion of CA adsorption on AC 75% with different initial concentrations. Conditions: AC 75%, pH = 3, agitation speed = 360 rpm and T = 20 °C.

* Corresponding author. E-mail: nassima.boudrahem@g.enp.edu.dz

TABLE S-I. Comparison of adsorption capacities for the removal of CA from aqueous solutions using other adsorbents.

Study	Adsorbent used	Preparation / activation	S_{BET} (m^2g^{-1})	Optimal pH	Kinetic model	Isotherm model	q_{max} (mg g^{-1})	Remarks
Present study	Activated carbon from polyester textile waste	H_3PO_4 activation + pyrolysis at 600 °C	826	3	Pseudo-second order	Freundlich	80.46	Low-cost, sustainable solution, high efficiency at low conc.
Mester et al. [26]	CAC, CPAC	Cork waste + K_2CO_3 (chemical) / steam (physical)	1060 (CPAC)	2	Pseudo-second order	Dubinin–Astakhov	295	High-performance materials, large adsorption capacity
Roza et al.[27]	Bamboo-based activated carbon (ABW)	$ZnCl_2$ activation + microwave heating	722.27	2-5	Pseudo-second order	Langmuir	229.35	Micro-/mesoporous structure, monolayer adsorption, high capacity
Lu et al.[28]	MIEX resin (ion exchange)	Synthesized magnetic resin	Not specified	5-9	Pseudo-first order	Langmuir	133.69	Ion exchange mechanism, good performance at neutral/basic pH
Hasan et al.[29]	Metal-Organic Framework (MIL-101)	MOF synthesis	3100	< 5	Pseudo-second order	Langmuir	312	Highly efficient material, but costly and complex to produce

Journal of the Serbian Chemical Society
JSCS-info@shd.org.rs • www.shd.org.rs/JSCS
J. Serb. Chem. Soc. 91 (5) 545–556 (2026)
JSCS–5508
Original scientific paper
Published 12 June, 2026

Pharmaceuticals in Belgrade's wastewater: Impact on surface waters and environmental risk assessment

LJILJANA M. TOLIĆ STOJADINOVIĆ[1]*, SVETLANA D. GRUJIĆ[2], NIKOLINA N. ANTIĆ[3] and TATJANA M. ĐURKIĆ[2]

[1]Innovation Centre of the Faculty of Technology and Metallurgy, Karnegijeva 4, 11000 Belgrade, Serbia, [2]University of Belgrade, Faculty of Technology and Metallurgy, Karnegijeva 4, 11000 Belgrade, Serbia and [3]Customs laboratory, Customs Administration of the Republic of Serbia, Bulevar Zorana Đinđića 155a, 11000 Belgrade, Serbia

(Received 26 May, revised 16 June, accepted 3 December 2025)

Abstract: In the Belgrade region, direct discharges of untreated wastewater into the Sava and Danube rivers have a detrimental impact on water quality. This study investigates this impact by examining the presence of pharmaceuticals in Belgrade's wastewater and corresponding surface water, alongside the associated environmental risk. A highly sensitive and selective LC–MS/MS method was developed, validated and applied to the analysis of water samples. Thirteen out of seventeen target pharmaceuticals were detected in wastewater, while nine compounds were found in surface water, with diclofenac reaching the highest concentration (1.1 μg L^{-1}). Metoprolol, carbamazepine and diclofenac were the most prevalent in both wastewater and surface water samples. Risk assessment indicated that diclofenac and azithromycin posed a high environmental risk (*RQ* > 1), while a mixture toxicity assessment suggested a cumulative hazard at all sampling sites. Additionally, the study evaluated pharmaceutical removal efficiencies in two wastewater treatment plants in Serbia, revealing variable efficiencies and even negative removal rates for some compounds, highlighting the inadequacy of conventional treatment plants in effectively eliminating these substances. The results emphasize the urgency of regulatory actions and the need for adequate treatment technologies to reduce pharmaceutical pollution in aquatic environments.

Keywords: drugs; emerging pollutants; urban wastewater; water quality; WWTP; ecological assessment.

INTRODUCTION

Pharmaceuticals are increasingly recognised as significant environmental contaminants due to their rising production and widespread use, posing potential risks

* Corresponding author. E-mail: ljtolic@tmf.bg.ac.rs
https://doi.org/10.2298/JSC250526088S

to aquatic ecosystems. Municipal sewage discharge is a major source of these contaminants. Pharmaceuticals enter wastewater through multiple pathways: *i*) excretion of parent compounds and metabolites following human consumption; *ii*) improper disposal of unused drugs; *iii*) hospital and healthcare facility discharges; *iv*) pharmaceutical manufacturing effluents.[1–4] These originate either as pharmaceutical waste (unused drugs disposed of through drains) or human metabolites (excreted after therapeutic use). Human excretion is the predominant pathway, with 30–90 % of administered doses excreted as parent compounds or metabolites.[5] Following administration, many pharmaceuticals undergo hepatic metabolism and are conjugated to facilitate excretion. The concern is that certain metabolites may retain or exceed the toxicity and persistence of the parent compounds.[6] However, current environmental risk assessment studies are predominantly focused on parent compounds. Numerous studies have confirmed the widespread occurrence of pharmaceuticals in wastewater and surface waters at concentrations capable of disrupting aquatic organisms and potentially affecting human health.[7–11]

This issue is particularly concerning in the Republic of Serbia, as less than 21 % of the population is connected to wastewater treatment plants (WWTPs).[12] Belgrade, the capital, exemplifies this issue, as it completely lacks treatment facilities, resulting in the direct discharge of raw sewage into the Sava and Danube rivers. Furthermore, existing WWTPs are often insufficient for removing pharmaceuticals,[13] allowing these contaminants to enter surface water, groundwater, and even drinking water.[14–16] Ongoing research is necessary to better understand the fate of pharmaceutical pollutants, their impact on aquatic life, and the potential risks they pose to ecosystem stability.

This study aimed to: *i*) develop and validate a fast, simple, and sensitive liquid chromatography-tandem mass spectrometry (LC–MS/MS) method for the determination of selected pharmaceuticals in wastewater; *ii*) determine the concentrations of selected contaminants in Belgrade urban wastewater directly discharged to the Sava and the Danube rivers, as well as in the corresponding river water; *iii*) assess the environmental risk posed by contaminants detected in river water; *iv*) evaluate the removal efficiency of the analysed pharmaceuticals in two WWTPs. The pharmaceuticals selected for the study are among the most commonly used and/or frequently detected in the investigated area.

EXPERIMENTAL

Chemicals and reagents

High-purity (> 95 %) analytical standards of seventeen selected pharmaceuticals were obtained from domestic pharmaceutical companies (Hemofarm, STADA Group, Vršac, Serbia, and Zorka-Pharma, Šabac, Serbia). These included: antibiotics (trimethoprim, sulfamethoxazole, azithromycin, erythromycin); the drugs for the treatment of cardiovascular diseases (metoprolol, bisoprolol, enalapril, cilazapril, amlodipine, atorvastatin, clopidogrel, simvastatin); anxiolytic

drugs (bromazepam, carbamazepine, lorazepam, diazepam); and one non-steroidal anti-inflammatory drug (diclofenac).

The individual stock standard solutions of pharmaceuticals were prepared in methanol at a concentration of 100 mgL^{-1}. The working standard solutions were prepared by mixing the appropriate amounts of the individual stock standard solutions and diluting them with methanol. All solutions were stored at 4 °C. For the pH adjustment of the water samples, concentrated acetic acid and ammonia were used. All solvents used were HPLC-grade from J.T. Baker (Center Valley, USA) or Sigma–Aldrich, and all reagents were of analytical grade. Deionised water was obtained using the GenPure ultrapure water system (TKA, Niederelbert, Germany).

Sample preparation

In this study, we modified a previously developed sample preparation method[17] for determining pharmaceuticals in surface water and groundwater samples by replacing the methanol–dichloromethane elution solvent with a safer methanol–ethyl acetate mixture. The modified method, briefly described below, was validated for wastewater samples.

Waters (Milford, MA, USA) Oasis hydrophilic–lipophilic balance (HLB, 200 mg/6 mL) cartridges were utilised for the solid-phase extraction (SPE) of wastewater samples. Prior to the SPE procedure, wastewater samples were filtered through < 1μm glass fibre filters (Whatman GmbH, Dassel, Germany). SPE sorbent was preconditioned with 5mL of a methanol–ethyl acetate (1:1) mixture, followed by 5 mL of deionized water and 5mL of deionized water with its pH adjusted to 6.0. The wastewater sample (100 mL), adjusted to pH 6.0, was then passed through the cartridge, and the sorbent was dried by vacuum suction for 10 min. Afterwards, analytes were eluted using 15 mL of a methanol–ethyl acetate (1:1) mixture, and the extract was evaporated under a nitrogen stream and reconstituted in 1 mL with methanol. The extract was filtered through a 0.45 μm polyvinylidene difluoride (PVDF) filter from Roth (Karlsruhe, Germany) and analysed.

LC–MS/MS analysis

Water sample extracts were analysed using LC–MS/MS based on the method developed by Grujić *et al.*,[18] which was further expanded to include drugs for the treatment of cardiovascular diseases, allowing the determination of 17 pharmaceuticals. Briefly, a Surveyor LC system (Thermo Fisher Scientific, Waltham, MA, USA) was used for the separation of the analytes on the reversed-phase Zorbax Eclipse® XDB-C18 column (75 mm×4.6 mm i.d., 3.5 μm particle size; Agilent Technologies, Santa Clara, USA). A pre-column (12.5 mm×4.6 mm i.d., 5 μm particle size; Agilent Technologies, Santa Clara, CA, USA) was installed in front of the separation column. The mobile phase consisted of water (A), methanol (B) and 10 % acetic acid (C). The gradient changed as follows (Fig. S-I, Supplementary material to this paper): 0 min, A 65 %, B 33 %, C 2 %; 12 min, B 98 %, C 2 %; 18 min, B 98 %, C 2 %; 18.01 min, B 100 %. The initial conditions were then re-established and held for 10 min. The flow rate of the mobile phase was 0.5 mL min^{-1}. An aliquot of 10 μL of the final extract was injected into the LC system. The LC system was coupled with an LCQ Advantage quadrupole ion trap mass spectrometer (Thermo Fisher Scientific, Waltham, MA, USA). The electrospray ionization (ESI) technique was used, and all analytes were analyzed in the positive ionization mode. The optimal source parameters were as follows: source voltage (4.5 kV), sheath gas (25 au, *i.e.*, 25 arbitrary units), and capillary temperature (290 °C). Fragmentation reactions used for identification and quantification, as well as the confirmation of selected analytes, are shown in Table S-I (Supplementary material).

The standard addition method was used to analyse the collected wastewater samples, compensating for matrix effects and incomplete analyte extraction. Each water sample was divided into six aliquots: four aliquots were spiked with a working standard solution at concentrations of 50–1000 ng L^{-1}, resulting in final extract concentrations of 5–100 μg L^{-1}, and the remaining two were not spiked.

Method validation

The linearity of the analytical response was studied using the matrix-matched standards (MMS) prepared at five concentration levels (5–100 μg L^{-1}). MMS were prepared by adding working standard solutions of the pharmaceuticals to the blank extracts obtained after the SPE procedure. The extraction recoveries and the repeatability of the method, expressed as the relative standard deviation (R*SD*), were determined by analyzing three replicate wastewater samples spiked at two concentration levels (100 and 1000 ng L^{-1}). The limits of detection (*LOD*s) and quantification (*LOQ*s) were determined as the minimum detectable amount of analyte with a signal-to-noise (*S*/*N*) ratio of 3 and 10, respectively,[19] using spiked samples at a concentration of 50 ng L^{-1}.

Water sample collection

The details related to sample collection are given in Supplementary material.

Risk assessment

The risk quotient (*RQ*) approach was used to assess the environmental risk of pharmaceuticals detected in surface water. Risk quotients were calculated using the equation:

$$RQ = \frac{MEC}{PNEC} \tag{1}$$

where *MEC* is the measured environmental concentration and *PNEC* is the predicted no-effect concentration of the detected compounds.[21] *PNEC* values were obtained from the Norman database,[22] using the lowest available values for each compound (Table S-III, Supplementary material). The risk to aquatic life may increase when pharmaceuticals are present in mixtures, as each compound contributes to toxicity, even if individual concentrations are below their *PNEC* values. Therefore, to fully estimate the risks to aquatic life arising from exposure to pharmaceuticals, the combined effects of their mixtures were considered. Risk at each sampling site was evaluated using the concentration addition concept,[23,24] with RQ_{mix} calculated as:

$$RQ_{mix} = \sum_{i=1}^{n} \frac{MEC_i}{PNEC_i} \tag{2}$$

Based on *RQ* values, the environmental risk was classified as: high ($RQ \geq 1$), medium ($0.1 \leq RQ < 1$), and low ($RQ < 0.1$).[25]

RESULTS AND DISCUSSION

Method validation

The developed analytical method was validated for wastewater samples, with linearity, recovery, repeatability, detection limits and quantification limits assessed (Table S-IV, Supplementary material). Linearity was evaluated using MMS (5––100 μg L^{-1}), corresponding to initial sample concentrations of 50–1000 ng L^{-1}. Determination coefficients (R^2) ranged from 0.990 to 0.999 for all tested analytes,

indicating adequate linearity. The recoveries ranged from 70 to 120 % for most analytes, except for azithromycin and erythromycin (55–62 %), likely due to pH adjustment to 6.0. Our previous study showed that pH values of 3.0 and 7.5 were optimal for azithromycin and erythromycin, respectively.[18] However, pH 6.0 provided the best overall recoveries, making it the most suitable choice for simultaneous analysis. The resulting *RSD* values were all below 20 %. Low limits of detection (3.3–50.0 ng L^{-1}) and quantification (11.1–166.7 ng L^{-1}) were obtained, demonstrating the method's sensitivity, which is in agreement with values reported in the literature[19] and its suitability for determining trace levels of selected analytes in wastewater samples.

Wastewater and surface water sample analysis

The validated method was used to analyse selected pharmaceuticals in urban wastewater samples discharged into the Sava and Danube rivers in Belgrade, as well as in the corresponding surface water. As shown in Table I, 13 out of 17 target pharmaceuticals were detected in urban wastewater, with concentrations ranging from 15 ng L^{-1} (cilazapril) to 1.2 μg L^{-1} (sulfamethoxazole). The most ubiquitous drugs were metoprolol, bisoprolol, enalapril, carbamazepine and diclofenac, detected at all sampling sites, confirming their widespread use and persistence in wastewater. Sampling site WW1 had the highest number of detected compounds (13 out of 17), likely because it is the primary discharge point for Belgrade's wastewater.

TABLE I. Pharmaceuticals detected in Belgrade urban wastewater at seven sampling sites WW1–WW7 (n = 2)

Pharmaceutical	Concentration ± *SD*, ng L^{-1}						
	WW1	WW2	WW3	WW4	WW5	WW6	WW7
Trimethoprim	122±12	53±5	–	–	482±72	–	–
Metoprolol	290±22	154±13	434±58	36±3	305±32	143±20	294±8
Sulfamethoxazole	122±19	122±9	–	–	1184±152	–	–
Azithromycin	318±48	102±0	–	–	–	–	–
Bisoprolol	63±11	46±4	118±22	83±7	49±8	35±4	76±9
Enalapril	155±12	128±26	240±51	284±44	174±17	164±20	208±34
Cilazapril	15±2	89±16	22±4	–	–	–	–
Erythromycin	133±22	266±34	347±22	–	–	–	–
Carbamazepine	274±44	313±30	449±14	263±8	127±25	190±49	253±41
Lorazepam	171±24	84±3	318±19	167±33	77±10	105±22	–
Diazepam	163±22		–	–	–	–	–
Atorvastatin	71±5	25±4	–	–	–	–	–
Diclofenac	442±73	253±11	58±5	471±70	782±156	479±105	310±71

Pharmaceuticals in untreated wastewater have been studied across the Western Balkans, with Petrović *et al.*[9] detecting trimethoprim, sulfamethoxazole, carbamazepine, lorazepam and atorvastatin in Novi Sad at concentrations similar to

ours, with carbamazepine being among the most abundant in both studies. However, diclofenac and metoprolol concentrations were higher in their study, with diclofenac exceeding 1 μg L^{-1}. Terzić *et al.*[26] investigated 44 pharmaceuticals in wastewater from Bosnia and Herzegovina, Croatia and Serbia, reporting a wide concentration range for many compounds. For pharmaceuticals detected in both studies, the concentrations measured in our samples fell within the reported ranges.

In the corresponding surface water samples, 9 out of 17 target pharmaceuticals were detected (Table II), with concentrations ranging from 19 ng L^{-1} (bisoprolol) to 1.1 μg L^{-1} (diclofenac). The most prevalent drugs in the surface water samples were metoprolol, carbamazepine, and diclofenac, detected at all sites. At sampling site SW8, 9 out of 17 substances were detected, with notably higher concentrations, likely due to its location in a small bay with limited water circulation.

TABLE II. Pharmaceuticals detected in Belgrade surface water at eight sampling sites SW1–SW8 (n = 2)

Pharmaceutical	Concentration ± *SD*, ng L^{-1}							
	SW1	SW2	SW3	SW4	SW5	SW6	SW7	SW8
Trimethoprim	145±11	–	–	–	–	–	–	334±54
Metoprolol	95±3	107±13	53±8	308±50	82±14	78±11	132±12	1012±150
Sulfamethoxazole	–	–	–	–	–			127±7
Azithromycin	–	–						58±1
Bisoprolol				33±2			19±2	661±124
Enalapril	–	–	–		–		–	1099±8
Carbamazepine	20±2	20±2	23±1	38±7	24±4	32±5	56±8	552±29
Diazepam	–	–	–	–		–	–	176±18
Diclofenac	316±47	157±2	267±50	225±45	375±75	1087±123	251±50	950±176

In a review paper,[27] the reported concentration ranges of pharmaceuticals in the Lower Danube River basin were: carbamazepine (3.94–945 ng/L), diclofenac (0.8–255 ng/L), sulfamethoxazole (30–204 ng/L) and trimethoprim (0.8–223 ng/L). Our results align with these ranges, except for diclofenac, which showed significantly higher concentrations at two sampling sites. Similarly elevated diclofenac levels were reported in the Danube near Budapest, Hungary (up to 931 ng/L).[28]

In most cases, the same compounds were found in both surface water samples and wastewater discharged into them, indicating the impact of Belgrade's municipal wastewater on surface water quality. The concentrations of most detected compounds were significantly lower in river water. However, for some compounds, such as diclofenac, similar or even higher concentrations were observed in surface water compared with wastewater. The highest detected diclofenac concentration in river water exceeded that observed in wastewater, likely due to its high environmental persistence.[29] Metoprolol, diclofenac and carbamazepine were the most frequently detected analytes in both sample types.

Hazard characterisation of detected pharmaceuticals

Hazard identification was conducted for each detected pharmaceutical according to the REACH/CLP criteria, evaluating five key hazard classes: persistence, bioaccumulation, toxicity, mobility and endocrine disruption.[30] A comprehensive summary of the hazard characterisation for all detected pharmaceuticals is provided in Table S-V (Supplementary material). The hazard assessment revealed that several detected pharmaceuticals exhibited concerning profiles: carbamazepine and erythromycin showed high persistence and toxicity, while azithromycin showed moderate-to-high persistence combined with high toxicity. Multiple pharmaceuticals (metoprolol, sulfamethoxazole, carbamazepine, erythromycin) demonstrated high mobility, raising concerns about their potential for widespread environmental distribution. Additionally, various compounds, including metoprolol, sulfamethoxazole, azithromycin, erythromycin, carbamazepine, lorazepam, diazepam and diclofenac, showed potential endocrine-disrupting activity. These hazard characteristics justify the inclusion of the detected pharmaceuticals in the risk assessment.

Risk assessment

The environmental risk associated with analytes detected in surface water samples was assessed, with the obtained *RQ*s presented in Fig. 2A. Based on the calculated *RQ* values, bisoprolol posed a low risk ($RQ < 0.1$), while most of the other detected analytes posed a moderate risk ($0.1 \leq RQ \leq 1$). However, diclofenac posed a high risk, with *RQ* values exceeding 1 at all sampling sites, reaching a maximum of 27.17 at site SW6. Azithromycin also exceeded the high-risk threshold ($RQ > 1$) at one site ($RQ = 3.05$ at SW8). Both diclofenac and azithromycin have been proposed for inclusion in the EU Priority Substances List in the field of water policy,[31] due to their widespread presence in water bodies and harmful effects on aquatic organisms. Other studies,[32–34] have also reported high risks for these substances, highlighting the need for further attention and regulatory consideration.

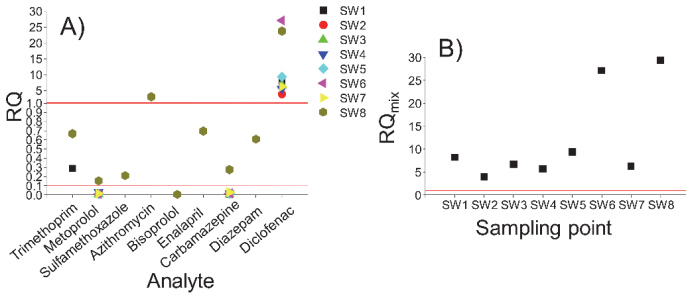

Fig. 2. A) Risk quotients (*RQ*s) for individual compounds at each surface water site; B) risk quotients for the compound mixture (RQ_{mix}) at each site.

The risk of the entire mixture of pharmaceuticals was also assessed at all surface water sampling sites. As shown in Fig. 2B, the RQ_{mix} significantly exceeded the threshold of 1 at all sites, with the highest value of 29.42 observed at site SW8. At this location, as well as at all other sites, diclofenac was the predominant contributor to the high RQ_{mix} value. However, even contaminants that individually do not pose a significant risk can contribute to an increased RQ_{mix} value and as part of a mixture, they may amplify environmental risk due to cumulative effects. These findings emphasise the need to assess the combined effects of contaminant mixtures, rather than focusing solely on individual compounds.

Pharmaceuticals detected in WWTPs and their removal rates

Pharmaceutical concentrations in wastewater samples from the selected WWTPs in Serbia (Table III) showed significant variations in both influent and effluent levels. Among the nine detected pharmaceuticals, the highest influent concentrations were recorded for carbamazepine (2.7 μg L^{-1}) at WWTP1 and diclofenac (5.9 μg L^{-1}) at WWTP2. Generally, influent concentrations exceeded those obtained for untreated wastewater from Belgrade (Table I), particularly for metoprolol, erythromycin and diclofenac. These variations may stem from differences in wastewater composition, such as differences in the proportion of domestic effluents.

TABLE III. Pharmaceuticals detected in influent and effluent samples of two WWTPs in Serbia (n = 2); *RE*: removal efficiency

Pharmaceutical	Concentration ± *SD*, ng L^{-1}		*RE* %	Concentration ± *SD*, ng L^{-1}		*RE* %
	Influent WWTP1	Effluent WWTP1		Influent WWTP2	Effluent WWTP2	
Trimethoprim	37±5	145±7	–292	142±13	109±22	23
Metoprolol	860±77	11630±15	–1252	644±112	3095±12	–381
Sulfamethoxazole	215±24	151±13	30	385±73	107±16	72
Bisoprolol	78±3	73±9	6	89±5	29±2	67
Enalapril	543±55	105±8	81	868±149	399±58	54
Erythromycin	1448±261	520±78	64	956±2	3833±25	–301
Carbamazepine	2675±589	389±62	85	1368±328	529±74	61
Lorazepam	148±2	242±5	–63	188±13	–	100
Diclofenac	1592±143	919±55	42	5927±948	324±35	95

Our results align with other studies reporting carbamazepine concentrations of up to 2150 ng L^{-1} in wastewater in Spain and 2499 ng L^{-1} in China,[35,36] as well as diclofenac levels reaching 4056 ng L^{-1} in Slovenia.[37] In contrast, Afonso-Olivares *et al.*[38] reported lower concentrations of carbamazepine, diclofenac and erythromycin compared with our study, while sulfamethoxazole and trimethoprim were found at higher levels. Differences in consumption patterns may account for regional variations in pharmaceutical concentrations.

All pharmaceuticals detected in influent samples were also present in effluent samples from both WWTPs, except for lorazepam (which was detected in only one effluent), indicating incomplete removal by conventional wastewater treatment. The highest effluent concentrations were observed for metoprolol (11.6 μg L^{-1}) at WWTP1 and erythromycin (3.8 μg L^{-1}) at WWTP2. The removal efficiencies (RE) of pharmaceuticals were evaluated based on influent and effluent concentrations. *RE* varied significantly, ranging from 6 % (bisoprolol) to 85 % (carbamazepine) at WWTP1 and 23 % (trimethoprim) to 100 % (lorazepam) at WWTP2. Gros *et al.*[14] suggested that pharmaceuticals may persist in WWTP effluents due to low adsorption onto activated sludge or slow microbial degradation within the plant's retention time. Consequently, conventional secondary treatment with activated sludge achieves only partial removal, with low *RE* commonly reported for certain pharmaceuticals.[15,39] Additionally, several pharmaceuticals (trimethoprim, lorazepam and metoprolol in WWTP1; erythromycin and metoprolol in WWTP2) exhibited higher concentrations in effluent than in influent samples, resulting in negative *RE*. This phenomenon, documented in other studies,[14,15,37] may result from pharmaceutical retention within the WWTP and subsequent episodic release. Another possible explanation is enzymatic deconjugation of conjugated metabolites, leading to the regeneration of parent compounds during treatment.[40] Despite their similar configurations, the two WWTPs exhibited significant differences in pharmaceutical removal efficiency, which may be explained by differences in process parameters, such as hydraulic retention time and sludge retention time.[41] WWTP2 generally exhibited higher efficiency, particularly in the removal of diclofenac and lorazepam (95 and 100 %, respectively).

Overall, these results suggest that the wastewater treatment processes in the two WWTPs were insufficient to fully eliminate the studied contaminants, highlighting the need for advanced treatment strategies to reduce pharmaceutical contamination in surface waters.

CONCLUSION

This study assessed the presence and impact of pharmaceuticals in Belgrade's wastewater on surface waters, revealing considerable pollution and associated environmental risks. A sensitive and reliable LC–MS/MS method was developed, validated and successfully utilised for pharmaceutical analysis. The most frequently detected pharmaceuticals in wastewater and surface water were metoprolol, carbamazepine and diclofenac, with diclofenac reaching concentrations of up to 1.1 μg L^{-1} in surface water. Risk assessment revealed that diclofenac and azithromycin posed a high environmental risk in surface waters, while the cumulative risk of pharmaceutical mixtures exceeded safety thresholds at all sampling sites. The results from the two conventional wastewater treatment plants (WWTPs) demonstrated variable removal efficiencies, with some pharmaceuticals exhibiting

negative removal rates, suggesting potential issues in the treatment processes. Overall, the study underscores the need for advanced wastewater treatment technologies and regulatory measures to mitigate pharmaceutical contamination and its ecological risks.

SUPPLEMENTARY MATERIAL

Additional data and information are available electronically at the pages of journal website: https://www.shd-pub.org.rs/index.php/JSCS/article/view/13395, or from the corresponding author on request.

Acknowledgement. This work was supported by the Ministry of Science, Technological Development and Innovation of the Republic of Serbia (Contracts No. 451-03-136/2025-03/ /200135 and 451-03-136/2025-03/200287).

ИЗВОД

ЛЕКОВИ У БЕОГРАДСКОЈ ОТПАДНОЈ ВОДИ: УТИЦАЈ НА ПОВРШИНСКЕ ВОДЕ И ПРОЦЕНА ЕКОЛОШКОГ РИЗИКА

ЉИЉАНА М. ТОЛИЋ СТОЈАДИНОВИЋ[1], СВЕТЛАНА Д. ГРУЈИЋ[2], НИКОЛИНА Н. АНТИЋ[3] и ТАТЈАНА М. ЂУРКИЋ[2]

[1]Иновациони центар Технолошко–металуршког факултета, Карнегијева 4, 11000 Београд, [2]Универзитет у Београду, Технолошко–металуршки факултет, Карнегијева 4, 11000 Београд и [3]Царинска лабораторија, Управа царина Републике Србије, Булевар Зорана Ђинђића 155а, 11000 Београд

На подручју Београда, испуштање отпадних вода директно у реке Саву и Дунав има штетан утицај на квалитет вода. Циљ ове студије је процена овог утицаја испитивањем присуства лекова у Београдским отпадним водама и одговарајућим површинским водама, уз процену еколошког ризика. Развијена је и валидирана високо-осетљива и селективана LC–MS/MS метода и примењена на узорке отпадних и површинских вода. Од седамнаест испитиваних лекова, тринаест је детектовано у отпадној води, док је девет пронађено у површинској води, при чему је диклофенак детектован у највишој концентрацији (1,1 μg L^{-1}). Метопролол, карбамазепин и диклофенак су најчешће детектовани у узорцима и отпадне и површинске воде. Процена ризика је показала да диклофенак и азитромицин представљају висок ризик по животну средину ($RQ > 1$), док је процена кумулативног ризика указала да на свим местима узорковања постоји значајан ризик услед присуства мешавине лекова. Додатно, у раду је процењена ефикасност уклањања лекова у два постројења за пречишћавање отпадних вода у Србији, која је указала на променљиву ефикасност, чак и појаву концентрисања појединих лекова, што указује на недостатке конвенционалних постројења у ефикасном уклањању ових супстанци. Ови закључци наглашавају потребу за регулаторним мерама и адекватним техникама третмана у циљу смањења загађења водене средине лековима.

(Примљено 26. маја, ревидирано 16. јуна, прихваћено 3. децембра 2025)

REFERENCES

1. L. Pang, K. He, Y. Zhang, P. Li, Y. Lin, J. Yue, *Sci. Total Environ.* **916** (2024) 170204 (https://doi.org/10.1016/j.scitotenv.2024.170204)
2. S. L. Bartelt-Hunt, D. D. Snow, T. Damon, J. Shockley, K. Hoagland, *Environ. Pollut.* **157** (2009) 786 (https://doi.org/10.1016/j.envpol.2008.11.025)

3. B. I. Escher, R. Baumgartner, M. Koller, K. Treyer, J. Lienert, C. S. McArdell, *Water Res.* **45** (2011) 75 (https://doi.org/10.1016/j.watres.2010.08.019)
4. P. Verlicchi, M Al Aukidy, E. Zambello, *Sci. Tot. Environ.* **429** (2012) 123 (https://doi.org/10.1016/j.scitotenv.2012.04.028)
5. H. P. Rang, M. M. Dale, *Pharmacology*, second edition, Churchill Livingstone, London, 1991, p. 955 (ISBN 10: 0443041105)
6. M. D. Celiz, J. Tso, D. S. Aga, *Environ. Toxicol. Chem.* **28** (2010) 2473 (https://doi.org/10.1897/09-173.1)
7. C. G. Daughton, T. A. Ternes, *Environ. Health Perspect.* **107** (1999) 907 (https://doi.org/10.1289/ehp.99107s6907)
8. T. Heberer, *Toxicol. Lett.* **131** (2002) 5 (https://doi.org/10.1016/S0378-4274(02)00041-3)
9. M. Petrović, B. Škrbić, J. Živančev, L. Ferrando-Climent, D. Barcelo, *Sci. Total Environ.* **468–469** (2014) 415 (http://dx.doi.org/10.1016/j.scitotenv.2013.08.079)
10. F. Hernández, M. Ibáñez, A.-M. Botero-Coy, R. Bade, M. C. Bustos-López, J. Rincón, A. Moncayo, L. Bijlsma, *Anal. Bioanal. Chem.* **407** (2015) 6405 (http://dx.doi.org/10.1007/s00216-015-8796-x)
11. Y. Yu, Z. Wang, B. Yao, Y. Zhou, *Sci. Total Environ.* **923** (2024) 171388 (https://doi.org/10.1016/j.scitotenv.2024.171388)
12. Statistical Office of the Republic of Serbia, *Drinking water supply and urban wastewater*, 2023, Available at: https://publikacije.stat.gov.rs/G2024/HtmlE/G20241134.html (date accessed: May 7, 2025)
13. S. Suárez, M. Carballa, F. Omil, J. M. Lema, *Rev. Environ. Sci. Biotechnol.* **7** (2008) 125 (https://doi.org/10.1007/s11157-008-9130-2)
14. M. Gros, M. Petrović, A. Ginebreda, D. Barceló, *Environ. Int.* **36** (2010) 15 (https://dx.doi.org/10.1016/j.envint.2009.09.002)
15. A.M. Botero-Coy, D. Martínez-Pachón, C. Boix, R.J. Rincón, N. Castillo, L.P. Arias-Marín, L. Manrique-Losada, R. Torres-Palma, A. Moncayo-Lasso, F. Hernández, *Sci. Total Environ.* **642** (2018) 842 (https://doi.org/10.1016/j.scitotenv.2018.06.088)
16. C. O. Okoye, E. S. Okeke, K. C. Okoye, D. Echude, F. A. Andong, K. I. Chukwudozie, H. U. Okoye, C. D. Ezeonyejiaku, *Heliyon* **8** (2022) e09143 (https://doi.org/10.1016/j.heliyon.2022.e09143)
17. T. Radović, S. Grujić, A. Petković, M. Dimkić, M. Laušević, *Environ. Monit. Assess.* **187** (2015) 4092 (https://dx.doi.org/10.1007/s10661-014-4092-z)
18. S. Grujić, T. Vasiljević, M. Laušević, *J. Chromatogr., A* **1216** (2009) 4989 (https://dx.doi.org/10.1016/j.chroma.2009.04.059)
19. K. Tolić Čop, D. Mutavdžić Pavlović, D. Živanić, A. Lakić, M. Runje, *Microchem. J.* **205** (2024) 111283 (https://doi.org/10.1016/j.microc.2024.111283)
20. *Water Supply and Sewage of Belgrade*, Available at: https://www.beograd.rs/lat/gradska-vlast/2144-jkp-beogradski-vodovod-i-kanalizacija_3/ (date accessed: April 24, 2025)
21. European Commission, 2003. *Technical guidance document on risk assessment, Part II,* Available at: https://echa.europa.eu/documents/10162/987906/tgdpart2_2ed_en.pdf/138b7b71-a069-428e-9036-62f4300b752f (date accessed: May 7, 2025)
22. NORMAN Ecotoxicology Database – *Lowest PNECs*, Available at: https://www.norman-network.com/nds/ecotox/lowestPnecsIndex.php (date assessed: May 12, 2023)
23. T. Backhaus, M. Faust, *Environ. Sci. Technol.* **46** (2012) 2564. (https://dx.doi.org/10.1021/es2034125)

24. F. Riva, E. Zuccato, E. Davoli, E. Fattore, S. Castiglioni, *J. Hazard. Mat.* **361** (2019) 103 (https://doi.org/10.1016/j.jhazmat.2018.07.099)
25. M. D. Hernando, M. Mezcua, A. R. Fernández-Alba, D. Barceló, *Talanta* **69** (2006) 334 (https://dx.doi.org/10.1016/j.talanta.2005.09.037)
26. S Terzić, I. Senta, M. Ahel, M. Gros, M. Petrović, D. Barcelo, J. Müller, T. Knepper, I. Martí, F. Ventura, P. Jovančić, D. Jabučar, *Sci. Total Environ.* **399** (2008) 66 (https://dx.doi.org/10.1016/j.scitotenv.2008.03.003)
27. C. L. Chiţescu, A. Ene, E.-I. Geana, A. M. Vasile, C. T. Ciucure, *Appl. Sci.* **11** (2021) 9721 (https://doi.org/10.3390/app11209721)
28. A. Helenkár, Á. Sebö k, Gy. Záray, I. Molnár-Perl, A. Vasanits-Zsigrai, *Talanta* **82** (2010) 600 (https://dx.doi.org/10.1016/j.talanta.2010.05.014)
29. Y. Correa-Navarro, G. López, C. Carazzone, L. Giraldo, J. Moreno-Piraján, *ACS Omega* **8** (2023) 38905 (https://doi.org/10.1021/acsomega.3c03051)
30. European Commission, Commission Delegated Regulation (EU) 2023/707 of 19 December 2022 amending Regulation (EC) No 1272/2008 as regards hazard classes and criteria for the classification, labelling and packaging of substances and mixtures, *Off. J. Eur. Union* **L 93** (2023) 7 (https://eur-lex.europa.eu/eli/reg_del/2023/707/oj)
31. Proposal for a DIRECTIVE OF THE EUROPEAN PARLIAMENT AND OF THE COUNCIL amending Directive 2000/60/EC establishing a framework for Community action in the field of water policy, Directive 2006/118/EC on the protection of groundwater against pollution and deterioration and Directive 2008/105/EC on environmental quality standards in the field of water policy, Available at: https://eur-lex.europa.eu/legal-content/EN/TXT/?uri=celex:52022PC0540 (date accessed: April 9, 2025)
32. O. Solaun, J. G. Rodríguez, I. Menchaca, E. López-García, E. Martínez, B. Zonja, C. Postigo, M. L. de Alda, D. Barceló, Á. Borja, A. Manzanos, J. Larreta, *Sci. Total Environ.* **765** (2021) 142765 (https://doi.org/10.1016/j.scitotenv.2020.142765)
33. O. Solaun, J. G. Rodríguez, Á. Borja, E. López-García, B. Zonjac, C. Postigo, D. Barceló, M. L. de Alda, J. Larreta, *Sci. Total Environ.* **847** (2022) 157563 (http://dx.doi.org/10.1016/j.scitotenv.2022.157563)
34. K. Ng, N. Alygizakis, M.-C. Nika, A. Galani, P. Oswald, M. Oswaldova, Ľ. Čirka, U. Kunkel, A. Macherius, M. Sengl, G. Mariani, S. Tavazzi, H. Skejo, B. M. Gawlik, N. S. Thomaidis, J. Slobodnik, *Water Res.* **230** (2023) 119539 (https://doi.org/10.1016/j.watres.2022.119539)
35. J. L. Santos, I. Aparicio, E. Alonso, *Environ. Int.* **33** (2007) 596 (https://dx.doi.org/10.1016/j.envint.2006.09.014)
36. Y. Zhang, B. Wang, G. Cagnetta, L. Duan, J. Yang, S. Deng, J. Huang, Y. Wang, G. Yu, *Water Res.* **140** (2018) 291 (https://doi.org/10.1016/j.watres.2018.04.056)
37. A. Klančar, J. Trontelj, A. Kristl, M. Zupančič Justin, R. Roškar, *Arh. Hig. Rada. Toksikol.* **67** (2016) 106 (https://dx.doi.org/10.1515/aiht-2016-67-2727)
38. C. Afonso-Olivares, Z. Sosa-Ferrera, J.J. Santana-Rodríguez, *Sci. Total Environ.* **599**–**600** (2017) 934 (http://dx.doi.org/10.1016/j.scitotenv.2017.05.058)
39. C. Lacey, G. McMahon, J. Bones, L. Barron, A. Morrissey, J. M. Tobin, *Talanta* **75** (2008) 1089 (https://dx.doi.org/10.1016/j.talanta.2008.01.011)
40. J. Sipma, B. Osuna, N. Collado, H. Monclús, G. Ferrero, J. Comas, I. Rodriguez-Roda, *Desalination* **250** (2010) 653 (https://doi.org/10.1016/j.desal.2009.06.073)
41. F. Wanner, M. Vana, L. Matousova, J. K. Fuksa, D. Pospichalova, *J. Water Chem. Technol.* **38** (2016) 111 (https://doi.org/10.3103/S1063455X16020090).

Journal of the Serbian Chemical Society
JSCS-info@shd.org.rs • www.shd.org.rs/JSCS
J. Serb. Chem. Soc. 91 (5) S153–S160 (2026)
Supplementary material

SUPPLEMENTARY MATERIAL TO

Pharmaceuticals in Belgrade's wastewater: impact on surface waters and environmental risk assessment

LJILJANA M. TOLIĆ STOJADINOVIĆ[1]*, SVETLANA D. GRUJIĆ[2], NIKOLINA N. ANTIĆ[3] and TATJANA M. ĐURKIĆ[2]

[1]*Innovation Center of the Faculty of Technology and Metallurgy, Karnegijeva 4, 11000 Belgrade, Serbia,* [2]*University of Belgrade, Faculty of Technology and Metallurgy, Karnegijeva 4, 11000 Belgrade, Serbia; and* [3]*Customs laboratory, Customs Administration of the Republic of Serbia, Bulevar Zorana Đinđića 155a, 11000 Belgrade, Serbia*

J. Serb. Chem. Soc. 91 (5) (2026) 545–556

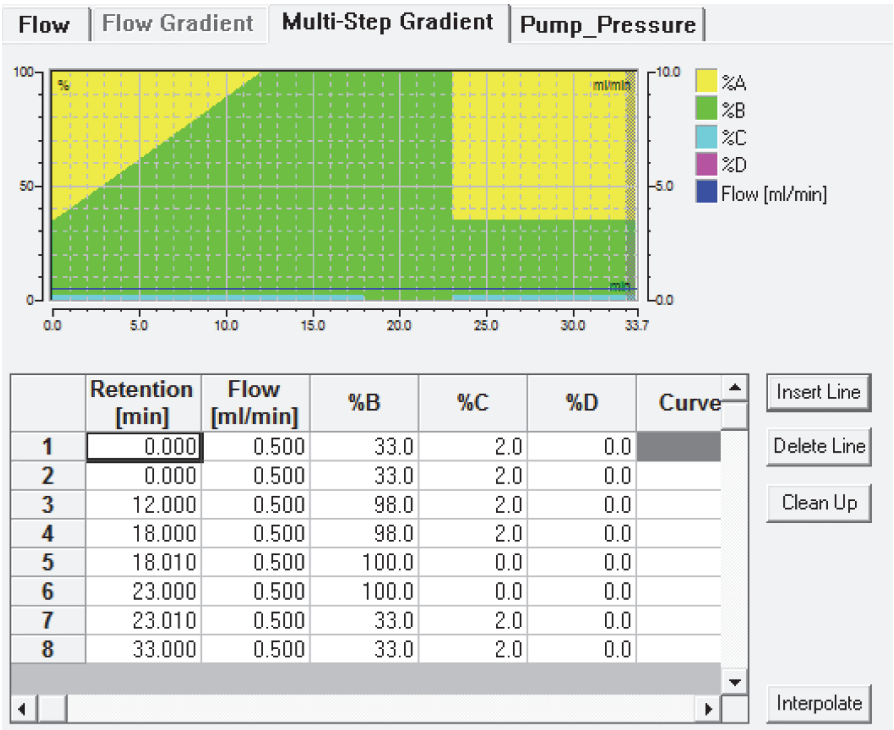

Fig. S-I. Mobile phase gradient profile.

* Corresponding author. E-mail: ljtolic@tmf.bg.ac.rs

Water sample collection

Wastewater and surface water samples were collected in Belgrade, Serbia, near the confluence of the Sava and the Danube rivers (Table S-II). A map with marked sampling sites (WW1–WW7) is shown in Fig. S-1. Wastewater samples were taken at seven discharge points, which handle about 80 % of Belgrade's untreated wastewater. The Belgrade sewage system consists of 212 km of collectors, 1,439 km of pipe network, 32,750 drains and 53,394 sewage connections.[20] Sample WW1 was taken from the largest sewage canal, serving approximately 500,000 inhabitants. Samples were collected over 24 h using automatic samplers and combined into composite samples. Corresponding surface water samples were collected at eight sampling sites downstream of wastewater discharge. Three samples were collected from the Sava river (SW1–SW3, Fig. S-1), four samples from the Danube river (one before the confluence of the two rivers, SW4; three after the confluence, SW6–SW8), and one at the confluence of the Sava and Danube rivers (SW5). Surface water samples were collected by direct sampling from a boat in the middle of the river flow at a depth of about 50 cm. All water samples were collected in 1 L PET bottles and stored at 4 °C until analysis (usually within 1–2 days after sampling). No precipitation occurred on the day of sampling.

Since Belgrade lacks a WWTP, influent and effluent samples were collected from two WWTPs located in small municipalities in Serbia (Sombor, WWTP1, and Velika Plana, WWTP2). The selected WWTPs provide primary and secondary treatment of wastewater using biologically active sludge. WWTP1 has a treatment capacity of 50,000 population equivalents (PE) or 9,300 m^3 day^{-1}, while WWTP2 has a capacity of 35,000 PE. Composite 24 h samples of influent and effluent wastewater were collected at each WWTP using automatic sampling devices. Water samples were stored in 1 L PET bottles and kept frozen without preservatives until preparation for analysis, which occurred a few days after sampling.

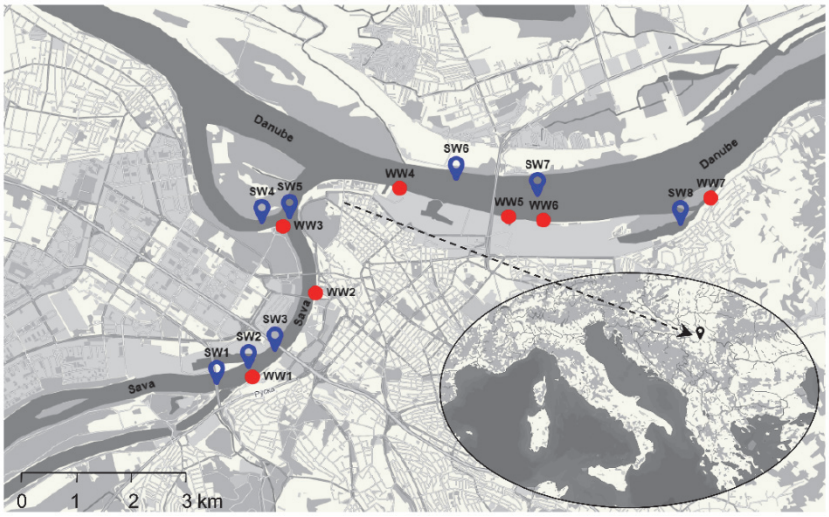

Fig. S-1. Sampling sites of wastewater (WW) and corresponding surface water (SW) in the Sava and the Danube rivers in Belgrade (Serbia).

Table S-I. MS operating parameters for selected pharmaceuticals.

Pharmaceuticals	Precursor ion (*m/z*)	Quantification reaction	Collision energy (%)	Confirmation reaction	Collision energy (%)
Trimethoprim	291 $[M+H]^+$	291→230	44	291→123	44
Metoprolol	268 $[M+H]^+$	268→191	37	268→218	37
Sulfamethoxazole	254 $[M+H]^+$	254→188	34	254→156	34
Azithromycin	749 $[M+H]^+$	749→591	30	591→434	28
Bisoprolol	326 $[M+H]^+$	326→116	31	326→222	31
Enalapril	377 $[M+H]^+$	377→234	30	377→303	30
Cilazapril	418 $[M+H]^+$	418→211	25	211→183	32
Erythromycin	734 $[M+H]^+$	734→576	26	734→716	26
Bromazepam	316 $[M+H]^+$	316→288	36	288→261	35
Amlodipine	409 $[M+H]^+$	409→238	25	409→294	25
Carbamazepine	237 $[M+H]^+$	237→194	34	237→220	34
Lorazepam	321 $[M+H]^+$	321→303	32	303→275	26
Diazepam	285 $[M+H]^+$	285→257	40	257→228	39
Atorvastatin	559 $[M+H]^+$	559→466	25	559→440	25
Diclofenac	296 $[M+H]^+$	296→278	28	278→250	22
Clopidogrel	322 $[M+H]^+$	322→212	28	212→184	23
Simvastatin	419 $[M+H]^+$	419→285	21	419→199	21

Table S-II. The sampling site description.

Sample	Latitude	Longitude	Site description
Surface water (SW)			
SW1	44.7962	20.4259	The Sava; 4 km before the confluence
SW2	44.7989	20.4336	The Sava; 3.5 km before the confluence; downstream from the largest WW canal (WW1)
SW3	44.8019	20.4400	The Sava; 2.7 km before the confluence
SW4	44.8233	20.4368	The Danube; 500 m before the confluence
SW5	44.8241	20.4434	The confluence
SW6	44.8305	20.4828	The Danube; 3.6 km after the confluence
SW7	44.8279	20.5091	The Danube; 5.6 km after the confluence
SW8	44.8231	20.5359	The Danube; 8.5 km after the confluence; small bay
Wastewater (WW)			Number of inhabitants connected to WW canal
WW1	44.7976	20.4346	The largest WW canal; catchment area of 7,277 ha; 500,000
WW2	44.8118	20.4494	Catchment area of 113 ha; 23,000
WW3	44,8229	20.4419	The second large WW canal; catchment area of 2,620 ha; 225,000
WW4	44.8293	20.4694	Catchment area of 92 ha; 17,000
WW5	44.8245	20.4953	Catchment area of 1,112 ha; 165,000
WW6	44.8239	20.5035	Catchment area of 50 ha; 5,000
WW7	44.8277	20.5430	Catchment area of 116 ha; 7,000

Table S-III. Lowest PNEC values of detected pharmaceuticals in freshwater obtained from NORMAN database.

Pharmaceuticals	Norman PNEC ID	CAS No.	Taxon. group	Scientific name	Applied AF	Justification	Derivation method	Lowest PNEC freshwater (μg L^{-1})	Ref
Trimethoprim	PNEC-ID-0348354	738-70-5	n.r. [a]	n.r.	0	n.r.	n.r.	0.5	1
Metoprolol	PNEC-ID-0348060	51384-51-1	PI	*Desmodesmus subspicatus*	50	n.r.	deterministic	8.6	2
Sulfamethoxazole	PNEC-ID-0348126	723-46-6	P	*Synechococcus leopoliensis*	10	n.r.	deterministic	0.6	2
Azithromycin	PNEC-ID-0347903	83905-01-5	PI	*Microcystis aeruginosa*	10	n.r.	deterministic	0.019	2
Bisoprolol	PNEC-ID-0348209	66722-44-9	PIV	n.r.	50	n.r.	deterministic	92	3
Enalapril	PNEC-ID-0031812	75847-73-3	fish	-	1000	[b]	deterministic	1.58	4
Carbamazepine	PNEC-ID-0347929	298-46-4	I	*Daphnia pulex*	50	n.r.	deterministic	2	2
Diazepam	PNEC-ID-0257661	439-14-5	F	*Danio rerio*	10	[c]	deterministic	0.29	5
Atorvastatin	PNEC-ID-0348226	134523-00-5	PIV	n.r.	10	n.r.	deterministic	8.5	6
Diclofenac	PNEC-ID-0348270	15307-86-5	n.r.	n.r.	0	n.r.	n.r.	0.04	7

[a] n.r. – not reported
[b] One predicted short-term L(E)C50 from each of three trophic levels (i.e., base set)
[c] Long-term results (e.g., EC10 or NOECs) from at least three species (normally fish, Daphnia and algae) representing three trophic levels

Table S-IV. Validation parameters of the analytical method: recoveries and relative standard deviations (RSD), limits of detection (LOD) and quantification (LOQ), and linearity correlation coefficient (R^2).

Pharmaceuticals	Recovery, % (RSD, %) Spiking level, ng L^{-1}		LOD, ng L^{-1}	LOQ, ng L^{-1}	R^2
	100	1000			
Trimethoprim	88 (8)	92 (5)	11.0	36.8	0.993
Metoprolol	87 (12)	87 (5)	3.3	11.1	0.993
Sulfamethoxazole	83 (5)	70 (8)	30.0	100.0	0.999
Azithromycin	58 (7)	55 (11)	5.2	17.4	0.999
Bisoprolol	71 (12)	84 (11)	5.2	17.2	0.997
Enalapril	117 (19)	110 (11)	30.0	100.0	0.993
Cilazapril	88 (2)	101 (7)	3.9	13.2	0.997
Erythromycin	56 (17)	62 (10)	4.1	13.7	0.997
Bromazepam	89 (11)	93 (7)	25.0	83.3	0.998
Amlodipine	81 (4)	96 (2)	23.4	77.9	0.998
Carbamazepine	107 (8)	101 (8)	3.6	11.8	0.999
Lorazepam	83 (13)	93 (6)	14.3	47.6	0.996
Diazepam	86 (10)	95 (4)	21.1	70.3	0.990
Atorvastatin	95 (2)	83 (5)	19.6	65.5	0.999
Diclofenac	83 (20)	92 (13)	23.1	76.9	0.993
Clopidogrel	87 (7)	94 (1)	9.3	30.9	0.999
Simvastatin	118 (19)	107 (7)	50.0	166.7	0.998

Table S-V. Hazard identification of detected pharmaceuticals.

Pharmaceutical	Persistence	Bioaccumulation	Toxicity	Mobility	Endocrine Disruption (ED)	Ref.
Trimethoprim	Moderate	Low	Moderate	High	Not reported	8
Metoprolol	Moderate	Low	Low	Moderate–high	Possible functional ED	9-11
Sulfamethoxazole	Moderate	Low	High	Moderate–high	May exhibit endocrine toxicity	12-14
Azithromycin	Moderate–high	Low–moderate	High	Moderate–high	May have endocrine effects	15
Bisoprolol	Moderate	Low	Low	Moderate	Not reported	16,17
Enalapril	Moderate	Low	Low	Moderate	Not classified as ED	18,19
Cilazapril	Moderate	Low	Low	Moderate	Not reported	20
Erythromycin	High	Low	High	High	Potential disruptor	21-23
Carbamazepine	High	Low	High	High	Potential to function as an ED	24-26
Lorazepam	Moderate	Low	Moderate	Moderate	Functional ED uncertainty	27
Diazepam	Moderate–high	Low–moderate	Moderate	Moderate	Potential to interact with endocrine function	28,29
Atorvastatin	Low–moderate	Low	Moderate	Moderate	Not reported	30,31
Diclofenac	Moderate-high	Low	Moderate-high	Moderate-high	Possible ED	32,33

REFERENCES

1. J. Bengtsson-Palme, D.G. J. Larsson, *Environ. Int.* **86** (2016) 140 (https://doi.org/10.1016/j.envint.2015.10.015)
2. Proposals for Quality Criteria for Surface Waters, Oekotexzentrum centre ecotex, Available at: https://www.oekotoxzentrum.ch/expertenservice/qualitaetskriterien/qualitaetskriterienvorschlaege-oekotoxzentrum/ (date accessed: April 24, 2025)
3. M. Baumann, K. Weiß, I. Kirst, W. Kopf, *Umweltqualitätsnormen (UQN) für Binnengewässer*, Umweltbundesamt, Dessau-Roßlau, Germany, 2020, p. 45 (https://doi.org/10.60810/openumwelt-5724)
4. R. Aalizadeh, P. von der Ohe, N.S. Thomaidis, *Environ. Sci.: Process. Impacts* **19** (2017) 438 (https://www.norman-network.com/nds/susdat/)
5. US-EPA (2018) AQUIRE database, Available at: https://cfpub.epa.gov/ecotox/search.cfm (date accessed: May 9, 2025)
6. ad hoc EQS List, Oekotexzentrum centre ecotex, 2022, Available at: http://www.ecotoxcentre.ch/expert-service/quality-criteria/quality-criteria-for-surface-waters (date accessed: May 9, 2025)
7. European Commission, ANNEXES to the Proposal for a Directive of the European Parliament and of the Council amending Directive 2000/60/EC establishing a framework for Community action in the field of water policy, Directive 2006/118/EC on the protection of groundwater against pollution and deterioration and Directive 2008/105/EC on environmental quality standards in the field of water policy, 2022, Available at: chrome-extension://efaidnbmnnnibpcajpcglclefindmkaj/https://eur-lex.europa.eu/resource.html?uri=cellar:d0c11ba6-55f8-11ed-92ed-01aa75ed71a1.0001.02/DOC_2&format=PDF (date accessed: May 9, 2025)
8. J. O. Straub, *Antibiotics* **2** (2013) 115–162 (http://dx.doi.org/10.3390/antibiotics2010115)
9. F. Grönera, C. Höhnea, W. Kleinera, W. Kloas, *Ecotoxicol. Environ. Saf.* **141** (2017) 271 (http://dx.doi.org/10.1016/j.ecoenv.2017.03.032)

10. D. Love, M. Slovisky, K. A. Costa, D. Megarani, Q. Mehdi, V. Colombo, E. Ivantsova, K. Subramaniam, J. A. Bowden, J. H. Bisesi Jr., C. J. Martyniuk, *Environ. Toxicol. Chem.* **43** (2024) 2530 (http://dx.doi.org/10.1002/etc.5981)
11. A. Massarsky, V. L. Trudeau, T. W. Moon, *J. Exp. Zool.* **315** (2011) 251 (https://doi.org/10.1002/jez.672)
12. W. Duan, H. Cui, X. Jia, X. Huang, *Sci. Total Environ.* **820** (2022) 153178 (http://dx.doi.org/10.1016/j.scitotenv.2022.153178)
13. D. Archundia, C. Duwig, L. Spadini, M.C. Morel, B. Prado, M. P. Perez, V. Orsaga, J. M. F. Martins, *Environ. Int.* **130** (2019) 104905 (https://doi.org/10.1016/j.envint.2019.104905)
14. K. Yu, Y. Qui, Y. Shi, X. Yu, T. Dong, Y. Wu, H. Li, L. Huang, *Ecotox. Environ. Safety* **247** (2022) 114234 (https://doi.org/10.1016/j.ecoenv.2022.114234)
15. E. Kalugendo, P. Singh, R. Agaewal, *Sust. Chem. One World* **7** (2025) 100106 (https://doi.org/10.1016/j.scowo.2025.100106)
16. A. A. Godoy, I. Domingues, L. B. de Carvalho, A. C. Oliviera, C. C. de Jesus Azevedo, J. M. Taparo. P. K. Assano, V. Mori, V. de Almeida Vergara Higalgo, A. J. A. Nogueira, F. Kummroe, *Environ. Sci. Pollut. Res.* **27** (2020) 5469 (https://doi.org/10.1007/s11356-019-07322-0)
17. Janusinfo Bisoprolol, Available at: https://janusinfo.se/beslutsstod/lakemedelochmiljo/pharmaceuticalsandenvironment/databaseenven/bisoprolol.5.30a7505616a041a09b06299f.html (data accessed: November 7, 2025)
18. M. Filice, A. Caferro, D. Amelio, F. Impellitteri, M. A. Iovine, M. Porretti, C. Faggio, A. Gattuso, M. C. Cerra, S. Imbrogno, *Aquat. Toxicol.* **273** (2024) 107014 (https://doi.org/10.1016/j.aquatox.2024.107014)
19. Janusinfo Enalapril, Available at: https://janusinfo.se/beslutsstod/lakemedelochmiljo/pharmaceuticalsandenvironment/databaseenven/enalapril.5.30a7505616a041a09b062a0e.html (date accessed: November 6, 2025)
20. A. Kravos, A. A. Žgajnar Gotvajn, H. Prosen, *Processes* **12** (2024) 2177 (https://doi.org/10.3390/pr12102177)
21. Janusinfo Erythromycin, Available at: https://janusinfo.se/beslutsstod/lakemedelochmiljo/pharmaceuticalsandenvironment/databaseenven/erythromycin.5.30a7505616a041a09b063251.html (data accessed: November 17, 2025)
22. K. Wang, T. Larkin, N. Singhal, Y. Song, *Sci. Tot. Environ.* **624** (2018) 1263 (https://doi.org/10.1016/j.scitotenv.2017.12.243)
23. J. Ren, S. Ni, Y. Shen, D. Niu, R. Sun, C. Wang, L. Deng, Q. Zhang, Y. Tang, X. Jiang, Z. Li, C. Li, *J. Clean. Prod.* **379** (2022) 134758 (https://doi.org/10.1016/j.jclepro.2022.134758)
24. Janusinfo Carbamazepine, Available at: https://janusinfo.se/beslutsstod/lakemedelochmiljo/pharmaceuticalsandenvironment/databaseenven/carbamazepine.5.30a7505616a041a09b063c57.html (available at: November 20, 2025)
25. T. J. Scheytt, P. Mersmann, T. Heberer, *J. Contam. Hydrol.* **83** (2006) 53 (https://doi:10.1016/j.jconhyd.2005.11.002)
26. H. Chen, X. Gu, Q. Zeng, Z. Mao, *Int. J. Environ. Res. Public Health* **16** (2019) 209 (https://doi:10.3390/ijerph16020209)

27. S. A. Hernández Martínez, E. M. Melchor-Martínez, R. B. González-González, J. E. Sosa-Hernández, R. G. Araújo, J. A. Rodríguez-Hernández, D. Barceló, R. Parra-Saldívar, H. M.N. Iqbal, *Environ. Res.* **229** (2023) 115892 (https://doi.org/10.1016/j.envres.2023.115892)
28. K. Tolić Čop, M. Gotovuša, D. Mutavdžić Pavlović, D. Dabić, I. Grčić, *Nanomaterials* **15** (2025) 827 (https://doi.org/10.3390/nano15110827)
29. C. L. Overturf, M. D. Overturf, D. B. Huggett, *Comp. Biochem. Physiol. C* **183–184** (2016) 46 (http://dx.doi.org/10.1016/j.cbpc.2016.02.001)
30. Janusinfo Atorvastatin, Available at: https://janusinfo.se/beslutsstod/lakemedelochmiljo/pharmaceuticalsandenvironment/databaseenven/atorvastatin.5.30a7505616a041a09b062c27.html#query/Diazepam (data accessed: November 19, 2025)
31. M. M. Santos, R. Ruivo, M Lopez-Marques, T. Torres, C. B. de los Santos, L. F. C. Castro, T. Neuparth, *Aquat. Toxicol.* **174** (2016) 1 (http://dx.doi.org/10.1016/j.aquatox.2016.02.001)
32. L. Lonappan, S. Kaur Brar, R. Kumar Das, M. Verma, R. Y. Surampalli, *Environ. Int.* **96** (2016) 127 (https://doi:10.1016/j.envint.2016.09.014)
33. N. J. Efosa, W. Kleiner, W. Kloas, F. Hoffmann, *Chemosphere* **173** (2017) 69 (http://dx.doi.org/10.1016/j.chemosphere.2017.01.030).

Journal of the Serbian Chemical Society
JSCS-info@shd.org.rs • www.shd.org.rs/JSCS
J. Serb. Chem. Soc. 91 (5) 557–557 (2026)
JSCS–5509
Original scientific paper
Published 24 March, 2026

Errata*

Article "A comparative study on ecological risk assessment of some potentially toxic elements accumulation in surface sediment of stagnant and running water ecosystems in Meriç delta wetland, Turkish Thrace", by GAZEL BURCU AYDIN, number *JSCS–5394,* printed in *J. Serb. Chem. Soc.* **90**(3) 383–392 (2025) (https://doi.org/10.2298/JSC240116107A) contained some errors.

On page 385, in EXPERIMENTAL, in the last sentence of paragraph *Chemical analysis* values are given in mg/L, but should be in mg/kg.

On page 386, in RESULTS AND DISCUSSION, in the first paragraph, values are given in mg/L, but should be in mg/kg.

Article "Biochanin A formulation with electrospun poly(vinylpyrrolidone) fibers and possible applications", *J. Serb. Chem. Soc.*, vol. 91, no. 4, pp. 381–398, May 2026, is published with the wrong DOI number in the footnote. The correct DOI number is https://doi.org/10.2298/JSC251125007G.

* https://doi.org/10.2298/JSC260324015M